UNIVERSITY OF CALIFORNIA SAN DIEGO

Mitochondrial Organization in Neurons: Interplay of Dynamics and Morphology

A dissertation submitted in partial satisfaction of the
requirements for the degree Doctor of Philosophy

in

Physics with a Specialization in Quantitative Biology

by

Anamika Agrawal

Committee in charge:

Professor Elena F Koslover, Chair
Professor Brenda Bloodgood
Professor David Kleinfeld
Professor Gulcin Pekkurnaz
Professor Wouter-Jan Rappel

2022

The Dissertation of Anamika Agrawal is approved, and it is acceptable in quality and form for publication on microfilm and electronically.

University of California San Diego

2022

DEDICATION

I dedicate this thesis to my family; parents and sister. They have been steadfast in their love and support for me all these years, even when my decisions for self-fulfilment meant that I had to live my life separately from theirs thousands of miles away.

TABLE OF CONTENTS

LIST OF FIGURES

LIST OF TABLES

ACKNOWLEDGEMENTS

I would like to thank Professor Elena F Koslover for her mentorship during my PhD. She has been my toughest critic and my greatest supporter at the many inflection points during my graduate program. She has taught me the value of humility and perseverance in research that I will cherish through the rest of my life.

I would also like to thank my committee members for their invaluable guidance and support. I would like to thank Professor Gulcin Pekkurnaz who was also an early collaborator and supporter of our work. I would also like to extend a special thanks to Professor David Kleinfeld who went above and beyond to support my career and research.

A PhD can be a lonely journey but I had the support of fellow group members who were delightful friend/colleague hybrids. Dr. Saurabh Mogre and Zuben Scott were fellow crewmates in the Physics PhD program and always had clever insights and occasionally witty quips about my research. Professor Aidan Brown, a former postdoc in our group, has given me useful advice on improving my communication skills, and I still turn to him for occasional advice.

I also had the immense privilege of collaborating with Professor Erin Barnhart at Columbia University and her amazing group members. I would specifically like to thank Eavan Donovan and Nicole Liberman who were a joy to work with and also made the last chapter of this dissertation possible.

I would also like to thank Professors Terry Hwa, Philbert Tsai and Alex Groisman, who introduced me and the rest of the qBio program to the wonders of interdisciplinary research. I would also like to thank my classmates in the Physics department and my qBio cohort for providing an intellectual environment I thoroughly enjoyed in my first two years of training. I would also like to thank Sharmila Poddar, Catherine Mcconney and Kevin Smith at the Physics department for facilitating my research. I would also like to thank the excellent mental health care providers I had through grad school, who helped me overcome a lot of personal and professional hurdles.

These past six years my life was made many times better by friends in La Jolla and

Pasadena. Manho, Huanyu, Chih-Chun, Pan and Alex started off as friends from classes and then became much more. Vaishakh, Sasank, Jonathan, Joyce, Samantha, Vinicius, Arian, Paco and Ana let me keep my sanity during the pandemic. Best friends from back home - Pratik, Komal and Malvika, called me to check on me and somehow always knew when I needed them the most.

I would like to thank Anchal Gupta, my long time partner, who has been my top supporter from our undergraduate days. I would finally like to thank my family; my parents and my sister, as well as my late grand parents. Through the sparse visits these past 6 years; through the uncertainity of the pandemic; and through their own personal trials, my family has been unwaivering in their love and support.

Chapter 2, in full, is a reprint of the material as it appears in Agrawal, A., Pekkurnaz, G. and Koslover, E.F. "Spatial control of neuronal metabolism through glucose-mediated mitochondrial transport regulation", *Elife*, 7, p.e40986, (2018). The dissertation author was the primary author of this paper.

Chapter 3, in full, is a reprint of the material as it appears in Agrawal, A. and Koslover, E.F. "Optimizing mitochondrial maintenance in extended neuronal projections", *PLOS Computational Biology*, 17(6), p.e1009073. (2021). The dissertation author was the primary author of this paper.

Chapter 4, in part, is currently being prepared for submission for publication of the material. Donovan, E. J.*, Agrawal, A.*, Liberman, N., Kalai, J. I., Chua, N. J., Koslover, E. F. and Barnhart, E. L. , 2021. "Dendritic Architecture Determines Mitochondrial Distribution Patterns *in vivo*." The dissertation author was one of the primary authors of this material.

VITA

2016	Bachelor of Technology in Engineering Physics, Indian Institute of Technology, Bombay
2016-2017	qBio Research Fellow, University of California San Diego
2017–2020	Teaching Assistant, Department of Physics University of California San Diego
2017-2022	Graduate Research Assistant, University of California San Diego
2022	Doctor of Philosophy in Physics with a Specialization in Quantitative Biology, University of California San Diego

PUBLICATIONS

Published

Agrawal, A., Scott, Z. C. and Koslover, E. F., 2021. Morphology and Transport in Eukaryotic Cells. **Annual review of biophysics** 51 (2022).

Agrawal, A. and Koslover, E.F., 2021. Optimizing mitochondrial maintenance in extended neuronal projections. **PLOS Computational Biology**, 17(6), p.e1009073.

Agrawal, A., Pekkurnaz, G. and Koslover, E.F., 2018. Spatial control of neuronal metabolism through glucose-mediated mitochondrial transport regulation. **Elife**, 7, p.e40986.

Mazur, M., Pokorný, P., Brown, P., Weryk, R.J., Vida, D., Schult, C., Stober, G. and **Agrawal, A.**, 2020. Precision measurements of radar transverse scattering speeds from meteor phase characteristics. **Radio Science**, 55(10), pp.1-32.

Under review

Konno, T., Parutto, P., Bailey, D.M., Davì, V., Crapart, C., Awadelkareem, M.A., Hockings, C., Brown, A., Xiang, K.M., **Agrawal, A.** and Chambers, J.E., 2021. Endoplasmic Reticulum morphological regulation by RTN4/NOGO modulates neuronal regeneration by slowing luminal transport. *Submitted to* **Developmental Cell**.

In preparation

Donovan, E. J.*, **Agrawal, A.***, Liberman, N., Kalai, J. I., Chua, N. J., Koslover, E. F. and Barnhart, E. L. , 2021. Dendritic Architecture Determines Mitochondrial Distribution Patterns *in vivo*. (* denotes equal contribution)

Agrawal, A., Capponi, S., Baker, J., Dueber, J., Marshall, W. and Bianco, S., 2021. Design Principles of Yeast Peroxisomes using Coarse-Grained Models.

ABSTRACT OF THE DISSERTATION

Mitochondrial Organization in Neurons: Interplay of Dynamics and Morphology

by

Anamika Agrawal

Doctor of Philosophy in Physics with a Specialization in Quantitative Biology

University of California San Diego, 2022

Professor Elena F Koslover, Chair

Neurons are large eukaryotic cells with high metabolic demands. Intracellular transport plays an important role in maintaining metabolic functioning in neurons despite heterogeneous spatio-temporal energetic demands. Mitochondria are the primary source of ATP in neurons and are distributed through motor-driven transport along neuronal cytoskeleton from the cell body of the neuron (soma) to long neuronal projections (axons and dendrites). Transport-based organization of mitochondria is regulated through a combination of mechanisms that control mitochondrial dynamics and its interplay with neuronal cytoskeleton.

One important regulatory mechanism is the control of mitochondrial motility through molecules such as glucose and Calcium that are localized to high metabolic activity regions in

axons. In Chapter 2, we use a reaction-diffusion framework to analyze how glucose-regulated mitochondrial motility can be an effective mechanism within physiological limits to adapt metabolic organization to increase mitochondrial glucose turnover.

While local changes in motor activity of mitochondria create local stationary populations to service high-demand sites, there is still the issue of how mitochondrial populations across the long length scales of neuronal projections are maintained at varying distances from the soma throughout neuronal lifetimes. In Chapter 3, we develop a quantitative framework to understand how mitochondrial dynamics of transport, fusion-fission and mitophagy, can be tuned to optimize the distribution of healthy mitochondria throughout interspersed sites located in long and occasionally branched axonal projections.

On longer length scales, axons and dendrites have interesting branched morphologies. Mitochondrial distribution patterns need to be robust to variations in subtree morphologies in dendrites so that distal branches with high metabolic activity have equitable but increased supply of mitochondria. In Chapter 4, we show that a combination of morphological scaling rules and mitochondrial transport behavior can explain how mitochondria are 'equitably' distributed in a *Drosophila* HS dendritic tree yet still maintaining increased densities in distal tips. Our predicted laws are corroborated by experimental observations of dendritic morphology and mitochondrial motility.

This dissertation combines various quantitative models at different scales in neurons to understand how mitochondrial distribution patterns can lead to robust metabolic fulfilment in neurons.

Chapter 1

Introduction

Neurons are one of the most metabolically active cells in our body. Several neuronal processes, such as synaptic transmission [212], neurotransmitter recycling [165] and generation of axonal action potentials [108] have high ATP demands. The problem of energetic fulfilment is further compounded by the long length scales of neuronal projections (hundreds of microns to meters long) and spatio-temporal specificity of metabolic demands in neurons. For example, presynaptic boutons and dendritic spines need large amounts of ATP during synaptic firing and integration processes. However these sites can have interspersed locations at long distances from the neuronal cell body (soma). The length scales between these sites are often larger than the diffusivities of ATP and glucose [134], thus necessitating active redistribution of intracellular components to maintain metabolic sufficiency. In addition, the time-sensitive nature of neuronal processes [201] also requires robustness in metabolic organization.

Like most large eukaryotic cells, neurons have a large number of mitochondria positioned throughout their extent to supply ATP in a timely and reliable manner [239]. In addition to providing the bulk of ATP required by neurons, mitochondria are also involved in calcium buffering important for intracellular processes[159]. Since mitochondria originate from the soma, with replication not observed outside of the cell body [40], they are distributed to axons and dendrites through active transport along microtubules forming neuronal cytoskeleton. The resulting distribution patterns of stationary and motile mitochondrial pools in axons and dendrites

is tuned to ensure proper servicing of high metabolic activity regions such as presynaptic boutons, dendritic spines and nodes of Ranvier [166].

To create and maintain optimal distribution of mitochondria in neurons, several regulatory mechanisms have been proposed. Mitochondrial motility has been observed to be modified by substrates such as Ca^{+2} [216] and glucose [153], which, in turn, are regulated by neuronal activity [8, 119]. Ca^{+2} binds to mitochondrial motor adapters to prevent kinesin binding to microtubules, resulting in mitochondrial stopping [216]. Increased glucose concentrations at locations of dense glucose entry channels at high demand regions lead to mitochondrial arrest through action of Glucose to ATP pathway intermediates on mitochondrial motor adapters [153]. Such transport-regulation mechanisms ensure that stationary populations of mitochondria are located at metabolic activity site to maintain a reliable supply of ATP. In Chapter 2, we use a quantitative model with a reaction-diffusion formalism to delineate the physical limits of glucose-dependent mitochondrial motility in being an effective mechanism in neurons. We find that intracellular glucose concentrations are poised at the critical limit where this particular control mechanism can be beneficial. We show that under physiological conditions, the distribution changes caused due to glucose-mediated mitochondrial halting can lead to a significant increase in glucose turnover.

Once an adequate distribution of mitochondria is established, it is also important that these mitochondria remain functional throughout the lifetime of a neuron. Mitochondrial health may degrade over hours due to protein degradation and oxidation [43]. On the other hand, neuronal lifetimes are much longer. Mitochondria are stationed for long periods of time at locations far away from the soma while they undergo degradation and reduction in ATP production capacity. To address this problem, several quality control mechanisms have been proposed. Interactions of stationary mitochondria with the small motile population through transient fusion events and occasional replacement can lead to long-term equilibration of health levels between the relatively-younger motile population of mitochondria and the stationary pool, thereby optimizing overall mitochondrial quality. Some unhealthy mitochondria can also be primed for degradation

and removed from the mitochondrial pool to further optimize the quality of the pool throughout the long lengths of axonal and dendritic domains. Thus, mitochondrial transport and fission-fusion dynamics need to be tuned to ensure a distribution of healthy mitochondria throughout the extended and branched morphology of neuronal projections. In Chapter 3, we develop a quantitative framework to explore how a healthy population of mitochondria can be maintained across interspersed demand sites in neurons, through a combination of interaction dynamics and selective turnover through mitophagy. We find that a low number of interaction events as well as a high stationary fraction of mitochondria optimize overall and distal mitochondrial health over a long range of degradation rates for mitochondrial components. These optimizing parameters don't change even if we introduce small amounts of local translation, which is another mechanism that could be employed towards mitochondrial health maintenance. We also show that stochastic interchange of motile and stationary mitochondria as well as transient fusion events both lead to similar steady-state health levels of mitochondria, but transient fusion could be more robust in mitochondrial health maintenance. We also show that introducing small levels of mitophagy can significantly enhance mitochondrial health when coupled with mitochondrial dynamics, but transient fusion events are better at leveraging mitophagy for quality control.

Neuronal projections over small length scales appear as simple linear domains, but over longer length scales they tend to have branched structures. Dendritic trees, in particular, have a complex tree-like morphology over short distances from the soma. Dendritic spines, that connect to presynaptic terminals, tend to be localized in the distal branches of dendrites. Mitochondria need to be distributed in such a way that these distal branches, irrespective of the parent tree structure, have balanced fulfilment of metabolic needs. In Chapter 4, we show that a combination of morphological scaling rules for dendritic trees and mitochondrial transport behavior can explain how mitochondria can be 'equitably' distributed in a *Drosophila* HS dendritic tree while still making sure distal mitochondrial densities increase away from the soma, despite variations in subtree morphology. These laws are corroborated by experimental measurements of dendritic morphology and mitochondrial motility in HS neurons.

This thesis aims to highlight some quantitative frameworks to understand how neurons maintain metabolic sufficiency and flexibility through mitochondrial transport regulation and organization. In addition, we also analyze the interplay of transport and morphology as another lens for intracellular organization. Broadly, this work provides an example of how intracellular organization, regulated through a combination of morphology and transport [2], forms an important part of the metabolic compartmentalization strategy in eukaryotic cells especially neural cells.

Chapter 2

Spatial Control of Neuronal Metabolism Through Glucose-Mediated Mitochondrial Transport Regulation

2.1 Abstract

Eukaryotic cells modulate their metabolism by organizing metabolic components in response to varying nutrient availability and energy demands. In mammalian axons, mitochondria respond to glucose levels by halting active transport in high glucose regions. We employ quantitative modeling to explore physical limits on spatial organization of mitochondria and localized metabolic enhancement through regulated stopping of processive motion. We delineate the role of key parameters, including cellular glucose uptake and consumption rates, that are expected to modulate mitochondrial distribution and metabolic response in spatially varying glucose conditions. Our estimates indicate that physiological brain glucose levels fall within the limited range necessary for metabolic enhancement. Hence mitochondrial localization is shown to be a plausible regulatory mechanism for neuronal metabolic flexibility in the presence of spatially heterogeneous glucose, as may occur in long processes of projection neurons. These findings provide a framework for the control of cellular bioenergetics through organelle trafficking.

2.2 Introduction

Cellular metabolism comprises an intricate system of reactions whose fine-tuned control is critical to cell health and function. A number of quantitative studies have focused on metabolic control through modulating reactant and enzyme concentrations and turnover rates [66, 3]. However, these studies generally neglect the spatial organization of metabolic components within the cell. By localizing specific enzymes in regions of high metabolic demand[102, 233], as well as clustering together consecutively acting enzymes[146], cells have the potential to substantially enhance their metabolism.

Spatial organization is particularly critical in highly extended cells, such as mammalian neurons, whose axons can grow to lengths on the meter scale. Metabolic demand in neurons is spatially and temporally heterogeneous, with especially rapid ATP turnover found in the presynaptic boutons[165], and ATP requirements peaking during synaptic activity and neuronal firing[189, 53, 220]. Neurons rely primarily on glucose as the energy source for meeting these metabolic demands[154]. Due to the long lengths of neural processes, the glucose supply can vary substantially over different regions of the cell[53, 220, 70]. In myelinated neurons, for instance, it has been speculated that glucose transport into the cell is localized primarily to narrow regions around the nodes of Ranvier[121, 72, 169], which can be spaced hundreds of microns apart[81, 20]. Glucose transporters in neurons have also been shown to dynamically mobilize to active synapses, providing a source of intracellular glucose heterogeneity[8].Furthermore, varying levels of activity in the mammalian brain may lead to varying extracellular glucose levels, resulting in spatially heterogeneous nutrient access[76]. Individual axons have been shown to span across multiple regions of the brain[131], enabling them to encounter regions with different glucose concentrations.

Most ATP production in neurons occurs within mitochondria: motile organelles that range from interconnected networks to individual globular structures that extend throughout the cell. As energy powerhouses and metabolic signaling centers of the cell, mitochondria are critical for

neuronal health [145]. Their spatial organization within the neuron plays a pivotal role in growth and cell physiology [111]. Defects in mitochondrial transport are involved in the pathologies of several neurological disorders such as peripheral neuropathy and Charcot-Marie-Tooth disease [11, 12].

A number of studies have shown that mitochondria are localized preferentially to regions of high metabolic demand, such as the synaptic terminals [111, 28]. Such localization can occur via several molecular mechanisms, mediated by the Miro-Milton mitochondrial motor adaptor complex that links mitochondria to the molecular motors responsible for transport[136]. Increased Ca^{2+} levels at active synapses lead to loading of calcium binding sites on Miro, releasing mitochondria from the microtubule and thereby halting transport[216, 119]. High glucose levels can also lead to stalling, through the glycosylation of motor adaptor protein Milton by the glucose-activated enzyme *O*-GlcNAc transferase (OGT)[153]. This mechanism has been shown to lead to mitochondrial accumulation at glucose-rich regions in cultured neurons[153]. It is postulated to regulate mitochondrial spatial distribution, allowing efficient metabolic response to heterogeneous glucose availability.

Mitochondrial positioning relies on an interplay between heterogeneously distributed diffusive signaling molecules (such as Ca^{2+} and glucose), their consumption through metabolic and other pathways, and their effect on motor transport kinetics. While the biochemical mechanisms and physiological consequences of mitochondrial localization have been a topic of much interest in recent years[118, 136], no quantitative framework for this phenomenon has yet been developed.

In this work we focus on glucose-mediated regulation of mitochondrial transport, developing quantitative models to examine the consequences of this phenomenon for metabolism under spatially varying glucose conditions. Our approach relies on a reaction-diffusion formalism, which describes the behavior of species subject to both consumption and diffusion. Reaction-diffusion systems have been applied to describe the spatial organization of a broad array of cellular processes[96], ranging from protein oscillations in *E. coli*[80], to coordination of

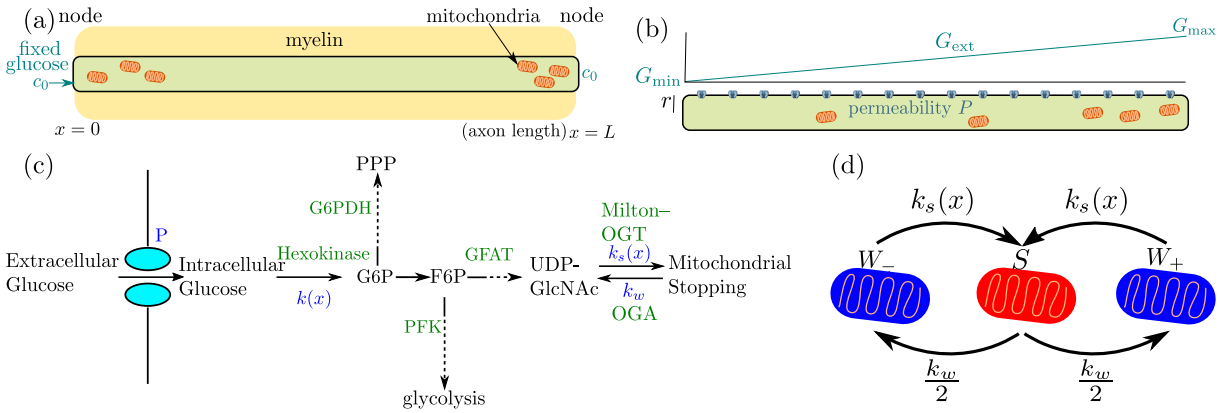

Figure 2.1. Schematic diagram of our simplified model for glucose-mediated mitochondrial transport regulation.
(a) Myelinated axonal region, with glucose entry localized at the nodes of Ranvier. Mitochondria accumulate at nodes due to the higher glucose concentration (b) Unmyelinated axonal region, subject to a linear glucose gradient. Glucose permeability is uniform throughout, with mitochondrial accumulation occuring at the region of high external glucose (c) Key steps of the metabolic pathway linking glucose availability and mitochondrial halting. (d) Mitochondrial transport states and rates of transition between them ($W_\pm$ represents retrograde and anterograde motion, S represents the stationary state).

mitotic signalling[29], to pattern formation in developing embryos[18, 65]. The response of actively moving particles to spatially heterogeneous, diffusive regulators has also been extensively investigated in the context of chemotaxis[208]. In contrast to most chemotactic cells, however, mitochondria have no currently known mechanism for directly sensing glucose gradients. Instead, they are expected to accumulate in response to local glucose concentration only. Our goal is to delineate the regimes in which such a crude form of chemotaxis can lead to substantial spatial organization and enhancement of metabolism.

Specifically, we model the modulation of mitochondrial density with glucose concentration in a tubular axonal region, focusing on two forms of spatial heterogeneity. In one case, we consider an axonal domain between two localized regions of glucose entry, representing the internodal region between nodes of Ranvier in myelinated neurons (Fig. 2.1a). The second case focuses on an unmyelinated cellular region with continuous glucose permeability, embedded in

an external glucose gradient (Fig. 2.1b). In both cases, we show that mitochondrial accumulation and enhanced metabolic flux is expected to occur over a limited range of glucose concentrations, which overlaps with physiological brain glucose levels. Our simplified quantitative model allows identification of a handful of key parameters that govern the extent to which glucose-mediated mitochondrial halting can modulate metabolism. We establish the region of parameter space where this mechanism has a substantial effect, and highlight its potential importance in neuronal metabolic flexibility and ability to respond to spatially varying glucose.

2.3 Results

2.3.1 Minimal model for mitochondrial and glucose dynamics

We begin by formulating a quantitative model to describe the spatial localization of mitochondria that halt in a glucose-dependent manner, in the presence of localized sources of glucose. This situation arises in myelinated neurons, which have glucose transporters enriched at the nodes of Ranvier, leading to highly localized sources of glucose spaced hundreds of micrometers apart within the cell[171].

Neuronal glucose transporters are known to be bidirectional[192], allowing glucose concentration within the cell to equilibrate with external glucose. For simplicity, we assume rapid transport of glucose through these transporters, so that the internal concentration of glucose at the nodes where transporters are present is assumed to be fixed. The cellular region between two glucose sources is modeled as a one-dimensional interval of length L with glucose concentration fixed to a value c_0 at the interval boundaries (Fig.2.1a). Glucose diffuses throughout this interval with diffusivity D, while being metabolized by hexokinase enzyme in the first step of mammalian glucose utilization (Fig. 2.1c) [224].

The concentration of glucose is thus governed by the reaction-diffusion equation,

$$\frac{dG}{dt} = D\frac{\partial^2 G}{\partial x^2} - k(x)G(x) \tag{2.1}$$

where $k(x)$ describes the spatial distribution of the hexokinase enzyme as well as the rate of consumption. In the case of spatially uniform, linear consumption [$k(x) = k$, a constant] this equation can be solved directly, yielding a distribution of glucose that falls exponentially from each source boundary, with a decay length $\lambda = \sqrt{D/k}$ [93].

Hexokinase 1 (HK1), the predominant form of hexokinase expressed in neurons, is known to localize preferentially to mitochondria[84], which in mammalian axons can form individual organelles approximately 1μm in length[51]. We carry out numerical simulations of Eq. 2.1 where consumption is limited to locations of individual discrete mitochondria, represented by short intervals of length Δ. Specifically, we define the mitochondria density as $M(x) = n(x)/(\pi r^2 \Delta)$, where $n(x)$ is the number of mitochondria overlapping position x, and r is the axon radius. The phosphorylation of glucose by mitochondrial hexokinase is assumed to follow Michaelis-Menten kinetics, described by

$$k(x) = \frac{k_{\mathrm{g}} M(x)}{G(x) + K_M}, \tag{2.2}$$

where K_M is the saturation constant and k_{g} is the turnover rate of glucose (per unit time per mitochondrion). The turnover rate k_g incorporates both the catalytic rate of hexokinase and the number of hexokinase enzymes per mitochondrion. This expression reduces to the case of constant linear consumption when glucose concentration is low ($G \ll K_M$) and mitochondria are uniformly distributed throughout the region.

In general, glucose consumption depends on the location of mitochondria within the domain. Mitochondrial distribution in neurons is known to be mediated through regulation of their motor-driven motility[28, 153]. Individual mitochondria switch between processively moving and paused states, modulated by the interplay between kinesin and dynein motors and the adaptor proteins that link these motors to the mitochondria[181]. In our model, we simulate mitochondria as stochastically switching between a processive walking state that moves in either direction with velocity v and a stationary state. The rate of initiating a walk (k_w) is assumed to be

constant, while the halting rate ($k_s(x)$) can be spatially heterogeneous. For simplicity, we assume the mitochondria are equally likely to move in the positive (+) or negative (-) direction each time they initiate a processive walk (Fig. 2.1b).

It has recently been demonstrated that the key motor adaptor protein (Milton) is sensitive to glucose levels, halting mitochondrial motility when it is modified through O-GlcNAcylation by the OGT enzyme[153]. Our model employs a highly simplified description of mitochondrial dynamics, which assumes that all pauses are associated with such an O-GlcNAcylation event. Recovery from the pause at the constant rate k_w corresponds to removal of the modification through the activity of the complementary enzyme O-GlcNAcase (OGA). Although there is evidence indicating long-term glucose deprivation can reduce OGA expression[240], for simplicity we assume in our model that OGA activity is independent of glucose levels. *In vivo* axonal mitochondria have been observed to undergo short-lived sporadic pausing while continuing to move processively in their previous anterograde or retrograde direction[170, 216]. Such pauses are subsumed into an effective processive velocity v in our model. Other sources of pausing, such as Ca^{2+}-regulated motor disengagement, PINK1/Parkin-mediated detachment of motors, and anchoring to the microtubules by syntaphilin [181], are not considered here in order to focus specifically on the effect of glucose-dependent mitochondrial spatial organization.

Upon entry into the cell, the first rate-limiting step of glucose metabolism is its conversion into glucose-6-phosphate by hexokinase. Further downstream metabolic pathways split, with much of the flux going to glycolysis while a small fraction is funneled into the pentose phosphate pathway and the hexosamine biosynthetic pathway (HBP). The HBP produces UDP-GlcNAc, the sugar substrate for O-GlcNAcylation (Fig. 2.1c)[75]. In our model, we assume that the rate of UDP-GlcNAc production equals the rate of glucose conversion by hexokinase, scaled by the fraction of G6P that is channeled into the hexosamine biosynthetic pathway. This assumption is valid if, at each point of pathway branching, the Michaelis-Menten saturation constants for the two branches are similar. This in fact appears to be the case for both the branching of the pentose phosphate pathway and glycolysis from the hexosamine biosynthetic pathway which is the focus

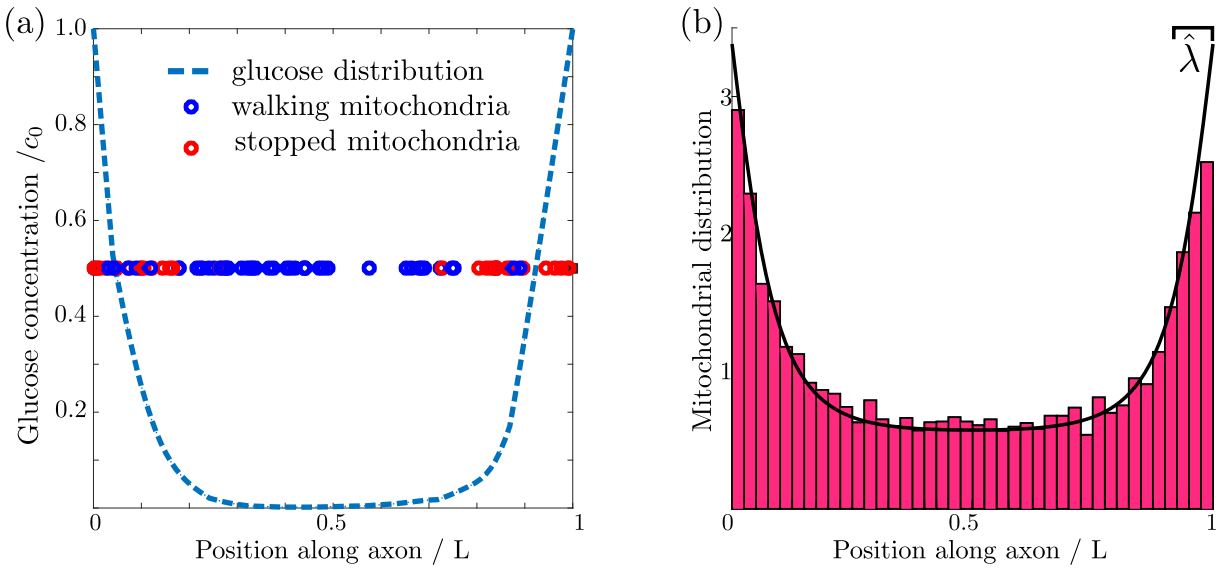

Figure 2.2. Glucose and mitochondrial distributions from simulations compared with numerical calculations.
(a) Glucose distribution and position of individual mitochondria (b) Normalized itochondrial distribution, $M(x)/\overline{M}$, obtained from simulating discrete mitochondrial motion (histogram compiled from 100 independent simulations), compared to numerical calculation of steady state continuous mitochondrial disribution (black curve). Results shown are for parameter values: $\hat{\lambda} = 0.08$, $\hat{c_0} = 1$, $\hat{k}_s = 100$.

of this work (see Appendix A.2). Consequently, saturation of the initial glucose conversion step will imply saturation of the entire hexosamine biosynthetic pathway. We therefore model the kinetics of Milton modification using the same Michaelis-Menten form as for hexokinase activity, with the pathway flux leading to Milton modification subsumed within a rate constant for mitochondrial stopping (k_s).

We note that the subcellular organization of the intermediates in the conversion from glucose into O-GlcNAcylated Milton is largely unknown. In our model, we make the extreme case assumption that all intermediates are localized to mitochondria, with only the initial glucose substrate capable of diffusing through the cytoplasm. We note that cytoplasmic diffusion of any of the pathway intermediates would attenuate the effect on mitochondrial localization. Our simplified model thus gives an upper limit on the extent to which mitochondria can localize at high glucose regions through the Milton modification mechanism. Following these simplified assumptions, we treat the kinetics of mitochondrial halting as dependent only on the local glucose concentration, according to the functional form

$$k_s(x) = \frac{k_s G(x)}{G(x) + K_M}, \tag{2.3}$$

where K_M is the Michaelis-Menten constant of hexokinase.

We proceed to evolve the simulation forward in time, with glucose consumption localized to regions within $\pm\Delta/2$ of each discrete mitochondrial position (details in Materials and Methods). A snapshot of one simulation run is shown in Fig. 2.2a, highlighting the accumulation of stationary mitochondria in the high glucose regions near the ends of the domain.

We are interested primarily in investigating the steady-state distribution of mitochondria and glucose in this system, averaged over all possible mitochondrial trajectories. We thus proceed to coarse-grain our model by treating the distribution of mitochondria as a continuous field $M(x) = W_+(x) + W_-(x) + S(x)$, where $W_+(x)$ is the distribution of mitochondria walking in the positive direction, $W_-(x)$ is the distribution of those walking in the negative direction,

Table 2.1. Physiological parameter values estimated from published data for Chapter 2

cytoplasmic glucose diffusivity	D	$140\mu\text{m}^2/\text{s}$
glucose turnover per mitochondrion	k_g	$1.3\times10^5\text{s}^{-1}$
axon radius	r	$0.4\mu\text{m}$
internodal distance	L	$250\mu\text{m}$
mitochondrial density	$\overline{M}$	$0.3\mu\text{m}^{-3}$
hexokinase Michaelis-Menten constant	K_M	0.03mM
brain glucose levels	c_0	$0.7-1.3$mM
ratio of stopped to moving mitochondria at high glucose	k_s/k_w	19
glucose permeability	P	20nm/s
glucose transporter (GLUT3) Michaelis-Menten constant	K_{MP}	3mM

Source: see Appendix A.1 for details of parameter estimates.

and $S(x)$ is the distribution of stationary mitochondria. We can then write down the coupled differential equations governing the behavior of the mitochondrial distributions as:

$$\begin{aligned}\frac{dW_+}{dt} &= -v\frac{\partial W_+}{\partial x} - k_s(x)W_+ + \frac{k_w S}{2}\\ \frac{dW_-}{dt} &= v\frac{\partial W_-}{\partial x} - k_s(x)W_- + \frac{k_w S}{2}\\ \frac{dS}{dt} &= k_s(x)[W_+ + W_-] - k_w S.\end{aligned} \tag{2.4}$$

The glucose distribution evolves according to Eq. 2.1 with consumption rate $k(x)$ given by Eq. 2.2. The boundary conditions at the ends of the domain are assumed to be reflective for the mitochondrial distributions, and to have a fixed glucose concentration c_0. The stationary state for this system can be calculated numerically (see Materials and Methods). The formulation with a continuous mitochondrial density faithfully represents the behavior of simulations with discrete mitochondria, as illustrated in Fig. 2.2b.

The steady-state spatial distribution of mitochondria and glucose in the continuous system depend on six parameters: $k_s/k_w, K_M, c_0, D, L, k_g\overline{M}$ where $\overline{M}$ is the average mitochondrial density in the axon (number of mitochondria per unit volume) . Estimates of physiologically relevant values are provided in Table 2.1. Dimensional analysis indicates that three of these parameters can be used to define units of time, length, and glucose concentration, leaving three dimensionless

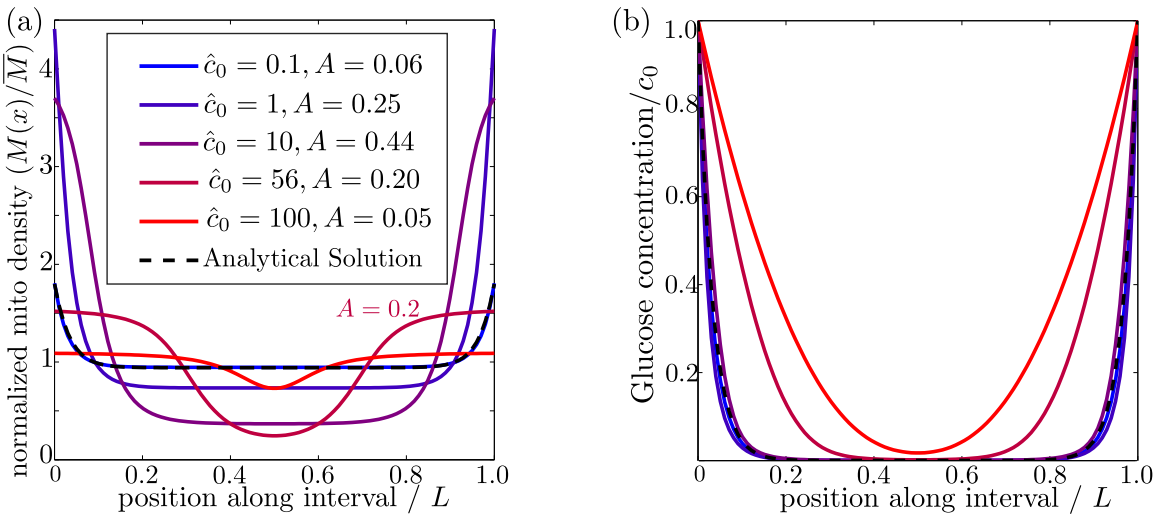

Figure 2.3. Effect of external glucose concentration on intracellular glucose and mitochondrial distributions.
(a) Normalized mitochondrial distribution $(M(x)/\overline{M})$, for different values of edge concentration $\hat{c_0}$. The curve with $\hat{c}_0 = 56$ illustrates the accumulation cutoff $A = 0.2$. (b) Glucose distribution normalized by edge concentration $(G(x)/c_0)$. The black dashed line in both panels indicates the analytical solution for the low glucose limit (Materials and Methods, Eq. 2.13). Source data provided in "Figure 3 - source data".

groups. We choose to use the following three dimensionless parameters, each of which has an intuitive physical meaning:

$$\hat{\lambda} = \sqrt{\frac{DK_M}{k_g \overline{M} L^2}}, \quad \hat{c}_0 = \frac{c_0}{K_M}, \quad \hat{k}_s = \frac{k_s}{k_w} \tag{2.5}$$

Here $\hat{\lambda}$ is the length-scale of glucose decay relative to the domain length, $\hat{c}_0$ is the boundary glucose concentration relative to the saturation constant K_M, and $\hat{k}_s$ is the ratio of stopped to walking mitochondria at high glucose levels. We proceed to explore the steady-state distribution of mitochondria and glucose as a function of these three parameters.

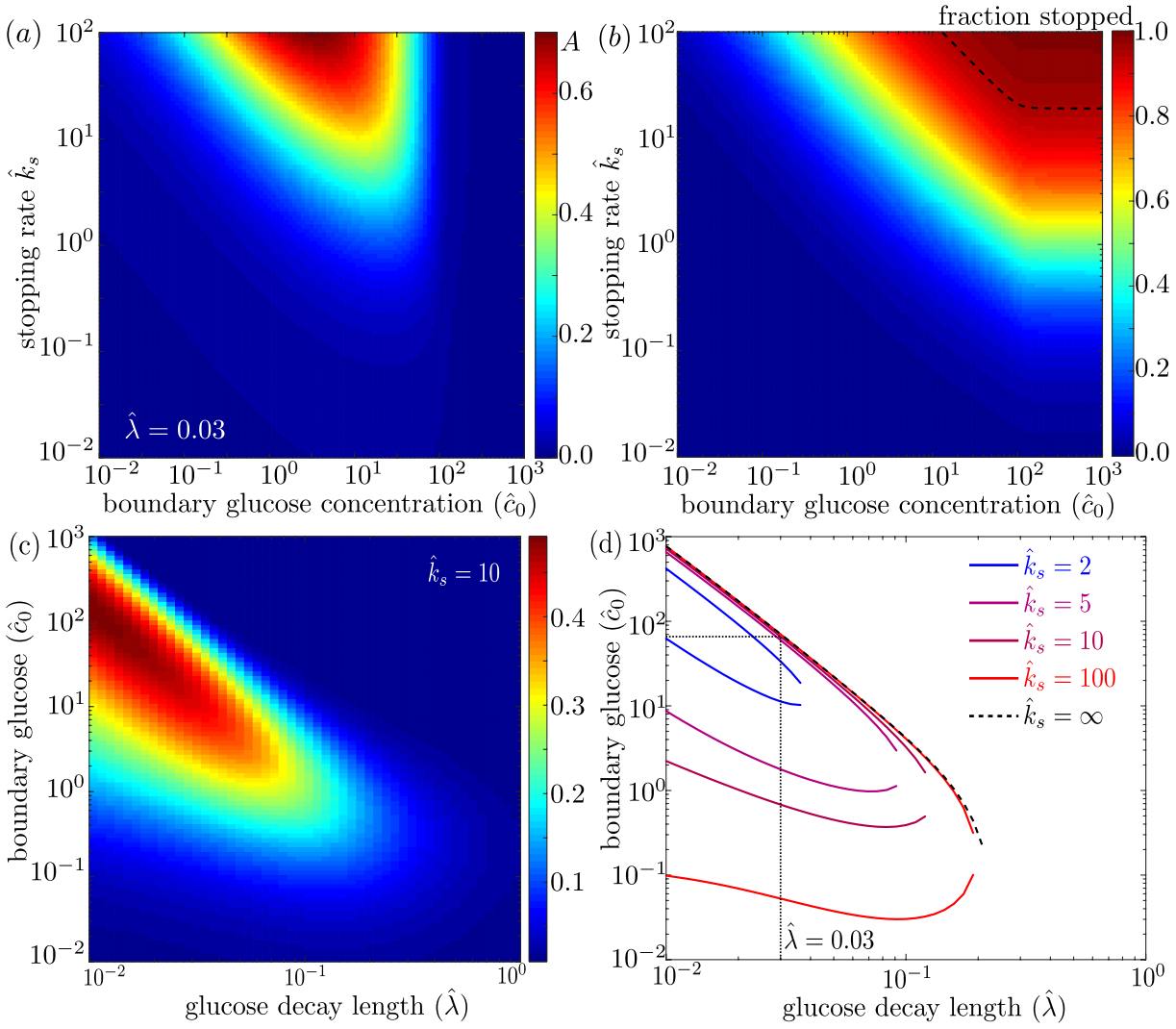

Figure 2.4. Effect of model parameters on mitochondrial accumulation at regions of localized glucose entry.
(a) Accumulation metric as a function of boundary glucose levels and mitochondrial stopping rate. (b) Fraction of mitochondria in the stopped state. Black dashed line indicates parameters corresponding to 95% stopped mitochondria. (c) Accumulation metric as a function of glucose levels $\hat{c}_0$ and decay length $\hat{\lambda}$. (d) Phase diagram for mitochondrial accumulation, showing upper and lower concentration cutoffs for accumulation above the cutoff of $A_{\text{cut}} = 0.2$. Dashed black line shows limit of high stopping rate $\hat{k}_s$. Dotted black line indicates estimate of $\hat{\lambda}$ for physiological parameters, and corresponding upper concentration cutoff. Source data provided in "Figure 4 - source data 1-3".

2.3.2 Mitochondrial localization requires limited range of external glucose

In order for mitochondria to preferentially accumulate at the source of glucose via a glucose-dependent stopping mechanism, three criteria must be met. First, the glucose concentration needs to be higher at the source than in the bulk of the cell, as occurs when the decay length due to consumption is much smaller than the size of the domain ($\hat{\lambda} \ll 1$). Second, if glucose levels become too high ($\hat{c}_0 \gg 1$) then both glucose consumption rates and stopping rates of the mitochondria become saturated, leading to a flattening of glucose and mitochondrial distributions (Fig. 2.3). There is thus an upper limit on the possible external glucose concentrations that will yield mitochondrial localization at the edges of the domain. Finally, the mitochondria must spend a substantial amount of time in the stationary state, since walking mitochondria will be broadly distributed throughout the domain. Because the stopping rate is itself dependent on the glucose concentration, this criterion implies that very low concentrations will also not allow mitochondrial localization. Fig. 2.3 shows the distribution of glucose and mitochondria at different values of the external glucose $\hat{c}_0$, illustrating that accumulation of mitochondria at the edges requires intermediate glucose levels.

To characterize the distribution of mitochondria along the interval, we introduce an accumulation metric A, defined by

$$A = 6\sigma^2/L^2 - 0.5$$

where σ^2 is the variance in the mitochondrial distribution. This metric scales from $A = 0$ for a uniform distribution to $A = 1$ for two narrow peaks at the domain edges. Mitochondrial distributions with several different values of the accumulation metric are shown in Fig. 2.3a. We use a cutoff of $A = 0.2$ to define distributions where the mitochondria are localized at the glucose source.

We explore the dependence of the mitochondrial accumulation on the three dimensionless

parameters defining the behavior of the system: the stopping rate constant $\hat{k}_s$, the glucose decay length $\hat{\lambda}$, and the external concentration $\hat{c}_0$. Because only the stopped mitochondria localize near the glucose sources, increasing the fraction of mitochondria in the stopped state (increased $\hat{k}_s$) inevitably raises the overall accumulation (Fig. 2.4a). The fraction of mitochondria in the stopped state will depend on both $\hat{k}_s$ and the overall levels of glucose, as dictated by $\hat{c}_0$ (Fig. 2.4b). Experimental measurements indicate that at high glucose concentrations, approximately 95% of mitochondria are in the stationary state[153]. We are thus interested primarily in the parameter regime of high stopping rates: $\hat{k}_s \gtrsim 10$. The limited range of concentrations that lead to mitochondrial accumulation at the edges of the domain can be seen in Fig. 2.4a.

For a high stopping rate ($\hat{k}_s = 10$), we then calculate the mitochondrial accumulation as a function of the remaining two parameters: $\hat{\lambda}, \hat{c}_0$. Here, again, we note that only intermediate glucose concentrations result in accumulation, with the range of concentrations becoming narrower as the decay length $\hat{\lambda}$ becomes comparable to the domain size (Fig. 2.4c). We can establish the concentration range within which substantial accumulation is expected, by setting a cutoff $A = 0.2$ on the accumulation metric and calculating the resulting phase diagram (Fig. 2.4d). Below the lower concentration cutoff, insufficient mitochondria are in the stationary state and so no localization is seen. This lower cutoff disappears in the limit of infinite $\hat{k}_s$. At intermediate concentrations, mitochondria are localized near the domain edges. Above the upper concentration cutoff, no localization is observed due to saturation of the Michaelis-Menten kinetics.

Using empirically derived approximations for the rate of glucose consumption by mitochondria and the diffusivity of glucose in cytoplasm (see Table 2.1), we estimate the decay length parameter as $\hat{\lambda} \approx 0.03$. The mitochondria are then expected to localize near the glucose source only if $\hat{c}_0 < 66$. Because the saturation concentration for hexokinase is quite low ($K_M \approx 0.03$mM)[224], we would expect mitochondrial accumulation for glucose concentrations below about 2 mM. We note that physiological brain glucose levels have been measured at $0.7 - 1.3$mM, depending on the brain region[132], implying that glucose-dependent halting of mitochondrial transport would be expected to result in localization of mitochondria at nodes of

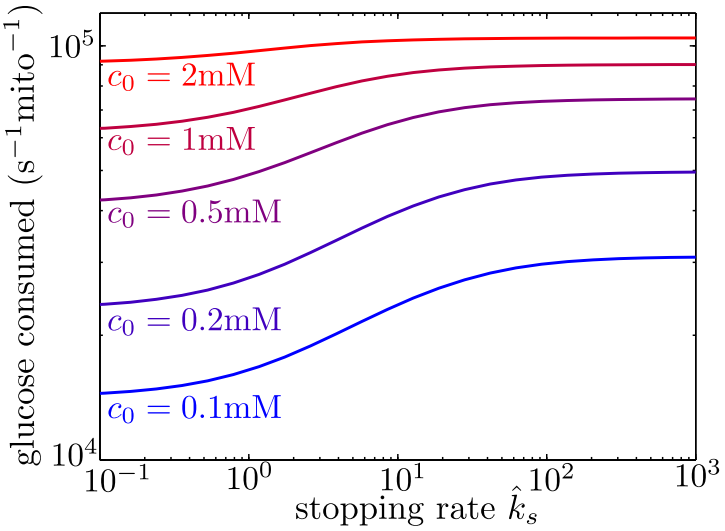

Figure 2.5. Mitochondrial stopping increases overall metabolic flux.
Total glucose consumption per mitochondrion, averaged over the full interval, is shown for different edge glucose concentrations (c_0) as a function of the mitochondrial stopping rate $\hat{k}_s$. The limit of small $\hat{k}_s$ corresponds to uniform mitochondria distribution. Parameters for the model are taken from Table I. Source data is provided in "Fig. 5 - source data". .

Ranvier.

2.3.3 Glucose-dependent halting can increase metabolic flux under physiological conditions

Localizing mitochondria to the glucose entry points is expected to increase the flux of glucose entering the cell, thereby potentially enhancing the overall metabolic rate. We calculate the overall effect of transport-based regulation on the net metabolic flux within the simplified model with localized glucose entry. Fig. 2.5 shows the effect of increasing mitochondrial stopping rates ($\hat{k}_s$) on the total rate of glucose consumption in the interval between nodes of glucose influx. At low $\hat{k}_s$ values, mitochondria are distributed uniformly throughout the interval. At high $\hat{k}_s$ values and at sufficiently low glucose concentrations, the mitochondria cluster in the regions of glucose entry, increasing the overall consumption rate by up to 40% at physiologically relevant glucose levels ($c_0 = 1$mM). We note that in hypoglycemic conditions, glucose levels can drop to 0.1mM [191], further increasing the magnitude of this effect.

In the case of limited glucose transport into the cell, intracellular glucose levels could be significantly below the concentrations outside the cell. Measurements of intracellular glucose in a variety of cultured mammalian cell types indicate internal concentrations within the range of $0.07 - 1$mM, up to an order of magnitude lower than glucose concentrations in the medium[85]. However, neuronal cells are known to express a particularly efficient glucose transporter (GLUT3)[193], and these transporters have been shown to be highly concentrated near the nodes of Ranvier[121, 169]. We therefore assume that glucose import into the nodes is not rate limiting for myelinated neurons in physiological conditions. Introducing a finite rate of glucose transport would effectively decrease the intracellular glucose concentration at the nodes c_0, increasing the enhancement in metabolic flux due to mitochondrial localization. In subsequent sections, we explore the role of limited glucose import in unmyelinated axons with spatially uniform glucose permeability.

2.3.4 Model for spatial organization in a glucose gradient

Extracellular brain glucose levels exhibit substantial regional variation, particularly under hypoglycemic conditions where more than ten-fold differences in local glucose concentrations have been reported[149]. Because individual neurons can traverse multiple different brain regions[131], a single axon can be subjected to heterogeneous glucose levels along its length. This raises the possibility that glucose-dependent mitochondrial localization can play a role in neuronal metabolic flexibility even in the case where glucose entry into the cell is not localized to distinct nodes. We thus extend our model to quantify the distribution of mitochondria in an axon with limited but spatially uniform glucose permeability that is subjected to a gradient of external glucose. This situation is relevant, for instance, to unmyelinated neurons in infant brains, as well as to *in vitro* experiments with neurons cultured in a glucose gradient[153].

In this model, the extracellular environment provides a continuous source of glucose whose influx is limited by the permeability of the cell membrane. Intracellular glucose dynamics are then defined by the reaction-diffusion equation

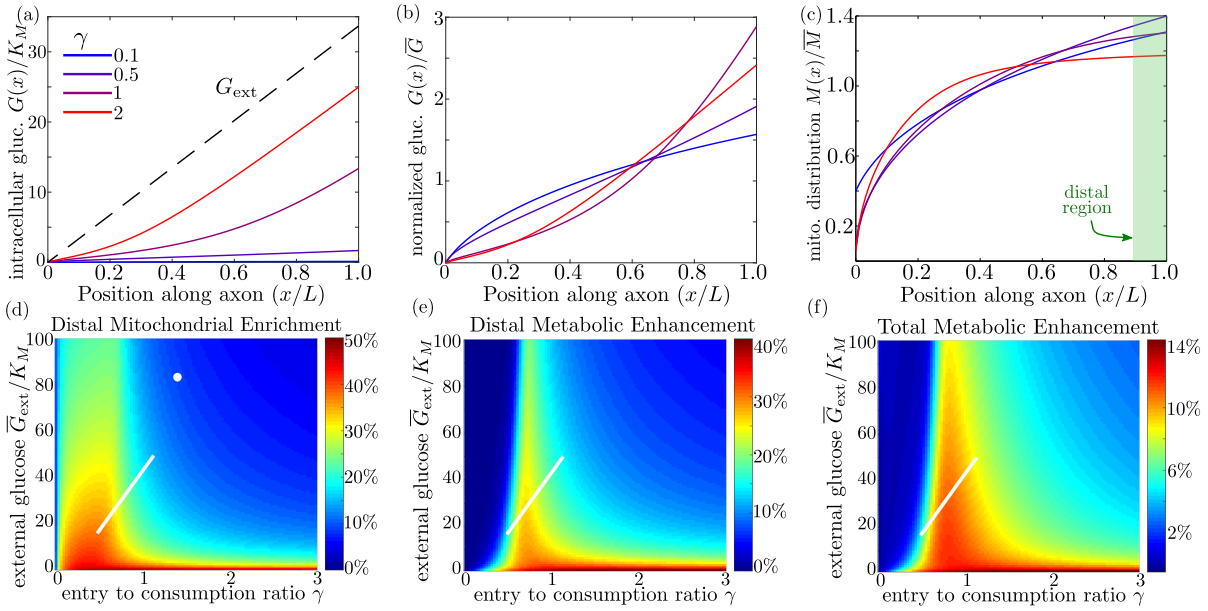

Figure 2.6. Mitochondrial and glucose organization in a region with uniform glucose permeability, subjected to a gradient of external glucose.

(a) Internal glucose levels for the steady state solution with $\overline{G}_{\text{ext}}/K_M = 17$ ($\overline{G}_{\text{ext}} = 0.5$ mM) and varying ratios of entry to consumption rate γ. Black dashed line shows external glucose levels. (b) Corresponding normalized distribution of internal glucose. (c) Corresponding normalized mitochondrial distribution. Shaded box indicates distal region used for calculating mitochondrial enrichment and metabolic enhancement in panels d-e. (d) Mitochondrial enrichment in the distal 10% of the interval at highest external glucose, compared to a uniform distribution. White dot marks estimated parameter values for neuronal cell culture experiments ($\overline{G}_{\text{ext}} = 2.5$mM). (e) Enhancement in metabolic flux in the distal region at high glucose, compared to a uniform mitochondrial distribution. (f) Enhancement in metabolic flux over full interval. White line in (d-f) shows estimated parameter range for physiological glycemic levels 0.5mM $< \overline{G}_{\text{ext}} <$ 1.5mM. Parameter values $\hat{k}_s = 19$, $\Delta\widehat{G}_{\text{ext}} = 2$ used throughout. Source data is provided in "Fig. 6 - source data 1-3".

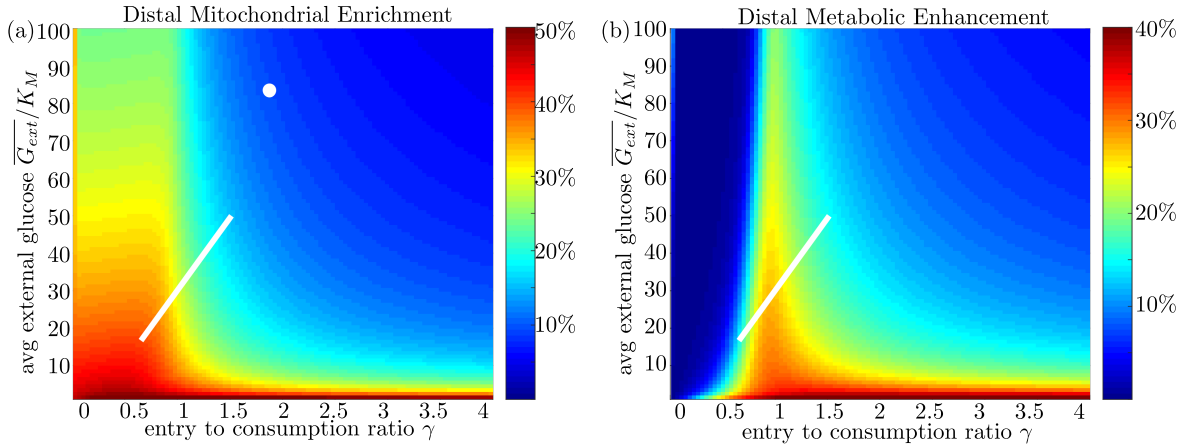

Figure 2.7. High stopping rate limit for model with uniform glucose permeability.
For the high k_s limit, we show (a) mitochondrial enrichment in the distal region and (b) metabolic enhancement in the distal region. In this limit, mitochondrial accumulation occurs for arbitrarily low values of γ as nearly all mitochondria are in the stopped state even at very low internal glucose concentrations. However, metabolic enhancement still occurs only within a narrow range of γ values.

$$\frac{dG}{dt} = D\frac{\partial^2 G}{\partial x^2} - k(x)G + P(x)\left(G_{\text{ext}}(x) - G\right), \tag{2.6}$$

where the first term corresponds to diffusive glucose spread, the second to a spatially varying metabolism of glucose, and the third to the entry of glucose into the cell. Here, G_{ext} is the external glucose concentration, and $P(x)$ is the membrane permeability to glucose, which we assume to depend in a Michaelis-Menten fashion on the difference between external and internal glucose concentration:

$$P(x) = \frac{(2/r)PK_{MP}}{K_{MP} + |G_{\text{ext}}(x) - G(x)|}, \tag{2.7}$$

where P is the spatially uniform permeability constant in units of length per time. This functional form incorporates two known features of glucose transporters: (1) they are bidirectional, so that the overall flux through the transporter at low glucose levels should scale linearly with the difference between external and internal glucose[27]; (2) neuronal glucose transporters saturate at high glucose levels (GLUT3 $K_{MP} \approx 3$mM[123], with an even higher saturation constant for GLUT4 [143]). When the difference in glucose levels is low, the overall flux of glucose entering

the cell reduces to $P(G_{\text{ext}}(x) - G(x))$. Mitochondria dynamics are defined as before (Eq. 2.4), and we again assume Michaelis-Menten kinetics for glucose metabolism by hexokinase localized to mitochondria (Eq. 2.2).

We note that the dynamics in Eq. 2.6 are governed by three time-scales: the rate of glucose transport down the length of the axon, rate of glucose consumption, and rate of glucose entry. The first of these rates becomes negligibly small in the limit $L \gg \sqrt{D(G+K_M)/(k_g\overline{M})}$. Because internal glucose levels can never exceed the external concentrations, in the range where $G_{\text{ext}} < 10\text{mM}$, the rate of diffusive transport should become negligible for $L \gg 150\mu\text{m}$. In the limit where intracellular glucose is much less than K_m, this criterion reduces to $\hat{\lambda} \ll 1$, indicating that glucose diffuses over a very small fraction of the interval before being consumed. The interval length L in this model represents an axonal length which can range over many orders of magnitude. We focus on axon lengths above several hundred microns, allowing us to neglect the diffusive transport of intracellular glucose (see Appendix A.3).

The steady-state glucose profile can then be determined entirely by the local concentration of mitochondria and external glucose. For a given mitochondrial density $M(x)$ and external glucose profile $G_{\text{ext}}(x)$, the corresponding intracellular glucose concentration can be found directly by solving the quadratic steady-state version of Eq.2.6 without the diffusive term. However, the steady-state mitochondrial distribution cannot be solved locally, because the limited number of mitochondria within the axon couples the mitochondrial density at different positions. We thus employ an iterative approach to numerically compute the steady-state solution for both glucose and mitochondrial density under a linear external glucose gradient $G_{\text{ext}} = G_{\text{min}} + (G_{\text{max}} - G_{\text{min}})\frac{x}{L}$ (see Materials and Methods).

For parameter combinations where intracellular glucose concentrations are above K_M but well below G_{ext}, the entry and consumption processes for glucose are both saturated. There is then a steep transition between two different regimes. In one regime, glucose entry exceeds consumption and internal glucose levels approach the external concentrations. In the other, consumption dominates and glucose levels drop below saturating concentrations. The key dimen-

sionless parameter governing this transition can be defined as the ratio of entry to consumption rates:

$$\gamma = \frac{2PK_{MP}\overline{G}_{\text{ext}}}{k_g\overline{M}r(K_{MP}+\overline{G}_{\text{ext}})}. \tag{2.8}$$

This ratio can be modulated in the cell either by recruiting varying amounts of glucose transporters (adjusting P) or changing the total amount of active hexokinase (adjusting $k_g\overline{M}$).

The remaining dimensionless parameters determining the behavior of this simplified model are the external glucose concentration relative to the hexokinase saturation constant ($\widehat{G}_{\text{ext}} = \overline{G}_{\text{ext}}/K_M$), the relative magnitude of the glucose gradient, $\Delta\widehat{G}_{\text{ext}} = (G_{\max} - G_{\min})/\overline{G}_{\text{ext}}$, the ratio of stopped to walking mitochondria $\hat{k_s} = k_s/k_w$, and the saturation constant for glucose transporters $K_{MP}/K_M \approx 96$. The last parameter is expected to remain approximately constant in neuronal cells. The average external glucose concentration and glucose gradient are expected to vary substantially depending on the glycemic environment to which the neuron is exposed. We note that $\Delta\widehat{G}_{\text{ext}}$ has a maximum possible value since the minimal glucose concentration cannot drop below 0. We proceed to analyze the limiting case where the glucose gradient is as steep as possible for any given value of average external glucose ($\Delta\widehat{G}_{\text{ext}} = 2$).

2.3.5 Mitochondrial arrest enables metabolic enhancement under glucose gradient

We quantify the amount of mitochondrial accumulation at the high glucose side of the domain by calculating the total mitochondrial density within the distal 10% of the interval compared to a uniform distribution, in analogy to experimental measurements[153]. Substantial enrichment in the high glucose region occurs when glucose entry into the cell cannot keep up with consumption ($\gamma \ll 1$) and the intracellular glucose levels drop below the hexokinase saturation concentration K_M, as can be seen in the glucose and mitochondrial distributions plotted in Fig. 2.6a-c. The interplay between external glucose levels and the entry / consumption rates

is illustrated in Fig. 2.6d. For external glucose concentrations well above K_M there is a sharp transition to mitochondrial enrichment at $\gamma < 1$. At the lowest levels of intracellular glucose, accumulation is again reduced because a very small fraction of mitochondria are found in the stopped state. In the limit of high k_s, mitochondrial accumulation would occur for arbitrarily low values of γ (Fig. 2.6S1). We note that because glucose entry and turnover are much faster than diffusive spread for biologically relevant parameter regimes, the model results do not depend on the cell length L (Appendix A.3).

Experimental measurements of mitochondrial enrichment in cultured neurons subjected to a gradient of 0 to 5mM glucose have indicated an approximately 20% enrichment in mitchondrial counts at the axonal region exposed to high glucose. We note that using published estimates of typical glucose permeability and mitochondrial glucose turnover for mammalian cells (Table 2.1) yields a ratio of entrance and consumption rates of $\gamma \approx 1.9$ for this experimental system. Because this ratio is above 1, we would not expect to see substantial mitochondrial enrichment. To result in the experimentally observed enrichment at high glucose, the ratio γ would need to be reduced by approximately a factor of 2, implying the existence of additional regulatory mechanisms. Modulation of γ could be achieved by either decreasing the number of glucose transporters in the cell (reducing P) or upregulating total hexokinase levels (increasing k_g). Neurons are believed to regulate both the density of glucose transporters and hexokinase activity in response to external glucose concentrations and varying metabolic demand[56, 168, 46]. In particular, adaptation to glycemic levels well above physiological values, as well as possibly reduced synaptic activity in a cultured environment, may result in downregulation of glucose transporters, lowering the value of γ. The discrepancy between model prediction and observed mitochondrial accumulation highlights the existence of additional regulatory pathways not included in the current model whose role could be explored in further studies that directly quantify glucose entry and consumption rates in cultured neurons.

Physiological brain glucose levels have been measured at 0.7mM - 1.3mM[132], with hypoglycemic levels dipping as low as 0.1mM and hyperglycemic levels rising up to 4mM[191].

Axons that stretch across different brain regions with varying glucose levels can thus be subject to a glucose gradient with $\overline{G}_{\text{ext}}$ on the order of 1mM (white line on Fig. 2.6d). We note that the physiological range overlaps substantially with the region of high mitochondrial accumulation, indicating that glucose-dependent halting can modulate mitochondrial distribution under physiologically relevant glycemic levels.

By accumulating mitochondria at the cellular region subjected to higher external glucose, the metabolic flux in that region can be substantially enhanced. In Fig. 2.6e we plot the enhancement in glucose consumption rates (compared to the case with uniformly distributed mitochondria) within the 10% of cellular length subjected to the highest glucose concentrations. Metabolic enhancement occurs within a narrow band of the γ parameter. The drop-off in enhancement at low values of the internal glucose concentration (low γ) is due to the coupling between glucose levels and mitochondrial localization. Specifically, mitochondrial accumulation at the region subject to high glucose concentration increases the local rate of consumption in that region, driving down local internal glucose levels. Consequently, the difference in internal glucose concentrations between the two ends of the cell is decreased when internal levels fall substantially below K_M (Fig. 2.6b), reducing the enhancement of metabolic flux. Although mitochondrial accumulation decreases metabolic flux in the low glucose region, the total rate of glucose consumption integrated throughout the cell is enhanced by up to approximately 14% when $\gamma \approx 1$ (Fig. 2.6f).

It is interesting to note that the typical physiological range of external glucose levels spans the narrow band of parameter space where metabolic enhancement is expected (white lines on Fig. 2.6e,f). These results implicate glucose-dependent mitochondrial stopping as a quantitatively plausible mechanism of metabolic flexibility, increasing metabolism in regions with high nutrient availability for axonal projections that span between hypoglycemic and euglycemic regions. The magnitude of this effect can be tightly controlled by the cell through modulating overall rates of glucose entry and consumption. Thus, by coupling mitochondrial transport to local glucose levels, whole-cell changes in hexokinase or glucose transporter recruitment can be harnessed to

tune the cell's response to spatially heterogeneous glucose concentrations.

2.4 Discussion

The minimal model described here provides a quantitative framework to explore the interdependence of glucose levels and mitochondrial motility and their combined effect on neuronal metabolic flux. Glucose-mediated halting of mitochondrial transport is shown to be a plausible regulatory mechanism for enhancing metabolism in cases with spatially heterogeneous glucose availability in the neuron.

We have quantitatively delineated the regions in parameter space where such a mechanism can have a substantial effect on mitochondrial localization and metabolic flux. Specifically, mitochondrial positioning requires both sufficient spatial variation in intracellular glucose and sufficiently low absolute glucose levels compared to the saturation constant of the hexokinase enzyme. In the case of tightly localized glucose entry (as at the nodes of Ranvier), intracellular spatial heterogeneity requires a small value of the dimensionless length scale for glucose decay ($\hat{\lambda} = \sqrt{DK_M/k_g\bar{M}L^2} \ll 1$). For physiologically estimated values, mitochondrial localization to the nodes is expected to occur for glucose levels below approximately 2mM, comparable to physiological brain glucose concentrations[132, 85]. In the case where glucose can enter homogeneously throughout the cell surface (as with unmyelinated axons), heterogeneity can arise from an external glucose gradient. We show that metabolic enhancement through mitochondrial positioning occurs in a narrow range of the key parameter $\gamma = (2PK_{MP}\overline{G}_{\text{ext}})/(k_g\overline{M}(K_{MP}+\overline{G}_{\text{ext}}))$, which describes the ratio of glucose entry to glucose metabolism, and that this narrow range intersects with physiological estimates.

The model developed here is intentionally highly simplified, encompassing a minimal set of parameters necessary to describe glucose-dependent mitochondrial localization. Other regulatory pathways that determine mitochondrial positioning are not included in this basal model. In particular, we do not consider here calcium-based transport regulation, which is known

to localize mitochondria to regions of synaptic activity[234, 216, 118, 119]. Upregulating OGT signaling in cultured cells has been shown to decrease the fraction of motile mitochondria by a factor of three, while reducing endogenous OGT nearly doubles the motile fraction, indicating that a substantial number of stationary mitochondria are stopped as a result of OGT activity[153]. Our model assumes the extreme case where all stopping events are triggered in a glucose-dependent manner, thereby isolating the effect of glucose heterogeneity. Stopping mechanisms dependent on neuronal firing activity could alter mitochondrial distribution in concert with glucose-dependent halting, increasing the density of mitochondria at presynaptic boutons or near areas of localized calcium influx as at the nodes of Ranvier[234]. We note that mitochondria have previously been shown to accumulate at spinal nodes of Ranvier in response to neuronal firing activity[49, 234]. The mechanism described here provides an additional driving force for mitochondrial localization near the nodes even in quiescent neurons.

Additional metabolic feedback loops, not included in our model, may result in a more complex dependence of mitochondrial stopping on glucose concentration. In particular, both the pentose phosphate pathway and glycolysis generate intermediates that feed back into UDP-GlcNAc production by the hexosamine biosynthetic pathway[98, 188]. Furthermore, several of the enzymes involved in the metabolic pathways linking glucose levels to Milton O-GlcNacylation may be regulated in a glucose-dependent manner. For example, the activity of the fructose-6-phosphate metabolizing enzyme GFAT is believed to be regulated by intermediates in the hexosamine pathway[202] and O-GlcNAc transferase (OGT) itself is directly regulated by UDP-GlcNAc levels[74]. Other enzymes, such as the de-GlcNAcylating enzyme OGA exhibit long term regulation of expression in response to altered glucose levels[240]. These regulatory mechanisms provide additional potential routes of metabolic control through mitochondrial positioning.

Several key parameters that regulate mitochondrial localization in response to glucose heterogeneity can be dynamically regulated in neurons. Specifically, the rate of glucose consumption ($k_g\overline{M}$) can be tuned by modulating the concentration or activity of hexokinase within

mitochondria or by altering total mitochondrial size and number. This parameter controls both the glucose decay length $\hat{\lambda}$ in the case of localized glucose influx and the ratio of glucose entry to consumption γ in the case of spatially distributed entry. We note that our model assumes hexokinase to be localized exclusively to mitochondria. The predominant form of hexokinase in the brain (HK1) is known to bind reversibly to the mitochondrial membrane, with exchange between a mitochondria-bound and a cytoplasmic state believed to contribute to the regulation of its activity[62]. Release of hexokinase into the cytoplasm would result in more spatially uniform glucose consumption, negating the metabolic enhancement achieved through mitochondrial localization.

An additional parameter known to be under regulatory control is the rate of glucose entry into the neuron (P). The glucose transporters GLUT3[193, 46, 220] and GLUT4[8] have been shown to be recruited to the plasma membrane in response to neuronal firing activity. Interestingly, transporter densities are themselves spatially heterogeneous, concentrating near regions of synaptic activity[8, 6]. The model described in this work quantifies the extent to which a locally increased glucose influx can enhance total metabolic flux, given the ability of mitochondria to accumulate at regions of high intracellular glucose.

A number of possible feedback pathways linking glucose distribution and mitochondrial positioning are not included in our basic model. For instance, hexokinase release from mitochondria into the cytoplasm (potentially altering k_g) is known to be triggered at least in part by glucose-6-phosphate, the first byproduct in glucose metabolism[36]. Chronic hypoglycemia has been linked to an upregulation in GLUT3 in rat neurons [206], which would in turn lead to an increased glucose uptake (P). The fraction of glucose funneled into the hexosamine biosynthetic pathway (incorporated within k_s) can also be modified through feedback inhibition of GFAT by the downstream metabolic product UDP-GlcNAc[110]. Such feedback loops imply that several of our model parameters (P, k_g, k_s) are themselves glucose-dependent and may become spatially non-uniform in response to heterogeneous glucose. Incorporating these effects into a spatially resolved model of metabolism would require quantifying the dynamics of both the feedback

pathways and mitochondrial positioning, and forms a promising avenue for future study.

Control of glucose entry and consumption underlies cellular metabolic flexiblity, and defects in the associated regulatory pathways can have grave consequences for neuronal health. Misregulation of hexokinase has been highlighted as a contributor to several neurological disorders, ranging from depression [167] to schizophrenia [185]. Neuronal glucose transporter deficiency has been linked to autism spectrum disorders[236] and Alzheimer's disease[116]. Furthermore, defects in mitochondrial transport, with the consequent depletion of mitochondria in distal axonal regions, contribute to peripheral neuropathy disorders[11].

Glucose-dependent mitochondrial localization provides an additional layer of control, beyond conventionally studied regulatory mechanisms, which allows the cell to respond to spatial heterogeneity in glucose concentration. Our analysis paves the way for quantitative understanding of how flexible regulation of metabolism can be achieved by controlling the spatial distribution of glucose entry and consumption.

2.5 Materials and Methods

2.5.1 Discrete mitochondria simulations

We simulate the internodal space of the axon, between localized nodes of glucose entry, as a one-dimensional domain for a reaction diffusion system with motile reaction sinks. The glucose concentration field is discretized over 100 equidistant points along the domain. Its dynamics are governed by the reaction diffusion equation (Eq. 2.1), evolved forward over time-steps of δt using the forward Euler method. Because forward Euler methods have stringent conditions for stability and convergence, we use a time-step that is much smaller than both the glucose decay time-scale and the time-scale associated with diffusion over our spatially discretized grid (see below).

The number of mitochondria in the domain is calculated according to $N = \overline{M}L\pi r^2 \approx 38$, where the mitochondrial density $\overline{M}$, internodal distance L, and axonal radius r are estimated from

published data (Table 2.1; Appendix A.1). The mitochondria are treated as discrete intervals of length $\Delta = 1\mu$m, with the position of each mitochondrial center updated at each timestep. Over each time step, every motile mitochondrion moves a distance of $\pm v\delta t$, (with transport velocity $v = 1\mu\text{m}/s$) and switches to a stationary state with probability $1-\exp(-k_s\delta t)$, where $k_s(x)$ is a function of the center position of that mitochondrion (Eq. 2.3). Mitochondria that reach within a distance of $\Delta/2$ from the ends of the domain are reflected, reversing their velocity while remaining motile. Analogously, every stationary mitochondrion switches to a motile state on each time-step with probability $1-\exp(-k_w\delta t)$. Processive walks are initiated with equal probability in either direction.

At any given time, the spatial density of mitochondria is calculated from the location of mitochondrial centers at positions $x_1,\ldots x_N$, according to $M(x) = n(x)/(\pi r^2\Delta)$, where

$$n(x) = \sum_{i=1}^{N} \left[\theta(x-x_i+\Delta/2) - \theta(x-x_i-\Delta/2)\right],$$

is the number of mitochondria overlapping spatial position x and θ is the Heaviside step function.

We integrate the simulation forward in time-steps of $\delta t = 0.2\frac{\Delta x^2}{D}$, where Δx is the spatial discretization. This time-scale is much smaller than the relevant decay time for glucose consumption $\left[\tau_g = \left(\frac{k_g\overline{M}}{K_M}\right)^{-1}\right]$. Using these small time-steps allows for stability and robust convergence with the forward Euler method. The simulation proceeds for 10^7 steps. Simulations are repeated 100 times to obtain the histogram shown in Fig. 2.2. Convergence to steady-state is established by comparing to calculations with the continuum model described in the subsequent sections.

2.5.2 Mitochondrial distribution for spatially varying stopping rate

For an arbitrary spatial distribution of stopping rates $k_s(x)$ the corresponding steady-state mitochondrial distribution can be calculated directly by solving the equations for mitochondrial

transport (Eq. 2.4):

$$\begin{aligned} S &= \frac{k_s(x)(W_- + W_+)}{k_w} \\ v\frac{dW_+}{dx} &= \frac{1}{2}k_s(x)(W_- - W_+) \\ v\frac{dW_-}{dx} &= \frac{1}{2}k_s(x)(W_- - W_+). \end{aligned} \tag{2.9}$$

Because our model assumes symmetry between anterograde and retrograde mitochondrial transport, as well as equal glucose concentrations at either boundary of the domain, we take $W_- = W_+$, implying that the population of walking mitochondria must be spatially constant. Consequently, the population of stopped mitochondria is proportional to the stopping rate ($S = Ck_s(x)/k_w$). The constant C can be calculated from the normalization condition,

$$\int_0^L M(x)dx = \int_0^L [W_-(x) + W_+(x) + S(x)]\,dx = \overline{M}L. \tag{2.10}$$

The overall steady-state distribution of mitochondria is then given by,

$$M(x) = W_-(x) + W_+(x) + S(x) = \frac{\overline{M}}{1 + \frac{1}{L}\int_0^L \frac{k_s(x)}{k_w}dx}\left[\frac{k_s(x)}{k_w} + 1\right] \tag{2.11}$$

.

Because the stopping rate is an explicit function of glucose concentrations $\left[k_s(x) = \frac{k_s G(x)}{K_M + G(x)}\right]$, this approach allows us to find the steady-state mitochondrial distribution for any fixed distribution of glucose.

2.5.3 Numerical solution for steady-state distributions with localized glucose entry

We solve for steady-state glucose and mitochondrial distributions using a numerical method that evolves the glucose concentration forward in time while explicitly setting the mitochondrial concentration to its steady-state value at each step.

The glucose distribution is initialized according to the steady-state solution for uniform consumption (Eq. 2.13). Mitochondrial density $M(x)$ is calculated from the glucose distribution according to Eq. 2.11 and Eq. 2.3. The glucose distribution $G(x)$, in turn, evolves according to the mitochondrial distribution as given by Eq. 2.1 and Eq. 2.2 . The glucose profile is integrated forward with a timestep $\delta t = 10^{-5}L^2/D$. The distributions are assumed to be converged once the root mean squared rate of glucose change drops below the minimal cutoff: $10^{-6}k_g\overline{M}$. Results of the continuous mitochondrial distribution model are shown to match the discrete mitochondria simulations (Fig. 2.2b). All subsequent analysis is done in the continuum limit.

2.5.4 Analytical solution for low glucose limit

We validate our numerical calculations by comparing to the analytically tractable solution in the limit of low glucose and nearly uniform mitochondrial distribution. In the limit of spatially uniform, linear consumption, the steady-state reaction-diffusion equation for glucose can be expressed as

$$0 = D\frac{\partial^2 G}{\partial x^2} - kG(x), \tag{2.12}$$

where $k = k_g\overline{M}/K_M$ is the constant consumption rate.

Assuming fixed glucose concentrations (c_0) at the boundaries of the domain, the steady-state glucose distribution is then given by

$$G(x) = \frac{c_0\cosh(\frac{x}{\lambda})}{\cosh(\frac{L}{2\lambda})}, \tag{2.13}$$

with $\lambda = \sqrt{\frac{D}{k}}$ defining the glucose decay length-scale. This quantity is a measure of how far glucose diffusively penetrates into the domain before being consumed by hexokinase. It is scaled by the size of the domain to give the dimensionless decay length scale $\hat{\lambda} = \sqrt{\frac{DK_M}{k_g\overline{M}L^2}}$ used as a key parameter in our model with localized glucose entry:

2.5.5 Steady-state distribution with uniform permeability in the slow diffusion limit

For the model with spatially uniform glucose permeability, we solve directly for the steady state distributions of glucose and mitochondria in the limit of slow diffusivity. When diffusion along the domain is slow compared to the timescales of glucose consumption and glucose import, the steady-state equation for glucose concentration is given by a simplified form of Eq. 2.6:

$$-k(x)G(x) + P(x)\left(G_{\text{ext}}(x) - G(x)\right) = 0. \tag{2.14}$$

Substituting $k(x) = \frac{k_g M(x) G(x)}{G(x)+K_M}$ and $P(x) = \frac{(2/r)PK_{MP}}{K_{MP}+|G_{\text{ext}}(x)-G(x)|}$, we get a quadratic equation in $G(x)$;

$$\left[1 - \frac{2PK_{MP}}{rk_gM}\right]G(x)^2 + \left[\frac{2PK_{MP}G_{ext}}{rk_gM} - \frac{2PK_{MP}K_M}{rk_gM} - G_{ext} - K_{MP}\right]G(x) + \left[\frac{2PK_{MP}K_MG_{ext}}{rk_gM}\right] = 0 \tag{2.15}$$

For a given mitochondrial profile, this quadratic equation is solved to find $G(x) = G(M(x))$. The mitochondrial distribution, $M(x)$ is then updated according to Eq. 2.11 and Eq. 2.3. We thus arrive at an iterative solution for $G(x)$ and $M(x)$.

2.6 Acknowledgements

Chapter 2, in full, is a reprint of the material as it appears in Agrawal, A., Pekkurnaz, G. and Koslover, E.F. “Spatial control of neuronal metabolism through glucose-mediated mitochondrial transport regulation”, *Elife*, 7, p.e40986, (2018). The dissertation author was the primary author of this paper.

Chapter 3

Optimizing mitochondrial maintenance in extended neuronal projections

3.1 Abstract

Neurons rely on localized mitochondria to fulfill spatially heterogeneous metabolic demands. Mitochondrial aging occurs on timescales shorter than the neuronal lifespan, necessitating transport of fresh material from the soma. Maintaining an optimal distribution of healthy mitochondria requires an interplay between a stationary pool localized to sites of high metabolic demand and a motile pool capable of delivering new material. Interchange between these pools can occur via transient fusion / fission events or by halting and restarting entire mitochondria. Our quantitative model of neuronal mitostasis identifies key parameters that govern steady-state mitochondrial health at discrete locations. Very infrequent exchange between stationary and motile pools optimizes this system. Exchange via transient fusion allows for robust maintenance, which can be further improved by selective recycling through mitophagy. These results provide a framework for quantifying how perturbations in organelle transport and interactions affect mitochondrial homeostasis in neurons, a key aspect underlying many neurodegenerative disorders.

3.2 Introduction

Mammalian neurons, with their complex and elongated architecture, pose a unique challenge for the delivery and maintenance of cellular components. Their relatively small cell body (soma) contains the nucleus and is responsible for synthesizing all the mRNA transcripts and a large portion of the proteins delivered to distal regions [64, 104]. For some proteins, local translation at distal outposts has been shown to play an important role in maintaining homeostasis [91, 87, 79]. However, this approach still requires the long-range delivery of mRNA from the nucleus [34, 174, 203]. Neurons thus rely on packaging components into vesicular organelles or RNA-protein granules, which are actively transported by molecular motors moving along microtubule tracks to the most distant regions of the cell. Such long-distance transport is critical for neuronal growth and repair [238, 17, 128], synapse formation and function [61, 114, 67], and synaptic plasticity [44, 235]. Furthermore, transport is required to maintain steady-state homeostasis of protein and mRNA levels. While neurons can have a lifespan of decades, the turnover of active mRNA is thought to happen on timescales of hours [19], and proteins are degraded over the course of a few days [43]. Efficient, perpetual delivery through transport from the cell body is thus required to replenish degraded components and maintain neuronal function.

A particular challenge for cellular homeostasis is supplying the spatially heterogeneous metabolic needs of neuronal projections. These projections, which stretch up to several hundred microns for dendrites and over a meter for axons, contain localized structures with elevated metabolic demand. For example, distal axonal structures such as presynaptic terminals and growth cones are known to have especially high ATP needs [73, 165]. In myelinated axons, the nodes of Ranvier can be separated by hundreds of microns [81] and contain high concentrations of ion pumps that are thought to correspond to locally elevated metabolic demand [31]. Postsynaptic dendritic spines also have high metabolic needs to support both ion pumping and local translation needed for proteostasis and plasticity [166, 72].

Reliable ATP production at sites of high metabolic demand is believed to rely on the localization of nearby mitochondria. These organelles serve as ATP-generating powerhouses and also help maintain Ca^{+2} homeostasis in the cytoplasm. Locally stationed mitochondria are a key source of fuel to power activity-dependent protein synthesis in dendritic compartments [166]. Mitochondria are also known to accumulate in presynaptic terminals [186] and in juxtaparanodal regions next to nodes of Ranvier in myelinated axons [234, 147]. Mitochondria are manufactured primarily in the soma [40] and delivered throughout neuronal projections via motor-driven transport [135, 181]. Delivery of mitochondria to specific regions relies on localized signals that trigger halting and switching into a stationary state. Several mechanisms for stopping motile mitochondria have been identified [181], including Ca^{+2}-dependent immobilization [216], glucose-dependent arrest [153], and syntaphillin-based anchoring [89]. Interestingly, 60-90% of axonal mitochondria are observed to be stationary, while the remainder are roughly equally split between an anterograde and retrograde motile population [181].

Mitochondria are one of many neuronal components whose delivery relies on local stop signals rather than a global addressing system. Dense core vesicles carrying neuropeptides [226] and RNA-protein particles [44] are distributed by sporadic capture at sequential synaptic sites as they circulate through the dendrites. Such delivery systems have been described by a "sushi belt model", where local sites trigger removal of components from an effective constantly moving conveyor belt [44, 223]. Quantitative analysis of the sushi belt model indicates that these systems face severe trade-offs between speed and accuracy, so that frequent halting interferes with the ability of transported components to reach the most distal regions [223]. The efficiency of a sushi-belt delivery system for steady-state replenishment of degrading components has not previously been addressed, and forms a key aspect of the current work.

The placement of stationary mitochondria at distal regions raises a challenging problem of "mitostasis" (mitochondrial homeostasis) [135]. Mitochondria are known to age over time, decreasing their membrane potential and ATP production efficiency [141], possibly as a result of damage caused by reactive oxygen species [10]. Defects in mitochondrial transport and

quality control are associated with a variety of neurological diseases, including Alzheimer's, Huntington's, and Parkinson's disease [187, 82]. Individual mitochondrial proteins have typical half-lives in the range of 2-14 days [43, 214]. Because most mitochondrial proteins are encoded in the nucleus, this implies that a distally stationed mitochondrion will experience significant degradation of its protein complement over the days to weeks time-scale. While local translation may replenish some of this protein content, not all mRNAs are found outside the soma [25], and the protein synthesis capacity of the axon is only a small fraction of that in the cell body [104]. Maintenance of a healthy population of mitochondria thus requires the continual delivery of new mitochondrial material to distal outposts. While some of this delivery could be accomplished by vesicular transport followed by local import, most nuclear-derived mitochondrial content is believed to be transported by a motile population of mitochondria themselves [135, 181].

Two main qualitative models have been proposed for the replenishment of aging neuronal mitochondria through long-range transport [135]. One, termed the 'Changing-of-the-Guard' (CoG) model, relies on individual mitochondria switching between the stationary and the motile pools. This enables newly synthesized mitochondria moving anterograde from the cell soma to halt at regions of high metabolic demand, while stationary mitochondria begin moving again to reach other regions or return to the soma for recycling. An alternative approach is the 'Space Station' (SS) model, in which a pool of mitochondria remains permanently stationed at distal sites. In this model, new protein components are delivered by passing motile mitochondria that undergo transient fusion and fission events with the stationary organelles.

Fusion and fission dynamics enable the exchange of membrane and matrix contents between distinct mitochondria [222, 215, 23]. In certain cell types, fusion allows the formation of extended mitochondrial networks that have been hypothesized to contribute to the efficient mixing of components that determine mitochondrial health [78, 213]. In neuronal axons, extensive fusion into a mitochondrial network is not observed but transient kiss-and-run events, consisting of a rapid fusion and fission cycle between two passing mitochondria, can nevertheless allow for component exchange [115, 184].

Neuronal mitostasis is also facilitated by a recycling pathway termed "mitophagy" [231]. In this pathway, unhealthy mitochondria with low membrane potential are marked by an accumulation of protein kinase PINK1 which recruits ubiquitin ligase Parkin, leading to ubiquitination of the mitochondrial surface [181, 231]. Autophagosomes (originating primarily at distal cell tips) move in the retrograde direction, engulf tagged damaged mitochondria, and carry them back to the cell body for recycling [120, 135].

Past theoretical studies of mitochondrial maintenance have focused on systems with extensive mitochondrial fusion and asymmetric fission [138, 150]. When mitochondrial health is determined by discrete factors in low copy numbers, fission events can stochastically result in particularly unhealthy daughter mitochondria that can then be targeted for degradation through mitophagy. The combination of discrete health units and selective autophagy has been shown to be sufficient for maintaining a healthy mitochondrial population [138, 150]. Recent studies have also begun to explore the role of spatial distribution, with randomly directed active transport and proximity-dependent fusion [150]. However, no quantitative model has yet attempted to address mitochondrial maintenance in the uniquely extended geometry of neuronal projections. This cellular system relies on long-range mitochondrial transport and faces the challenge of positioning mitochondria at specific distal regions of high metabolic demand.

In this work, we develop quantitative models for the coupling between mitochondrial transport and mitochondrial homeostasis in neuronal projections. We treat mitochondrial health as a continuously decaying parameter along the axon and assume that the generation of some of the critical mitochondrial material essential for health is limited to the cell body. Our models encompass both the 'Space Shuttle' and the 'Changing-of-the-Guard' qualitative mechanisms for mitochondrial exchange. In contrast to past work [150], we focus not only on total mitochondrial health, but also on the distribution of healthy mitochondria among localized distal regions of high metabolic demand. The balance between mitochondrial transport and localization, in the face of decaying mitochondrial health, serves as a bridge between spatially-resolved models of neuronal distribution [223, 226] and global models of mitochondrial maintenance [138, 150].

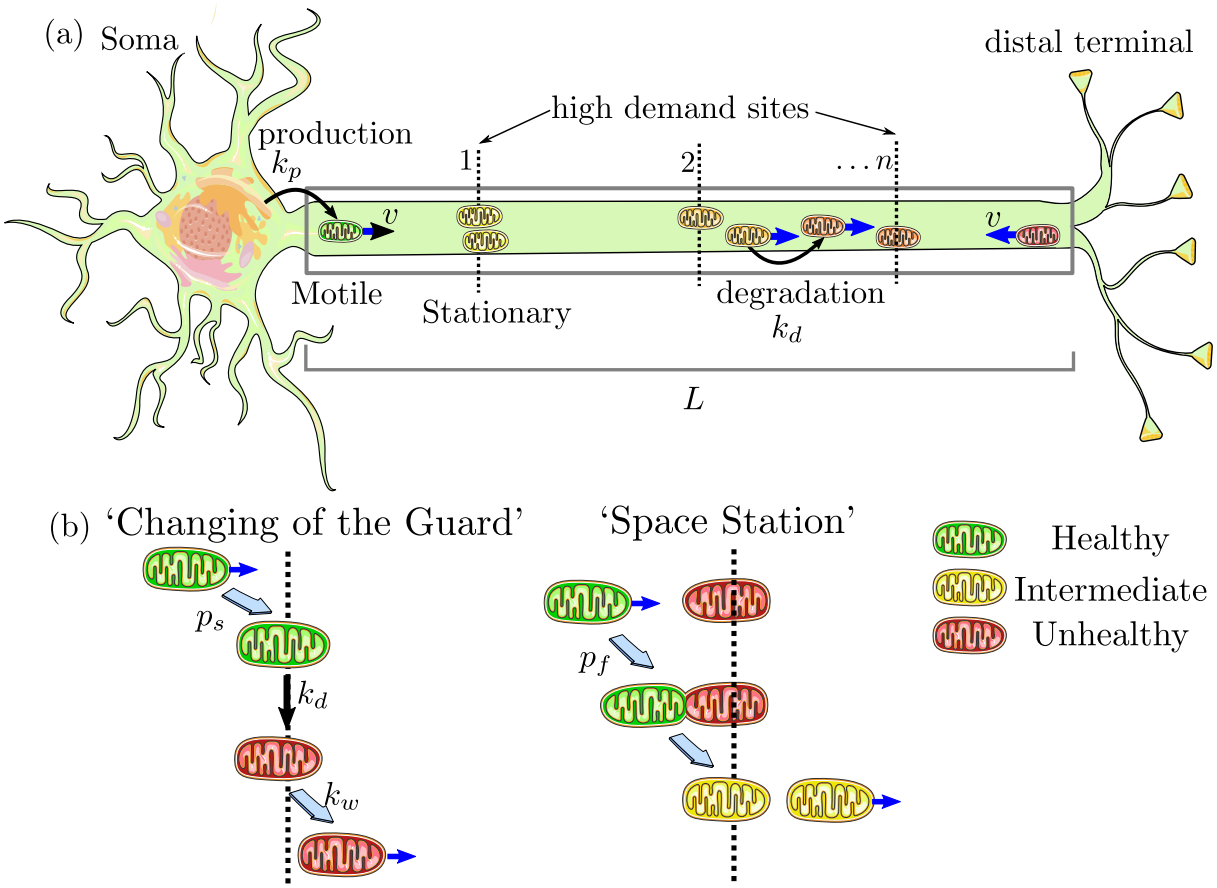

Figure 3.1. Schematic of quantitative models for mitochondrial maintenance in long neuronal projections.
(a) Mitochondria are produced at the soma at rate k_p, move processively with velocity v, and can stop at one of n discrete sites with high metabolic demand. Mitochondrial health degrades continuously with rate k_d. Gray box represents the modeled linear domain of length L. (b) Two models for mitochondrial exchange at demand sites. In the CoG model, stationary mitochondria re-enter the motile population with rate k_w while passing motile mitochondria stop with probability p_s. Stopping and restarting rates are independent of mitochondrial health; on average, however, restarting mitochondria will be less healthy than when they first stopped at the site, due to degradation in the stationary state. In the SS model, transient fusion events occur with probability p_f each time a motile mitochondrion passes a permanently stationary one[1].

We leverage both analytically tractable mean-field methods and discrete stochastic simulations to explore the equivalence between the SS and CoG mechanisms, delineate the parameter values that maximize mitochondrial health, and establish the existence of an optimum health threshold for mitophagy. This modeling effort fills a gap in our existing understanding of how neurons accomodate the trade-offs inherent in maintaining mitochondrial homeostasis while positioning mitochondria in regions far distant from the primary site of protein and organelle biogenesis.

3.3 Model Development

Two inherent constraints pose a challenge for maintaining distal mitochondrial outposts in a linearly extended region such as mammalian axons. First, mitochondrial health is assumed to be dependent on components (*eg:* proteins) that degrade rapidly compared to the cell lifespan and must be manufactured primarily in the cell soma at one end of the domain. The limitation of long-range transport from the soma can, in part, be bypassed by local protein translation, a phenomenon whose role has been increasingly appreciated in recent years [91, 87, 79]. Local protein synthesis can both maintain distal levels of fast-degrading proteins and allow for rapid response to changing local conditions[79, 60]. It should be noted, however, that local translation shifts the burden of transport and maintenance to mRNA, which tends to have even shorter lifetimes than many proteins[229, 180, 204]. We briefly explore the contribution of local translation to our model in a subsequent section, but focus primarily on mitochondrial health components that must be transported from the cell body.

A second key assumption is the existence of discrete "demand sites" interspersed throughout the domain, which have a particularly high need for a healthy population of localized mitochondria. For simplicity, we treat the demand sites as very narrow slices of the domain and focus on mitochondrial health specifically within those slices – an extreme form of spatial heterogeneity in metabolic demand. In the opposite extreme of wholly homogeneous metabolic

demand, the optimum maintenance strategy becomes simple: all mitochondria should move back and forth through the cell as rapidly as possible (within the limits of other constraints such as energetic requirements of transport) in order to ensure frequent replenishment of proteins at the cell soma.

In a system with discrete demand sites, optimizing metabolism requires the establishment of a population of stationary mitochondria specifically at those sites. However, this stationary population must be continuously replenished by a flux of either new proteins or entirely new mitochondria. We develop two quantitative models for mitochondrial replenishment (the SS and CoG model, illustrated in Fig. 3.1), in keeping with recent qualitative proposals for mitochondrial maintenance mechanisms [135].

In both cases, we assume that there are n discrete point-like demand sites at positions x_i, placed at equal separations over a linear domain of length L (Fig. 3.1a). This long linear domain mimics the extended axonal regions imaged in cell cultures [153] and serves as a simplification that enables us to focus on the interplay of dynamic processes for determining mitochondrial homeostasis. The effect of more complicated branched geometries observed *in vivo* is explored briefly in Supporting Information.

We treat individual mitochondrial health as a continuous quantity that is set to 1 when the mitochondrion leaves the cell body and decays exponentially with constant rate k_d as it travels down the axon. This health can be thought of as proportional to the copy number of an unspecified critical mitochondrial protein that is manufactured in the soma and is turned over during the lifetime of the mitochondrion. Other studies have also focused on the membrane potential and the accumulation of mutations in mitochondrial DNA as markers for mitochondrial health [138, 150]. With an appropriate change of units, the mitochondrial health in our model can equivalently represent any of these quantities, requiring only that they change in a continuous manner, with a single well-defined decay rate. Although a variety of factors may contribute to mitochondrial aging [94], we include only one decay rate for a single limiting health factor in our simplified model. More complicated systems that incorporate multiple decaying components

or different decay rates for the more metabolically active stationary mitochondria versus motile mitochondria are left for future expansions of the basic model. For clarity of exposition, we will assume that health corresponds to protein content in the remainder of the discussion.

The metabolic health at each demand site (H_i) is given by the total protein content for all mitochondria stationed at the site. Since each site is assumed to be very narrow (on the order of a few microns in an axonal length of mm to cm), the motile mitochondria spend negligible time at these sites and can be neglected from our calculations of demand site health. We consider two utility functions for overall metabolic health. The first is $\langle H \rangle = \frac{1}{n}\sum_{i=1}^{n} H_i$, the average health over all demand sites. The second is the health level at the most distal demand region (H_n), which serves as the lowest value across all the sites. Optimizing $\langle H \rangle$ requires maximizing the sum total metabolic rate in many regions of interest. Such an optimum could correspond to an uneven distribution of mitochondrial health between individual regions, with the distal demand sites being poorly supplied, while the proximal sites maintain a high health level. By contrast, optimizing H_n ensures that each individual region exhibits, to the greatest extent possible, a high level of mitochondrial health. Increasing the total number of mitochondria in the domain (M) will predictably raise both metrics. At the same time, requiring a fixed total number of mitochondria to service a greater number of demand sites should decrease the average health at each site. Consequently, we normalize the demand-site health levels by the total number of mitochondria per site:

$$\widehat{H}_i = H_i/(M/n), \quad \left\langle \widehat{H} \right\rangle = \frac{1}{n}\sum_{i=1}^{n} \widehat{H}_i \tag{3.1}$$

An individual mitochondrion can either be motile (moving with velocity $\pm v$) or stationary (at one of the demand sites). For simplicity, we neglect transient pausing of motile mitochondria and treat them as having a constant effective velocity outside of the demand regions. In keeping with experimental observations of axonal mitochondria [218], a motile mitochondrion is assumed to move processively in the anterograde or retrograde direction, with no switching of directional-

ity in the bulk of the domain. This assumption is relaxed in the Changing-of-the-Guard model, where stationary mitochondria can restart in either the anterograde or retrograde direction. The fate of mitochondria when they reach the terminus of an axon may involve some combination of local degradation [7] and recirculation towards the soma [126, 133, 24]. Given that the retrograde and anterograge flux of mitochondria are similar in axons [153, 160, 133], we assume that most of the organelles return to the cell body for recycling. Modeled mitochondria that reach the end of the domain (length L) are thus assumed to instantaneously switch to retrograde motion. A retrograde mitochondrion that returns to the soma at $x = 0$ is removed from the domain. To maintain a steady-state total mitochondrial number, anterograde mitochondria with full health are produced at the somal end with rate k_p.

The difference between the two models lies in the ability of individual mitochondria to switch between stationary and motile pools or to exchange protein content with other mitochondria, as described below.

3.3.1 Changing-of-the-Guard (CoG) model

One mechanism for maintaining a healthy population of localized mitochondria is by allowing occasional interchange between the pool of motile mitochondria and those stationed at demand regions. In the absence of fusion and protein exchange, motile mitochondria are generally younger and healthier than stationary ones, and the latter must be removed and recycled sufficiently quickly to maintain overall mitochondrial health at the regions of interest.

The simplest version of this model assumes that the rate of restarting stationary mitochondria is independent of their health or demand site position along the axon. An expanded version that incorporates mitophagy to selectively remove unhealthy mitochondria is considered in a subsequent section. Here, we assume each moving mitochondrion has a constant probability p_s for switching to the stationary state each time it passes a demand region. A stationary mitochondrion restarts motility with fixed rate constant k_w. Upon re-entering the motile state, it is equally likely to move in either the anterograde or retrograde direction. Stochastic agent-based

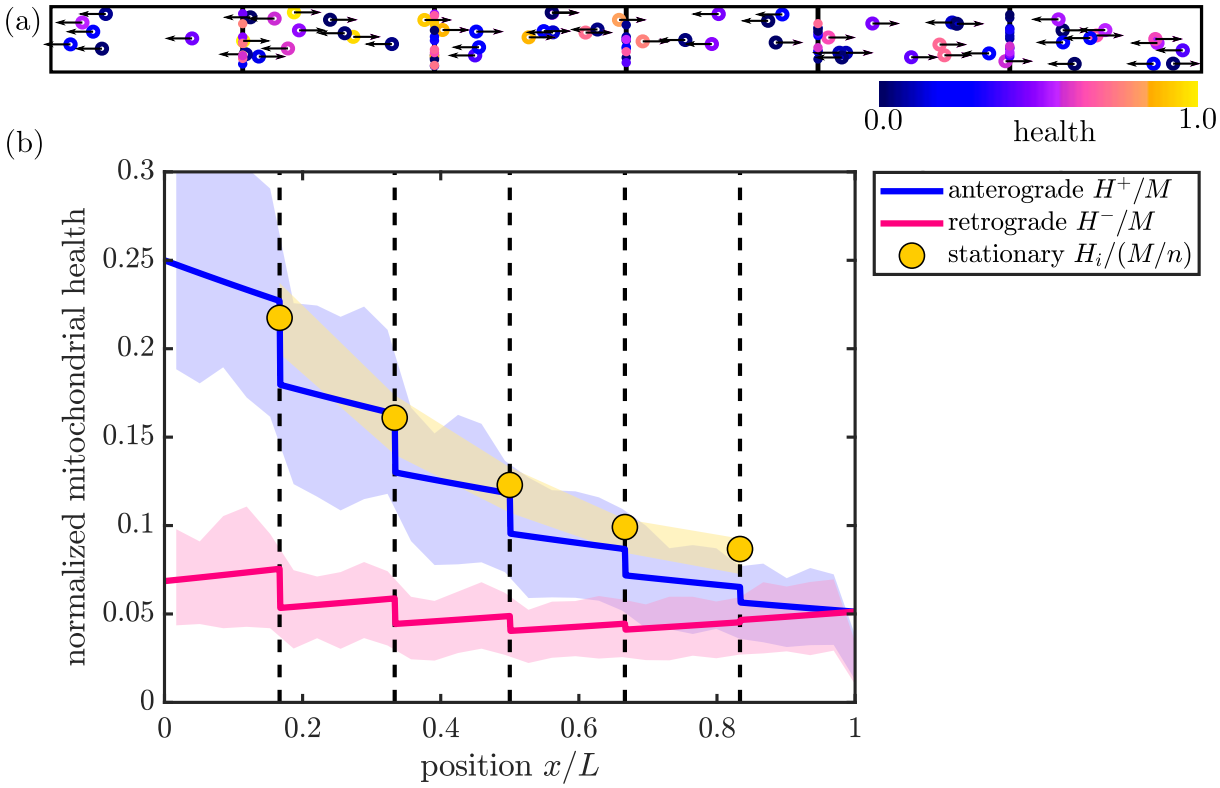

Figure 3.2. Comparison of mean-field and discrete stochastic models.
(a) Snapshot of stochastic simulation of the CoG model, with $M = 100$. (b) Steady-state solution for mitochondrial health in the CoG model (Eq. 3.2). Solid curves show linear density of mitochondrial health in anterograde (blue) and retrograde (magenta) mitochondria, normalized by total number of mitochondria in the domain. Yellow circles show total health at each of the discrete demand sites (dashed black lines), normalized by the total number of mitochondria per region. Shaded regions show corresponding quantities from discrete stochastic simulations (mean $\pm$ standard deviation) with $M = 1500$ mitochondria in the domain. Parameters used in (a) and (b): $n = 5, p_s = 0.4, f_s = 0.5, k_d L/v = 0.6$. Corresponding results for the SS model are provided in Supporting Information (S4 Fig).

simulations of this model are illustrated in Fig. 3.2a and Supporting Video S1.

A mean-field description of this model tracks the behavior of $H^{\pm}(x,t)$ (the linear density of mitochondrial health moving in the anterograde (H^{+}) and retrograde (H^{-}) directions) and H_i (the total health of stationary mitochondria at demand site i). These quantitites evolve according to the following set of equations:

$$\frac{dH^{\pm}}{dt} = \mp v\frac{\partial H^{\pm}}{\partial x} - k_d H^{\pm} \tag{3.2a}$$

$$\frac{dH_i}{dt} = v p_s \left[H^{+}(x_i^{-}) + H^{-}(x_i^{+})\right] - (k_d + k_w)H_i \tag{3.2b}$$

$$vH^{\pm}(x_i^{\pm}) = vH^{\pm}(x_i^{\mp})(1-p_s) + \frac{1}{2}k_w H_i \tag{3.2c}$$

$$H^{+}(L) = H^{-}(L) \tag{3.2d}$$

$$vH^{+}(0) = k_p. \tag{3.2e}$$

Equation 3.2a describes transport and decay of health (or protein content) in motile mitochondria. The distributions $H^{\pm}(x,t)$ are continuous on each interval (x_i, x_{i+1}), with discontinuities at the demand sites. Equation 3.2b encompasses switching between the stationary and motile populations, with $H^{\pm}(x_i^{-}), H^{\pm}(x_i^{+})$ referring to the limit of the distribution approaching the i^{th} site from the negative and from the positive side, respectively. Equation 3.2c gives the boundary condition at each demand site, where the flux of outgoing proteins from one side of the site must equal the flux of incoming proteins that pass without stopping from the other side, as well as the flux of stopped proteins that re-enter the motile state in that direction. Equation 3.2d describes switching of anterograde to retrograde motile mitochondria at the distal end of the domain. Finally, Eq. 3.2e gives the production rate of healthy mitochondria at the proximal end of the domain, assuming a health level of 1 for each newly-made mitochondrion.

The distribution of mitochondria themselves obeys the same set of equations (Eq. 3.2) with the k_d terms removed. We define ρ as the steady-state density of all motile mitochondria and S as the steady-state number of stationary mitochondria at each demand site. At steady state,

ρ is constant throughout the domain and S is the same in all demand sites, with

$$\rho = 2k_p/v, \quad S = v\rho p_s/k_w. \tag{3.3}$$

The total number of mitochondria in the domain is given by $M = \rho L + nS$. We use the total mitochondria M as a control parameter in our models, allowing k_p to vary as needed in order to maintain a given value of M. This approach represents a system where the total mitochondrial content in the domain is limited, so that increasing the number of stationary mitochondria comes at the expense of having a smaller motile population. The steady-state fraction of mitochondria in the stationary pool is defined as f_s and can be expressed as

$$f_s = \frac{nS}{M} = \frac{nvp_s}{Lk_w + nvp_s}. \tag{3.4}$$

The quantity f_s encompasses the trade-off between health replenishment by motile mitochondria and metabolic servicing of localized sites by stationary mitochondria, making it a convenient control parameter to explore this balance throughout the rest of our study.

At steady state, Eq. 3.2 can be solved analytically to give the distribution of mitochondrial health throughout the domain and at each demand site (Fig. 3.2b; see Materials and Methods for details). The mean-field model accurately describes the steady-state distributions when averaged over many realizations of stochastic trajectories for discrete mitochondria (Fig. 3.2b).

In each of the regions between demand sites, the steady-state anterograde protein density drops exponentially as $e^{-xk_d/v}$ with distance from the soma. The reverse relationship holds for retrograde-moving protein density, which decreases exponentially towards the soma. It should be noted that the overall mitochondrial health decreases with increasing distance from the soma – a fundamental consequence of long-range transport and continual protein turnover. Interestingly, a modest correlation between mitochondrial aging and distance from the nucleus has been experimentally observed in hippocampal neurites [52]. Furthermore, some measurements

indicate that retrograde moving mitochondria have lower health than anterograde ones[178] as also seen in Fig. 3.2.

3.3.2 Space Station (SS) model

An alternate approach to mitochondrial homeostasis relies on maintaning a pool of permanently stationed mitochondria in each demand region, whose contents can be replenished by transient fusion and fission with the motile population. Such transient 'kiss-and-run' events have been observed to allow for exchange of mitochondrial membrane and matrix proteins in H9c2 and INS-1 cells [115].

In our quantitative Space Station model, permanently stationary mitochondria are placed at the high demand sites, with $S = f_s M/n$ mitochondria per site. We assume the mitochondria maintain their discrete identities following a transient fusion/fission event, and that the protein content of the two mitochondria is fully equilibrated in each such event. Every time a motile mitochondrion passes a demand site, it has the opportunity to fuse with each of the stationary mitochondria present at that site, in sequence. Each transient fusion/fission event is successful with probability p_f, and the choice to fuse with each stationary mitochondrion is independent of health levels or prior fusion events. Following an instantaneous fusion/fission cycle, the health levels of the mitochondria are equilibrated, so that a protein in a motile mitochondrion has probability $p_f/2$ of switching to a stationary one each time there is a passage event. The rate at which a stationary protein re-enters a motile state in this model is given by $p_f/2$ times the flux of motile mitochondria passing the stationary organelle containing that protein. At steady state, this gives an effective restarting rate of

$$\widehat{k}_w = \frac{p_f}{2} v\rho = \frac{p_f v M(1-f_s)}{2L}, \tag{3.5}$$

where ρ is the linear density of motile mitochondria and f_s is the fraction of mitochondria in the permanent stationary state.

The mean-field equations for the SS model are derived in the Methods section. For the case with only one mitochondrion per site ($S = 1$), they are mathematically equivalent to the CoG model, with the variable replacements $p_s \to p_f/2$ and $k_w \to \widehat{k}_w$.

Stochastic simulations of the SS model with discrete mitochondria are illustrated in Supporting Video S2, and the resulting steady-state mitochondrial health matches well to the mean-field model (S4 Fig).

3.3.3 Model comparison

In order to compare the efficiency of mitochondrial maintenance via the CoG and SS models, we must first consider the different control parameters involved. Parameter definitions for both models are summarized in the Methods section. The parameters k_d (protein decay rate), M (total mitochondria), N (number of demand sites), v (motile mitochondria speed), and L (domain length) play the same role in both models. The CoG model is further parameterized by k_w (restarting rate for a stationary mitochondrion) and p_s (stopping probability for motile mitochondrion at each demand site). The SS model, on the other hand, has the parameters S (fixed number of stationary mitochondria per site) and p_f (probability of fusion with each stationary mitochondrion). These last two parameters define two key features of the maintenance mechanism: the steady-state fraction of mitochondria in the stationary pool (f_s), and the probability that a protein within a motile mitochondria will transition into a stationary state while passing each demand site ($\widehat{p}_s$). If these two control parameters are fixed, then for the CoG model we have $p_s = \widehat{p}_s$ and f_s given by Eq. 3.4. For the SS model, we set $f_s = nS/M$ directly. Because a motile mitochondrion has the opportunity to fuse sequentially with multiple stationary organelles at each demand site, the overall probability that a protein will transition to a stationary state at that site is given by

$$\widehat{p}_s = 1 - (1 - p_f/2)^S, \tag{3.6}$$

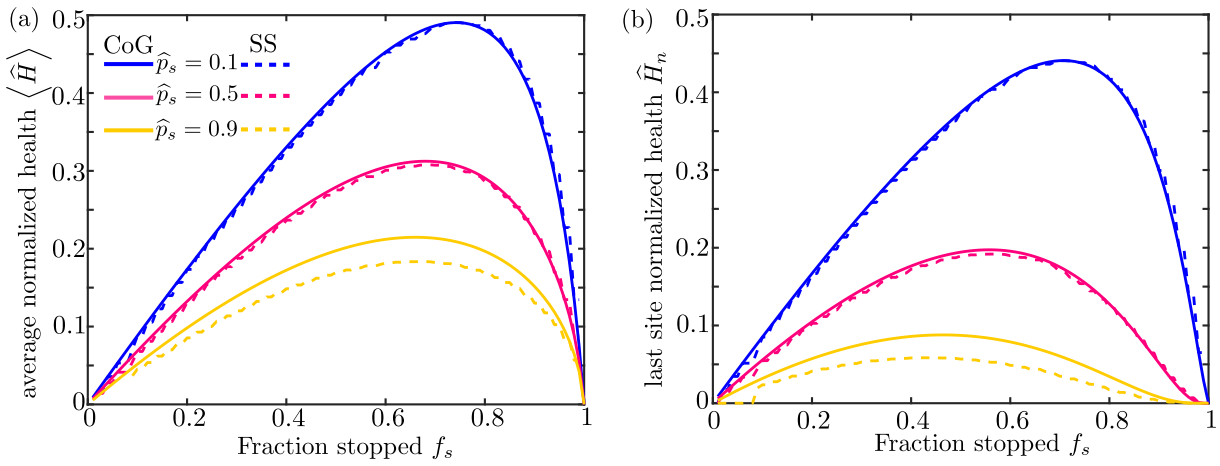

Figure 3.3. Comparison of mitochondrial maintenance models for matched parameter values. (a) Steady-state normalized mitochondrial health averaged over all demand regions is computed with the CoG model (solid lines) and the SS model (dashed lines) as a function of the fraction of stopped mitochondria (f_s) for three different values of the effective protein stopping probability $\widehat{p}_s$. (b) Corresponding plots of the normalized health in the most distal demand site, for both models. All values are computed with $M = 1500$, $\widehat{k}_d = 0.06$, and $n = 30$.

allowing a corresponding p_f value to be set for each effective stopping probability $\widehat{p}_s$.

When there is just one mitochondrion stationed in each demand site ($S = 1$), the two mean-field models become mathematically identical for fixed values of f_s and $\widehat{p}_s$. In general, the two models give very similar results so long as the stopping probability at each demand site is small ($\widehat{p}_s \lesssim 0.5$), as shown in Fig. 3.3. In this limit, $p_f \approx 2\widehat{p}_s/S$ and $\widehat{k}_w \approx k_w$ (from Eq. 3.4–3.5). For large values of $\widehat{p}_s$, the SS model is seen to yield slightly lower mitochondrial health than the CoG model (Fig. 3.3). It should be noted that for a fixed value of f_s, the SS model can only reach a limited maximum value of the effective stopping probability $\widehat{p}_s$. In fact, even if fusion events occur with each stationary mitochondrion ($p_f = 1$), a motile mitochondrial component always has a non-zero chance of continuing in its motile carrier rather than being left behind at the demand site. In the remainder of this work, we focus primarily on low values of $\widehat{p}_s$, a regime where the two models give essentially equivalent mean-field results.

To reduce the number of relevant model parameters, we can apply dimensional analysis, non-dimensionalizing all length units by the domain length L, and time units by L/v (the time for a motile mitochondrion to traverse the domain). The remaining dimensionless parameters are

the non-dimensionalized decay rate $\widehat{k}_d = k_d L/v$, the number of mitochondria in the domain M, the number of demand sites n, the fraction of mitochondria in the stationary population f_s, and the effective protein stopping probability at each demand site $\widehat{p}_s$.

In the CoG model, the total number of mitochondria is directly proportional to the production rate k_p, which sets the boundary condition at the proximal edge of the domain (Eq. 3.2e). Consequently, the normalized health values $\left\langle \widehat{H} \right\rangle$ and $\widehat{H}_n$ (which are scaled by the number of mitochondria per site) are independent of the total number of mitochondria in the system. The same relationship is seen for the SS model (S5 Fig). The chosen normalization embodies the assumption that the total amount of mitochondrial material in the cell is limited by other constraints, and that we are interested in modeling the overall mitochondrial health for a particular fixed number of total mitochondria.

In both maintenance models, mitochondrial proteins are removed from the system via two mechanisms: they undergo decay (with rate $\widehat{k}_d$) or they are recycled in the soma when a motile mitochondrion returns to its starting point. The total protein content in the system therefore depends on the time-scale for a given protein to return to the soma, and hence on the number of stops made by a given protein in the domain. The average total number of stops during a protein's back and forth journey through the cell is given by $N_s = 2\widehat{p}_s n$. As shown in Figure 3.4, it is this parameter rather than the specific number of regions n and stopping probability p_s that primarily determines the mitochondrial health at each demand site.

For the maintenance models proposed here, there are thus three primary parameters of relevance: the steady-state fraction of stationary mitochondria f_s, the number of stops expected for an individual protein while moving along the domain N_s, and the dimensionless protein decay rate $\widehat{k}_d$. The fraction f_s embodies the trade-off between mitochondrial transport and localization at distal sites. The number of stops N_s quantifies how often proteins exchange between the mobile and stationary populations. The dimensionless decay rate $\widehat{k}_d$ indicates how much health decay is expected for a mitochondrion that moves without stopping down an entire axon. Its value depends on the protein lifetime (a few days for mitochondrial proteins [214, 43]), the

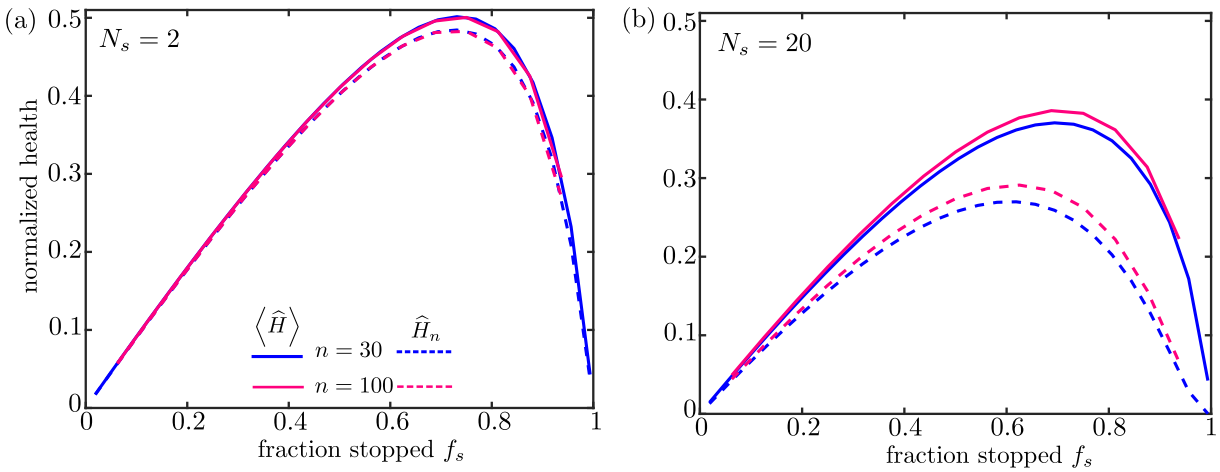

Figure 3.4. Mitochondrial health as a function of key dimensionless parameters.
Solid curves show normalized average health over all demand sites; dashed curves show normalized health at the most distal site. The number of demand sites is set to $n = 30$ (blue) or $n = 100$ (magenta). For each fraction of stationary mitochondria the fusion probability is adjusted to give a fixed number of stopping events for an individual protein traversing the domain: (a) $N_s = 2$ and (b) $N_s = 20$. All values shown are for the SS model, with $M = 1600$ and $\widehat{k}_d = 0.06$. Results for different values of M are provided in Supporting Information S5 Fig.

average speed of motile mitochondria ($\sim 0.5\mu$m/s [218]), and the length of the axon itself. Axon lengths can vary widely, from hundreds of microns up to the meter-long axons in the human sciatic nerve [135]. Because mitochondrial maintenance is particularly challenging when mitochondria must be stationed far away from the cell nucleus, we focus here on long axons in the range of $1-10$ cm. This range corresponds approximately to the average axon lengths measured in callossal neurons in monkey and human brains [26]. Estimating $k_d \approx (4\text{days})^{-1}$ and $v \approx 0.5\mu$m/s, this gives dimensionless decay rates of $\widehat{k}_d \approx 0.06 - 0.6$.

In Supporting Information, we include an expansion of the SS model to a branched tree geometry, rather than linear. Comparing steady-state mitochondrial health for matched values of $\widehat{k}_d$, f_s, and N_s, gives relatively similar results for the branched and linear geometries (S2 Fig), despite the exponentially greater volume, and hence much lower overall mitochondrial density, in the branched structure. This result further highlights the importance of the three main parameters identified here in determining mitochondrial health.

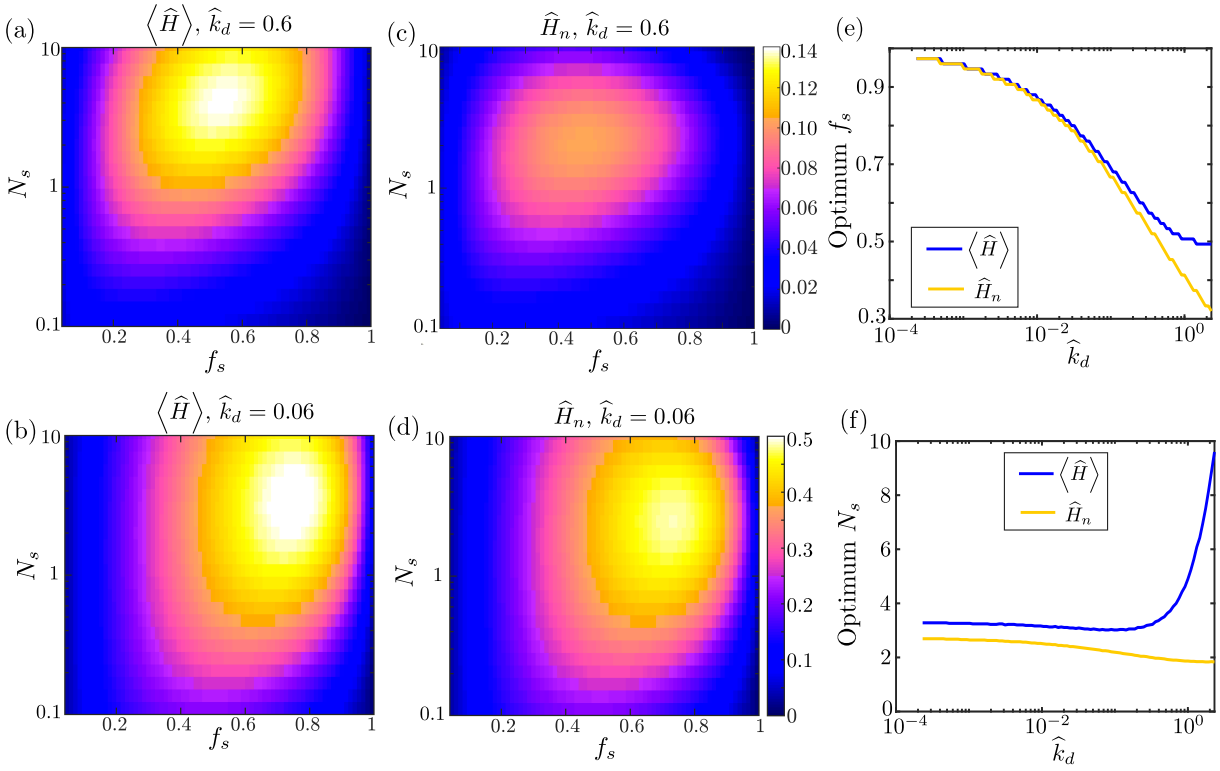

Figure 3.5. Optimizing mitochondrial health through variation of transport parameters. (a-b) Average health across all demand regions as a function of fraction of stopped mitochondria (f_s) and number of stopping events (N_s), for two dimensionless decay rates ($\widehat{k}_d$). (c-d) Mitochondrial health at the most distal demand site, for two different decay rates. (e-f) Values of the f_s and N_s parameters that correspond to maximum average health (blue curves) or last region health (yellow curves). Optimal parameters are plotted as a function of the decay rate. Results shown were computed for the CoG model.

3.4 Results

3.4.1 Optimizing mitochondrial maintenance

We consider the average health of the system as a function of the mitochondrial transport parameters f_s and N_s (Fig. 3.5). An optimal value of the average health is observed at intermediate values of both the stopped fraction and the number of stopping events. When too few mitochondria are in the stationary state (low f_s), then the total health at the demand regions is low simply because there are very few mitochondria present in those narrow regions. On the other hand, if too many mitochondria are stationary (high f_s), the pool of motile mitochondria

available for replenishing decayed proteins at the demand sites becomes very sparse and the health of the system diminishes. The optimum with respect to f_s relies on the assumption that the total mitochondrial content in the domain is limited, embodying a trade-off between the stationary and motile populations.

Higher decay rates $\widehat{k}_d$ require a higher fraction of mitochondria to be motile in order to maintain optimal health. It should be noted that experimental quantification of neuronal mitochondria indicates that roughly $60-90\%$ of mitochondria are in a stationary state [181], in keeping with the optimal values observed for cm-long axons (Fig. 3.5b,d).

For a fixed fraction of stopped mitochondria, low values of N_s (the number of stops made by a protein during its journey along the axon) correspond to a system with very rare interchange between the stationary and motile populations. Values that are too low result in little opportunity for healthy proteins newly synthesized in the soma to be delivered to the demand sites. By contrast, high values of N_s represent a system with very frequent interchange between the two populations. Overly frequent stopping events increase the probability that a protein in a healthy proximal demand site will be picked up by a retrograde motile mitochondrion and carried back into the soma for recycling. In Supporting Information S3 Fig, we show that forbidding retrograde fusion events in the Space Station model removes this optimum and allows higher health levels at high values of N_s.

Similar behavior with respect to f_s and N_s is seen for the normalized health of the last region (Fig. 3.5c-d). The optimum stopped mitochondria fraction and number of stopping events are both shifted to slightly lower values in this case, making it more likely that a protein can successfully reach the most distal region without protracted stops along the way.

Figure 3.5e shows the optimal value for the stationary fraction f_s over a range of dimensionless decay rates $\widehat{k}_d$. The optimum fraction of mitochondria in the stationary pool is high for very long-lived proteins. In the limit of no decay ($\widehat{k}_d \to 0$), all mitochondria can be kept permanently at the demand sites to maximize the health of the system. In the opposite limit of rapidly decaying proteins, the optimum stationary fraction for the average health approaches

$f_s \approx 50\%$, indicating that mitochondria should be split evenly between motile and stationary pools. For the health of the most distal region, the optimal stationary fraction is slightly lower to allow for more motile mitochondria capable of reaching the end of the domain without extensive decay of their protein content.

In Figure 3.5f, we see that when the decay rate is relatively low ($\widehat{k}_d \leq 1$), with many proteins surviving a back and forth journey down the axon, optimum mitochondrial maintenance is achieved in the range $N_s = 2-4$ stopping events. This optimal N_s value is not sensitive to specific values of the decay rate, number of demand sites, or total mitochondrial content. It relies only on the assumption of relatively slow protein decay, and the premise that protein exchange is blind to the current health or position of the mitochondria. We note that physiologically relevant values of the dimensionless protein decay rate are expected to fall in the regime $\widehat{k}_d \leq 1$. A similar range for the optimal number of stopping events N_s is obtained when considering the health of the most distal demand region only.

Interestingly, the optimum values of f_s and N_s remain largely unchanged in a model with branched tree-like geometries (see Supporting Information and S2 Fig). Our model thus robustly predicts that the transition of mitochondrial components from motile to stationary organelles at demand sites is expected to be rare (with only $2-4$ stopping events during the entire journey along the axon), regardless of the specific model, the parameters chosen, or the relative contribution of different sites to the health of the system.

3.4.2 Effect of Local Translation

While distal protein synthesis plays a role in maintaining and modulating local protein levels in neuronal projections [54], it is unclear to what extent the proteins determining mitochondrial health rely on this mechanism. Approximately 30% of neuronal mRNA transcripts have been identified outside the cell body [25]. For some transcripts that do exhibit local translation, severed axons have been observed to have only 5% total protein synthesis capacity relative to the soma [104]. Although we focus on the long-range delivery of protein components to maintain

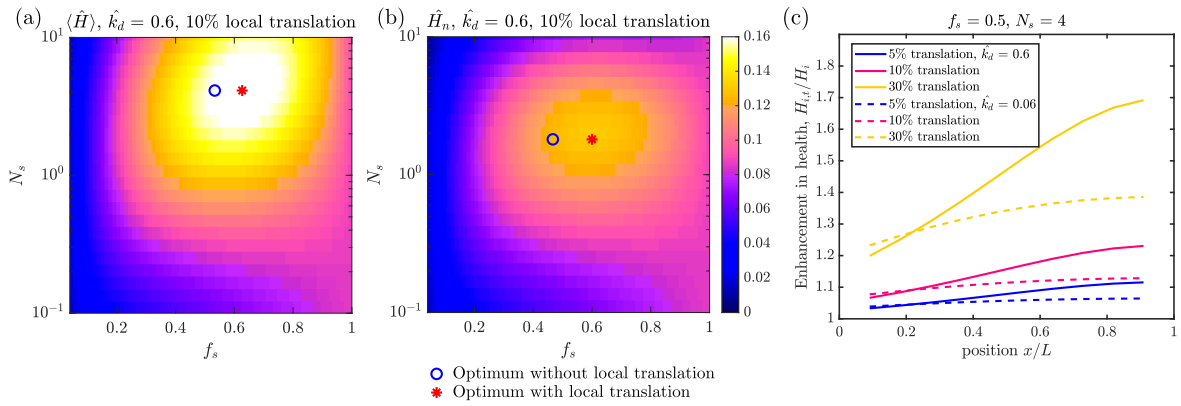

Figure 3.6. Mitochondrial health in the presence of local translation.
(a) Average health across all demand regions as a function of fraction of stopped mitochondria (f_s) and number of stopping events (N_s), for high decay rate ($\widehat{k_d}$) and local translation level $\alpha = 10\%$. Markers show the optimal parameter values with (red asterisk) and without (blue circle) local translation. (b) Corresponding mitochondrial health at the most distal demand site. (c) Enhancement of health levels at each demand site in the presence ($H_{i,t}$) versus absence (H_i) of local translation, for one set of transport parameters, ($f_s = 0.5, N_s = 0.4$), two decay rates $\widehat{k_d}$, and three different local translation levels (α).

mitochondrial health, in this section we explore the effect of low levels ($5-30\%$) of local protein synthesis that may contribute to mitostasis in neurons.

In our simple model for mitochondrial maintenance, we incorporate a term corresponding to local translation and insertion of proteins specifically into the stationary mitochondria. The total rate of protein incorporation at a demand site is assumed to be proportional to the number of stationary mitochondria at that site, replacing Eq. 3.2b with

$$\frac{dH_i}{dt} = vp_s\left[H^+(x_i^-) + H^-(x_i^+)\right] - (k_d + k_w)H_i + \frac{rf_sM}{n}, \tag{3.7}$$

where the stationary mitochondria at steady state are expressed in terms of f_s via Eq. 3.4.

The total flux of proteins delivered into the axon from the soma varies with the fraction of mitochondria in the motile population. For a given total number of mitochondria M, the maximum soma-derived flux is given by $k_{\text{p,max}} = Mv/(2L)$. We assume the rate, per mitochondrion, of distal protein manufacture throughout the axon to be equation to a fraction α of this somal production,

setting $r = \alpha k_{\mathrm{p,max}}/M$. The rate at which new proteins are incorporated into mitochondria stationed at each demand site is then given by rS.

Figure 3.6(a,b) shows the effect of a modest level of local translation with $\alpha = 10\%$, for high degradation rate $\hat{k}_d = 0.6$. The primary difference compared to the model without local translation (Fig. 3.5) is the increased health at high values of f_s (large fraction of stopped mitochondria) and at low values of N_s (less frequent exchange between the motile and stationary populations). The optimum value for the fraction of stopped mitochondria is only slightly increased, to $f_s \approx 0.6$. Notably, the optimum number of stopping events ($N_s \approx 2-4$) remains robust to the introduction of low levels of local translation, indicating that infrequent exchanges between stationary and motile populations remain optimal for mitochondrial maintenance.

In Figure 3.6(c), we plot the enhancement due to local translation at each of the demand sites ($H_{i,\mathrm{t}}/H_i$), for a fixed set of transport parameters close to the optimum value. Unsurprisingly, the effect of local translation is greatest when the dimensionless decay rate is highest, allowing fewer proteins to survive transport to the distal tip of the domain. The biggest effect of local translation is observed on mitochondrial health at the most distal sites. Local translation rates that reach 30% of maximum somal production (per mitochondrion) are sufficient to double the mitochondrial health in the last demand site for high $\widehat{k}_d$ (corresponding to a protein decay time of 4 days and a centimeter-long axon). At these high local translation levels, the optimum in the f_s parameter disappears (S9 Fig), as it becomes advantageous to keep all mitochondria stationed at the demand sites and forgo transport from the soma entirely. However, modest levels of distal translation, similar to those measured for some transcripts in axon severing experiments[104], have a more limited effect on overall health and do little to shift the optimal transport parameters. In order to focus primarily on the interplay between transport and mitostasis, we therefore exclude local translation from our model in all subsequent results.

3.4.3 Variability of mitochondrial health

Our calculations thus far quantify the mean-field steady-state levels of mitochondrial health in high-demand axonal regions. However, the instantaneous health at each site is inherently variable due to the stochasticity of mitochondrial dynamics. This variability arises from fluctuations in both the number of mitochondria and the health per mitochondrion in each region. A robust cellular distribution system may require high levels of mitochondrial health to be maintained over long time periods, rather than tolerating highly fluctuating health levels. At the same time, variability in the distribution of mitochondria may allow for a more rapid response to changing energy demand at the expense of decreased precision in mitochondrial positioning [223]. In neuronal dendrites, mitochondrial content in localized regions has been shown to fluctuate around a well-defined steady-state level [166], indicating that robust maintenance of healthy mitochondria in those regions (low fluctuations compared to average quantities) may be advantageous to the cell.

To understand the effect of stochasticity in our model, we turn to agent-based simulations. These simulations give the same average steady-state mitochondrial health as the mean-field calculations discussed previously (Fig. 3.2). We define the total health variability of our system (σ_H) as the standard deviation in mitochondrial health per region $\langle H \rangle$, calculated over many iterations of the system after it has reached steady state. Although they exhibit the same average health levels for comparable parameter values, the normalized variability [$\sigma_H / \overline{\langle H \rangle}$] is very different for the two maintenance models (Fig. 3.7). Specifically, the CoG model has an additional source of variance due to fluctuating numbers of mitochondria per region, whereas the space-station model has a fixed number of mitochondria at each demand site. In the CoG model, replenishment of protein content occurs in whole-mitochondrion chunks, with transient periods of missing mitochondria in the region until a new one arrives to take its place. This discreteness in protein turnover becomes more pronounced when there are fewer mitochondria per region, as seen in Fig. 3.7. For the SS model, variability arises from how often motile mitochondria

exchange their protein contents with stationary ones, and becomes particularly high when the number of motile mitochondria is small (high f_s). Because the protein levels are a continuous quantity, the SS model allows for more extensive equilibration across the many mitochondria in the system, and thus exhibits lower fluctuations than the CoG model. This difference between the models becomes even more pronounced at lower decay rates (S6 Fig), when most mitochondria in the SS system have similarly high protein levels but the fluctuations in mitochondria number for the CoG model are still present. It should be noted that while the SS model in our simulations fills up demand sites with stationary mitochondria uniformly (same S for all sites), we have also considered an alternate approach where the permanently stationed mitochondria are initially distributed onto demand sites at random. This random initial distribution does not significantly affect the variability in mitochondrial health at the demand sites (S6b Fig).

Overall, the SS model maintains more stable health levels in individual demand sites by allowing for equilibration in protein content rather than removal of discrete mitochondria. This maintenance system is thus expected to be more robust during periods of consistent metabolic demand in specific regions. By contrast, the CoG maintenance mechanism gives rise to higher variability that could allow for more rapid redistribution of healthy mitochondria in systems with time-varying demand site positions.

The difference in variability between the two models is a metric which could serve to distinguish the contribution of each to mitostasis in neurons. Experimental data in embryonic fibroblasts indicates that knock-down of the genes responsible for mitochondrial fusion increases heterogeneity in the mitochondria protein age[52]. Similar experiments in neurons would help establish the role of occasional fusion events in maintaining mitochondrial health.

3.4.4 Effect of Mitophagy

In addition to utilizing motor-driven transport and transient fusion events to maintain a healthy mitochondrial population, neuronal cells make use of mitophagy – a quality control pathway for selectively recycling damaged or depleted mitochondria. Mitochondria with low

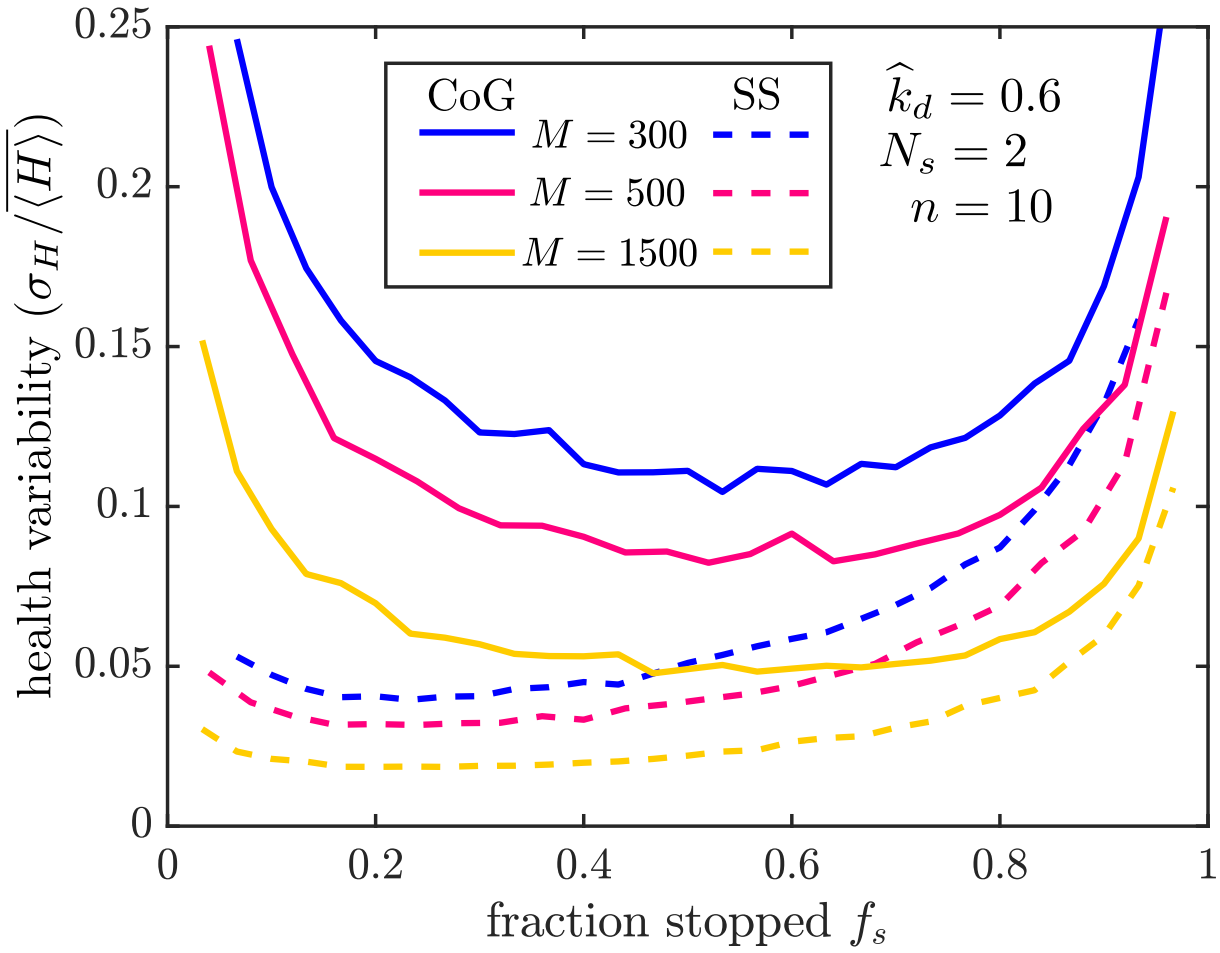

Figure 3.7. Variability of mitochondrial health in different maintenance models.
Plotted is the standard deviation in health per region (σ_H) divided by its average value ($\overline{\langle H\rangle}$), across 1000 iterations of stochastic simulations. Results are shown for 300 (blue), 500 (magenta), and 1500 (yellow) average mitochondria in the domain. Solid lines correspond to simulations of the CoG model and dashed lines to the SS model. All simulations used parameters $\widehat{k}_d = 0.6, n = 10, N_s = 2$. Corresponding plots are provided in Supporting Information to show the effect of lower decay rates (S6a Fig) and of random stationary mitochondria distribution in the SS model (S6b Fig).

membrane potential are recognized by the PINK1/Parkin signaling pathway, which triggers ubiquitination and arrest of mitochondrial transport [181, 217, 214]. The marked mitochondria are then targeted for encapsulation by autophagosomes, which transport them back to the soma for recycling while fusing with proximally located fully acidified lysosomes en route [120, 7]. In essence, this pathway allows for the selective removal of damaged mitochondria from the population and directed transport back to the cell body for rapid recycling of the mitochondrial building blocks.

We introduce mitophagy into our model by allowing mitochondria to enter an "engulfed" state whenever their health drops below a threshold level (ϕ). This simplified approach neglects any delays in autophagosome arrival or recognition of the damaged mitochondria, assuming that all engulfment events occur immediately when the threshold is reached. Although a variety of other quality control mechanisms, such as asymmetric fission [205] and health-dependent halting of mitochondrial transport [237], may contribute to mitochondrial homeostasis, we focus here on a single simplified sensing process representing mitophagy.

While in the engulfed state, the mitochondria move exclusively in the retrograde direction [24, 133], without pauses or reversals, and are unable to stop or engage in fusion at the demand sites. For the Space Station model, if a permanently stationary mitochondrion becomes engulfed and departs for the soma, it leaves behind a gap at the demand site that is filled by stopping the next motile mitochondrion passing that site. A more complex response involving a stopping probability upon passing each open site would correspond to an interpolation between the SS and the CoG models. Because mitophagy is triggered by low health in an individual discrete mitochondrion, our mitophagy model cannot be easily described by mean-field analytical calculations. Instead, we employ stochastic simulations to explore the effect of mitophagy on steady-state mitochondrial maintenance. Simulations are carried out for a domain with $M = 300$ mitochondria, $n = 10$ regions, and $f_s \approx 0.53$, giving a average of 15 mitochondria per site. This number is within the range that has been observed in paranodal regions [135].

Limiting mitochondrial production rates

In its simplest form, the mitophagy model increases mitochondrial turnover without changing any other parameters. By providing an additional pathway for mitochondria to return to the soma, without altering the production rate k_p, mitophagy will decrease the total number of mitochondria in the domain (Fig. 3.8a). This model represents the limiting case where the number of mitochondria in an axon is limited by the rate at which they can be produced from the somal population and injected into the proximal axon, regardless of how much total mitochondrial material is available. We consider the effect of mitophagy on the overall health of axonal mitochondria in this regime, comparing both the SS and CoG model. We start with the case of no mitophagy ($\phi = 0$), considering a vertical slice of the plots in Fig. 3.5 corresponding to a fraction of mitochondria in the stationary state: $f_s(\phi = 0) = 0.53$. We proceed to increase the protein threshold ϕ, corresponding to more frequent mitophagy events, while holding constant all other parameters (including production rate k_p, number of stops N_s, restarting rate k_w in the CoG model, and maximum number of mitochondria that can be stationed at each site, S, for the SS model). The effect of increasing mitophagy on mitochondrial health can be considered by defining the health in each demand site, normalized by the total mitochondrial content per site in the absence of mitophagy ($M^{(0)}$). Specifically, we define the health of the i^{th} demand site as

$$\widehat{H}_i^{(0)} = H_i / [M^{(0)}/n], \tag{3.8}$$

and the average health across all sites as $\left\langle \widehat{H}^{(0)} \right\rangle$. Unlike our previous normalization (Eq. 3.1), this quantity no longer corresponds to the health per mitochondrion, because the advent of mitophagy would decrease the total number of mitochondria in the domain. Instead, we use this health metric to understand how the total amount of mitochondrial protein changes at each demand site when new mitochondrial production is not upregulated to keep up with the enhanced turnover due to mitophagy. The alternate case, where total mitochondrial content is kept constant,

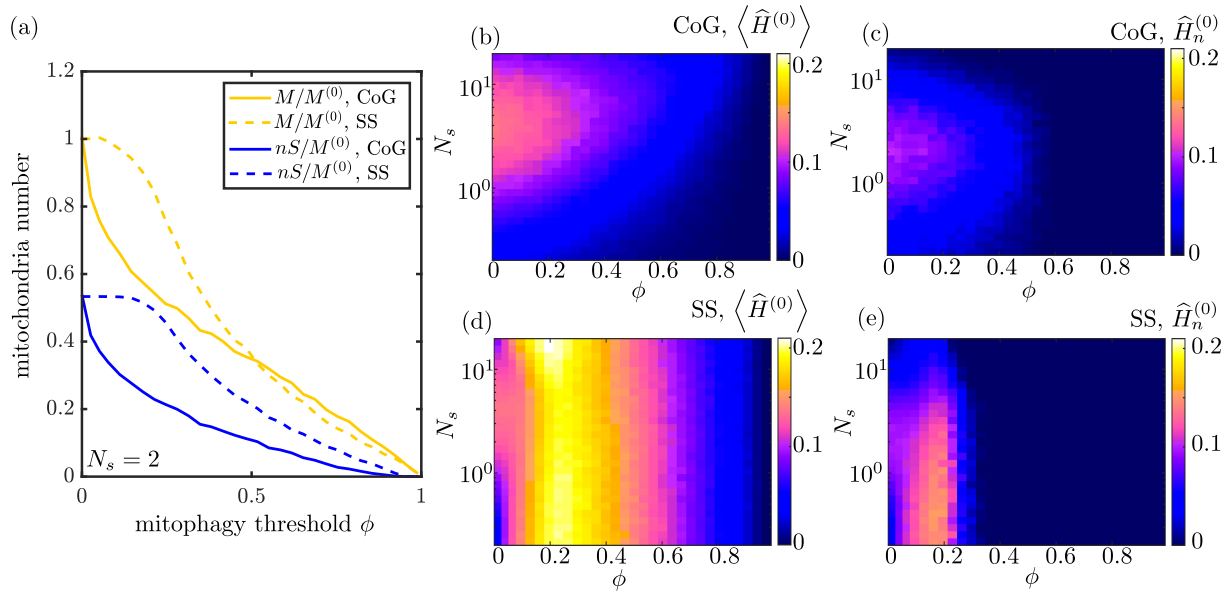

Figure 3.8. Effect of mitophagy, at fixed production rate k_p.
(a) The total number of mitochondria in the domain (yellow) and the number of stationary mitochondria (blue) are plotted as a function of the mitophagy threshold, for both the CoG model (solid lines) and the SS model (dashed lines). Mitochondria quantities are normalized by the steady-state number of mitochondria in the absence of mitophagy. (b) Mitochondrial health for the CoG model, averaged over all demand sites, plotted as a function of mitophagy threshold and number of stopping events N_s. (c) Health at most distal demand site, for the CoG model. (d-e) Analogous plots of average health and distal site health for the SS model. All plots assume mitochondrial production rate does not change with increased mitophagy, and correspond to fraction of mitochondria stopped $f_s(\phi = 0) = 0.53$ in the absence of mitophagy.

is considered in the subsequent section.

A seen in Fig. 3.8b,c, the introduction of mitophagy in the CoG model decreases the mitochondrial health at the demand sites. This is a result of a decrease in the average number of mitochondria stationed at each site (Fig. 3.8a), as mitophagy causes more mitochondria to leave the domain without increasing the production rate k_p. By contrast, in the SS model modest levels of mitophagy will actually increase the average mitochondrial health at the demand sites (Fig. 3.8d). For this maintenance system, the number of stationary mitochondria does not change significantly for $\phi \lesssim 0.2$ (see Fig. 3.8a). However, these low levels of mitophagy remove some of the most unhealthy motile mitochondria from the population capable of fusing, thereby increasing the average health of all the remaining mitochondria in the domain. Notably,

a mitophagy threshold of $\phi \approx 0.2$ optimizes both the average health of stationary mitochondria and the health of the most distal site in the SS model (Fig. 3.8d-e).

The difference between the CoG and SS model in the presence of mitophagy reflects, in part, the different variability of stationary mitochondria. In the SS model, the mitochondria are more homogeneous in terms of their protein content (Fig. 3.7). Because mitophagy removes individual organelles whose health drops below a particular threshold, the homogenization arising from fusion events makes it less likely that a stationary mitochondrion will drop below threshold and become engulfed. As a result, low levels of mitophagy have a much smaller effect on both the number of stationary mitochondria and the total number of mitochondria (engulfed, stationary, and motile) in the SS model. For this model, only those mitochondria moving retrograde and already near the somal region become engulfed at low ϕ values. These depleted mitochondria are prevented from fusing with stationary mitochondria in the proximal demand regions, thereby increasing the overall health of the system without substantial change to total mitochondrial number.

Limiting mitochondrial content

One of the presumed benefits of the mitophagy pathway is its ability to more rapidly return damaged mitochondria to the soma, permitting their components to be recycled for future use [135]. We therefore consider again the regime where the system is limited not directly by the production rate, but by the total amount of available mitochondrial components. In this case, mitophagy causes an increase in the production rate k_p, as the mitochondria on average return to the soma more quickly for recycling. We implement this model by rescaling all protein levels by the total number of mitochondria (including engulfed, stationary, and motile) in the domain. Health levels are normalized by the actual number of total mitochondria at steady state [$\widehat{H}_i = H_i/(M/n)$], thereby removing the effect of decreased mitochondrial population in the presence of autophagy. This approach is equivalent to explicitly fixing the total amount of mitochondrial content available, as demonstrated in Supporting Information (S7 Fig).

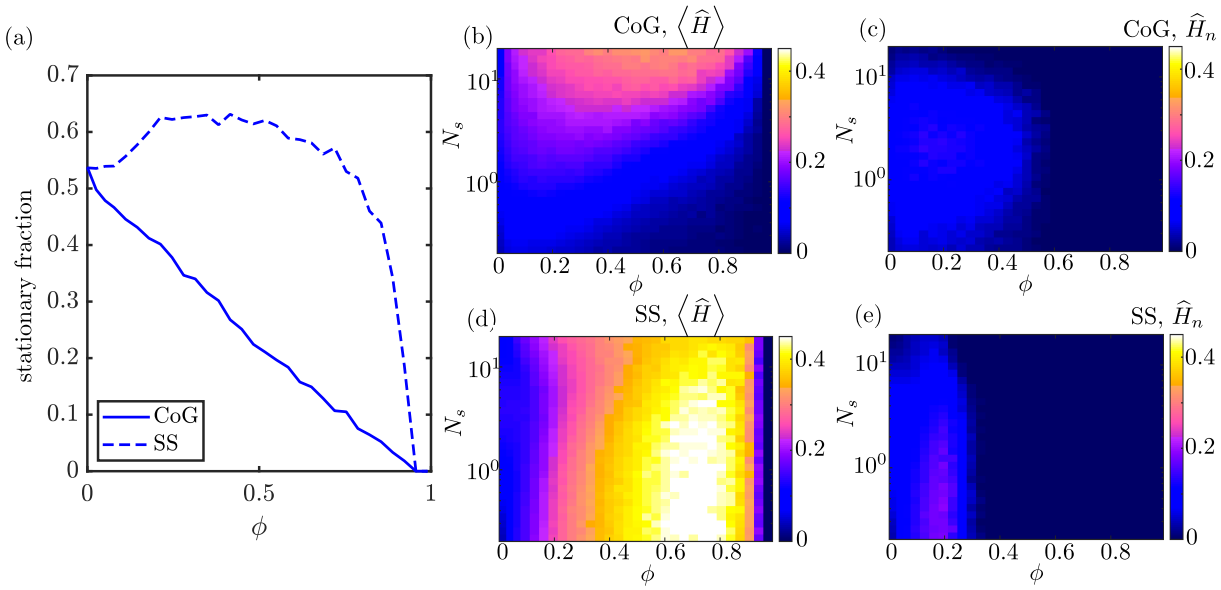

Figure 3.9. Effect of mitophagy when total mitochondrial number is limited.
(a) Fraction of mitochondria in the stationary state as a function of increasing mitophagy threshold, for the CoG model (solid line) and the SS model (dashed line), with parameters set such that $f_s = 0.53$ at $\phi = 0$. (b) Mitochondrial health, normalized by the total number of mitochondria per site, averaged over all demand sites, for the CoG model. (c) Normalized mitochondrial health at most distal demand site, for the CoG model. (d-e) Analogous plots of normalized average health and distal site health for the SS model. Normalizing by total mitochondrial number is equivalent to a system where the total mitochondrial content is held fixed with the onset of mitophagy (S7 Fig).

In this regime, both the SS and CoG maintenance models allow an increase in mitochondrial health with intermediate levels of mitophagy (Fig. 3.9b-e). The normalized health of the most distal region ($\widehat{H}_n$) is increased by about 90% for the SS model and 40% for the CoG model, when compared to the case of zero mitophagy (evaluated at the optimum value of N_s for each ϕ value). As before, the optimal mitophagy threshold is in the range $\phi \approx 0.1 - 0.2$ for both models. The average health of stationary mitochondria improves by 80% for the SS model and 20% for the CoG model at these optimal mitophagy thresholds. While higher mitophagy levels can improve average regional health still further, they do so at the expense of a severe drop in the health of the most distal region, as very few mitochondria are able to reach that region when mitophagy occurs too early in the domain.

Even when normalizing by total mitochondrial content, the SS model has a significant advantage over the CoG model. Namely, because the restarting rate k_w is fixed for each row in the plots of Fig. 3.9, the fraction of mitochondria in the stationary state drops substantially in the CoG model as mitophagy is introduced (Fig. 3.9a). This reflects the fact that stationary mitochondria are preferentially engulfed in this model, so that even if we normalize by the total mitochondrial content, a smaller fraction of mitochondria remain at the demand sites. In the SS model, by contrast, equalization of mitochondrial health by transient fusion events implies that stationary mitochondria are no more likely than motile ones to become engulfed, and the fraction of mitochondria in the stationary state remains constant or even increases slightly for a broad range of ϕ values.

It is reasonable to suppose that a cell employing the CoG strategy might have compensatory mechanisms to adjust the fraction of the mitochondrial pool that is stationed at demand sites in the presence of mitophagy (perhaps by increasing stopping probability p_s or decreasing the restarting rate k_w). In order to assess the relative advantage of the two models, we therefore consider the maximal mitochondrial health each of them can achieve at a given mitophagy level, if allowed to freely adjust the other model parameters. We assume the total mitochondrial pool remains fixed and therefore again normalize the results by M/n as in Fig. 3.9.

As the mitophagy threshold is raised (with freely adjustable transport parameters), the increase in average health over all the demand regions can be substantial — up to 4-fold for the CoG model and 5-fold for the SS model (Fig. 3.10a). However, the parameters that give such high average health result in most of the protein content being concentrated in the first few demand sites, with the health of the most distal site dropping to zero. This regime corresponds to rapid turnover of motile mitochondria that undergo mitophagy before they ever reach the distal regions. Notably, experimental observations have indicated that mitochondrial densities are indeed somewhat lower at distal sites [122, 142]. Given the necessity of supplying the metabolic needs of all individual demand sites, we next consider the parameters necessary to maximize mitochondrial health in the most distal site, rather than averaging over the entire domain.

If we optimize over the health of the most distal site (Fig. 3.10b), we see as before that this distal health increases by about 90% in the SS model and about 40% in the CoG model, compared to the case of no mitophagy. These values represent the maximal distal site health that can be achieved by each model if the parameters f_s and N_s are allowed to vary freely, within the constraint of constant $\phi, \widehat{k}_d, M, n$. At the optimal mitophagy threshold ($\phi \approx 0.2$), the average regional health is also increased, in both models, by up to a factor of two. However, the CoG model allows for greater average health at still-higher mitophagy levels, indicative of its tendency to distribute mitochondria unevenly throughout the domain when mitophagy is present, so that proximal sites gain many healthy mitochondria while distal health are left under-supplied.

We conclude that introducing mitophagy to selectively recycle unhealthy mitochondria can substantially improve mitochondrial health throughout high-demand regions of the domain. This improvement is maximized by allowing mitochondria to become engulfed when their health level drops below approximately 20% of its initial value. It should be noted that this optimal value of ϕ is specific to the decay rate ($\widehat{k}_d \approx 0.6$) used in these simulations. This dimensionless decay rate corresponds to a domain length of about 10 cm and protein lifetime of about 4 days, so that there is a substantial amount of protein decay by the time a mitochondrion traverses the entire domain. Lower values of $\widehat{k}_d$ move the optimal ϕ to higher values, rising to an optimum value of

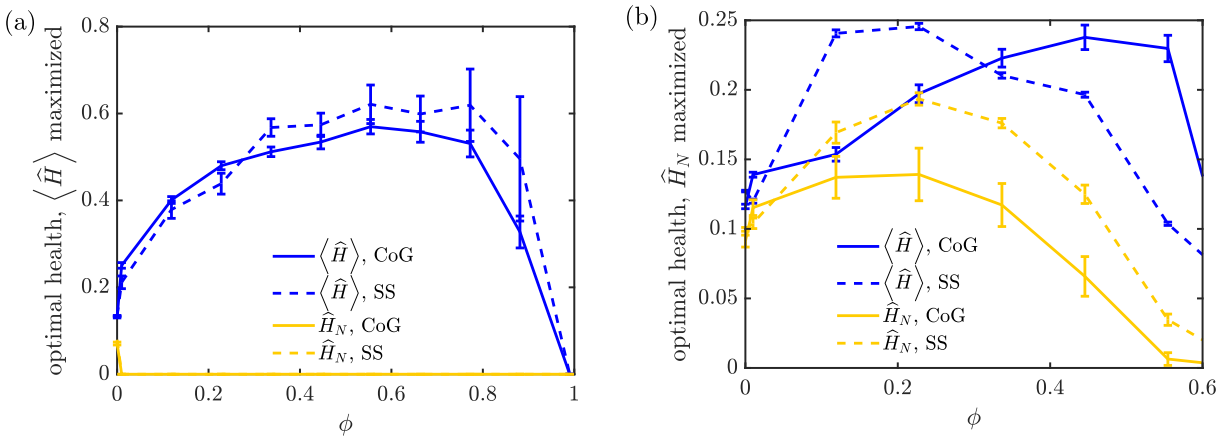

Figure 3.10. Optimal performance of mitochondrial maintenance models in presence of mitophagy.
(a) For each mitophagy threshold ϕ, the parameters f_s, N_s are optimized to give the maximum normalized average health: $\langle H \rangle$. The resulting normalized average health (blue) and normalized last region health (yellow) are plotted for the CoG model (solid) and SS model (dashed). (b) Analogous plots, with parameters adjusted to maximize the normalized last region health $\widehat{H}_n$ for each mitophagy threshold. All health levels are normalized by total mitochondrial content per region (M/n), corresponding to a system where the total amount of mitochondrial material is limited. Error bars show standard error of the mean from 10 replicates. Fixed parameters are $\widehat{k}_d = 0.6, M = 300, n = 10$. A corresponding plot of optimized health for low decay rate $\widehat{k}_d$ is provided in Supporting Information S8 Fig.

$\phi = 0.6$ for $\widehat{k}_d = 0.06$, corresponding to a shorter 1 cm axon (S8 Fig). This shift reflects the fact that less degradation occurs during the journey of a mitochondrion along the axon, making it feasible to trigger mitophagy at higher health thresholds while still allowing mitochondria to reach the last demand site. An interesting consequence of this model is that longer neuronal projections require mitophagy to be delayed to more extensive decay levels in order to permit at least partially functional mitochondria to reach the most distant demand sites.

3.5 Discussion

The models described above constitute a quantitative framework for mitochondrial maintenance in extended cellular regions such as neuronal axons. Neurons face unique challenges in mitochondrial homeostasis, both because of the need to transport material from the cell body through long cellular projections and because of their spatially heterogeneous metabolic

needs. Balancing these constraints requires positioning stationary mitochondria in specific regions of high metabolic demand, while also retaining a population of motile mitochondria to transport the components needed for mitochondrial health. Our work differs from prior studies of mitochondrial maintenance [138, 150] by taking into account these spatial constraints unique to neurons. At the same time, we diverge from prior models of transport and spatial distribution for neuronal components [223] by incorporating continuous degradation and focusing on the steady-state health at specific localized sites.

Our results highlight similarities and differences between two main models of mitostasis: the 'Changing of the Guard' and the 'Space Shuttle' model. In the absence of selective recycling processes, the two models are shown to be equivalent in their average steady-state behavior. Analysis of the mean-field model for both mechanisms shows that in extended projections, with many demand sites and large numbers of mitochondria, the efficiency of the maintenance mechanism depends primarily on three dimensionless parameters. These parameters are (1) $\widehat{k}_d = k_d L/v$, which sets the extent of health decay while a mitochondrion crosses the domain, (2) $f_s = nS/M$, the fraction of mitochondria in the stationary pool, and (3) $N_s = 2\widehat{p}_s n$, the typical number of stopping events for a mitochondrial component during its round-trip journey through the projection. Optimal mitochondrial health in high-demand sites is achieved at intermediate values of both f_s and N_s. The optimal fraction of stationary mitochondria lies in the $50-80\%$ range, depending on the precise value of the dimensionless decay rate. This range is compatible with experimental observations which imply that $60-90\%$ of axonal mitochondria are stationary [181]. For mature cortical axons, the observed stationary fraction has been observed to be relatively high at 95% [109], possibly hinting at an even slower effective degradation rate of mitochondrial cargo.

Furthermore, our model makes the prediction that, for a broad physiologically relevant range of decay rates, very few stopping events ($N_s \approx 2-4$) are required for optimal maintenance. This result is robust to the introduction of low levels of local translation (Fig 3.6) or expansion of the model to a branched tree-like morphology (S1 Fig). The low optimal value of N_s implies

that both switching of mitochondria between motile and stationary states and transient fusion events of axonal mitochondria should be very rare – happening only a few times during the entire journey of a mitochondrion down the axon. Due to the inherent difficulty of experimentally tracking motile mitochondria over long time periods, this result is consistent with the fact that stationary mitochondria appear to be nearly permanent and interchange between stationary and motile pools is rarely observed [50, 194, 218].

Differences between the CoG and the SS models become evident when considering the variability of mitochondrial health at demand sites over time and between different cells. Transient fusion and fission events in the SS model allow extensive equilibration of health levels between individual mitochondria, resulting in much lower variance in the health of entire regions. On the one hand, such decreased variance implies a more robust maintenance system, which avoids large fluctuations in metabolic health at a high-demand site as individual mitochondria enter or leave the stationary pool at that site. On the other hand, greater fluctuations in the CoG model may imply an enhanced responsiveness to changing conditions (*eg:* changing spatial distribution of metabolic demand). A close relationship between fluctuation magnitudes and response to external driving is a key feature of physical systems dominated by thermal fluctuations [99]. Analogous fluctuation-response relationships have also been proposed to underly biological systems [106, 177], such as gene networks, where a greater degree of responsiveness to external signals goes hand in hand with higher fluctuations at steady-state [225, 21]. Although detailed exploration of temporal response by mitochondrial maintenance systems lies outside the scope of this paper, the behavior of these models in the presence of time-varying metabolic demand serves as a potentially fruitful area for future work.

A biologically relevant consequence of the different fluctuation magnitudes for the two maintenance models is their differing response to the incorporation of selective mitophagy of damaged mitochondria. In a system where mitochondrial production remains constant, introducing low levels of autophagy causes a substantial drop in the number of stationary mitochondria at each demand site in the CoG model. For the SS model, by contrast, equilibration

of mitochondrial health implies that the number of both stationary and total mitochondria remains relatively unchanged at low mitophagy thresholds. As a result, moderate autophagy levels improve the overall mitochondrial health at demand sites in the SS model while monotonically decreasing health in the CoG case.

Because mitophagy allows mitochondria to be recycled more rapidly, we also consider the steady-state health normalized by total number of mitochondria in the domain. This approach is equivalent to adjusting the mitochondrial production rate in such a way that the total number of mitochondria remains fixed even in the presence of autophagy. In this case, an optimal autophagy threshold is observed for both models, although the SS model still allows for the greatest (nearly 2-fold) increase in the mitochondrial health at the most distal demand site. Overall, the extensive mixing of mitochondrial contents permitted by transient fusion and fission events allows for improved health of localized mitochondria in the presence of recycling via selective mitophagy. The optimal mitophagy threshold depends on the domain length and protein decay rate, with an optimal value of $\phi \approx 0.2$ for both models in the case of 10 cm axons and 4-day mitochondrial protein decay times.

The models described in this work are, of necessity, highly simplified. The model design aimed to highlight key challenges of mitochondrial maintenance in long neuronal projections and some of the fundamental strategies that can be utilized by the cell to meet those challenges. In reality, neuronal mitostasis may include a variety of complicating factors, many of which remain poorly understood. For example, our model incorporates the simplest possible sensing and response mechanism for mitochondrial health — dropping below a critical health level prevents further exchange events and forces a return to the soma for recycling. Other contributing mechanisms may include asymmetric fission that concentrates health factors in one of the resulting organelles [205, 150], local recycling [7] and formation of new mitochondria, or a sensing mechanism that regulates the ability of mitochondria to stop as a function of total ATP production by other mitochondria in the region [230, 216]. Furthermore, a sensing mechanism that would prohibit fusion of retrograde mitochondria while allowing frequent fusion

of anterograde ones would also increase overall health levels in the domain, though having little effect on the health of the most distal site (S3 Fig). Although such mechanisms would allow for more efficient mitochondrial maintenance, we focus here on the simplified case of purely somal mitochondria production and no additional sensing that would differentiate the behavior of stationary or motile organelles. Additionally, we employ the simplifying assumption of a constant decay rate k_d for both stationary and motile mitochondria. More complicated models where the decay in mitochondrial health depends on local metabolic activity could be incorporated within the framework of this model in future work.

In addition to the two transport and exchange mechanisms described here, local protein translation may also contribute to mitochondrial maintenance in distal regions [91, 87, 79]. However, the extent to which mitochondria are able to produce their full complement of proteins by local synthesis is largely unknown. General measurements of local translation indicate that only about a third of transcripts are found outside the cell soma, and that for individual transcripts the protein synthesis capacity of the axon may be only a small fraction of somal production [25, 104]. We incorporate a small contribution from local translation in our model, and find that the primary outcomes – the optimal fraction of stopped mitochondria and the small optimal number of stopping events – remain unchanged (Fig. 3.6). More extensive local synthesis could drive the system to place all mitochondria in the stationary population (S9 Fig). However, it should be noted that even a small set of mitochondrial proteins that rely on somal translation would necessitate the transport and exchange mechanisms described here. To focus on the interplay between transport and maintenance, we primarily explore system dynamics in the absence of local translation. Our assumption that key components of mitochondrial health require long-range transport from the soma is partly substantiated by evidence that mitochondrial aging increases with distance from the soma [52], implying an important role for long-range transport.

For the most part, we consider the simplest possible system geometry, with a single linear projection rather than more complicated branched axonal structures. We find that our results with

this simplification can also be applied to symmetric branched geometries, further underscoring the importance of the effective transport and exchange parameters defined here. Our models also assume the metabolic demand in a neuron is concentrated at discrete high-demand regions. While this is an over-simplification of the complex distribution of neuronal metabolism, it serves as a limiting case for spatial heterogeneity that requires the formation of both stationary and motile pools of mitochondria.

Studies in non-neural globular animal cells show that mitochondrial maintenance relies largely on fusion and fission to maintain the health of the overall population of mitochondria [222]. In neuronal axons, fusion events are thought to be relatively rare, and it seems likely that mitostasis actually involves a hybrid of the 'Changing-of-the-Guard' and the 'Space-Shuttle' mechanisms. Our separate exploration of the two models highlights the similarity of both in maintaining the average mitochondrial health. However, we have also shown that the differing fluctuations dictated by the two models can alter their response to rising levels of mitophagy, implying that the introduction of occasional localized fission and fusion events can prove beneficial. Experimental studies that explore the effect of knocking down fusion proteins on the overall age of mitochondrial proteins, such as have already been carried out for non-neuronal cell types[52], would help disentangle the contribution of the SS and CoG mechanisms to mitostasis in neurons.

The interplay of transport and localization is a general principle for maintaining homeostasis under the constraints of highly extended geometries and spatially heterogeneous demands that characterize neuronal cells. Our analysis outlines the key parameters that can be tuned to optimize steady-state distributions, with a specific focus on maintaining mitochondrial health in neurons. A key consequence of the models is that optimal mitochondrial health can be maintained with a large fraction of stationary mitochondria and with very rare interchange between the stationary and motile population. This prediction may account for the difficulty of catching such exchanges in live cell imaging experiments, and the general tendency of stationary mitochondria to remain stationary over long periods of observation [50, 109, 194]. With the

advent of new experimental techniques that allow for long-term tracking of individual mitochondria [218], it would be valuable to quantify the frequency of these rare transitions. Our results also predict a benefit to mitochondrial exchange via transient fusion events, motivating future experimental determination of whether such fusions contribute to maintenance of localized axonal mitochondria. Given the importance of mitochondrial maintenance for neuronal health, developing a quantitative framework that delineates the factors governing mitostasis serves as a critical step towards better understanding of the role of metabolism in neurodegenerative diseases.

3.6 Methods

Source code for all simulations and analytic calculations is available at: https://github.com/lenafabr/mitofusion.

3.6.1 Table of Parameters

3.6.2 Steady-state mean-field solution for CoG model

We find the steady-state solution for the mean-field version of the Changing-of-the-Guard model, which treats mitochondrial density and mitochondrial health as continuous fields on a linear segment from $x = 0$ to $x = L$. We define the density of anterograde and retrograde motile mitochondria as $\rho^{\pm}(x)$, while the number of stationary mitochondria in each point-like high-demand region i is given by S_i. These distributions obey the following set of dynamic

equations:

$$\frac{d\rho^{\pm}}{dt} = \mp v\frac{\partial \rho^{\pm}}{\partial x} \tag{3.9a}$$

$$\frac{dS_i}{dt} = vp_s(\rho^+(x_i^-) + \rho^-(x_i^+)) - k_w S_i \tag{3.9b}$$

$$v\rho^{\pm}(x_i^{\pm}) = v\rho^{\pm}(x_i^{\mp})(1-p_s) + \frac{1}{2}k_w S_i \tag{3.9c}$$

$$\rho^+(L) = \rho^-(L) \tag{3.9d}$$

$$v\rho^+(0) = k_p \tag{3.9e}$$

Equation 3.9a describes the evolution of the mitochondrial density in each interval between consecutive demand sites. Equation 3.9b governs the number of stopped mitochondria at each discrete demand site, with the first term corresponding to the incoming flux of mitochondria stopping at that site, and the second term corresponding to the restarting of stationary mitochondria. The remaining equations provide the boundary conditions for each interval of the domain between demand sites. Equation 3.9c enforces conservation of organelles, so that the flux of anterograde mitochondria leaving the site is equal to the combination of those organelles which pass by without stopping and those which restart from a stopped state. Eq. 3.9d - 3.9e set the boundary conditions at the distal end (anterograde mitochondria turn around to move in the retrograde direction) and the proximal end of the domain (mitochondrial production).

At steady state, Eq. 3.9a implies that the linear density of mitochondria is constant within each region between demand sites. Setting Eq. 3.9b to zero yields the steady-state relation,

$$S_i = \frac{vp_s(\rho^+(x_i^-) + \rho^-(x_i^+))}{k_w}. \tag{3.10}$$

Plugging in to the boundary conditions Eq. 3.9c-3.9e then implies that the motile mitochondrial densities are equal and constant everywhere in the domain: $\rho^+ = \rho^-$. We define $\rho = \rho^+ + \rho^-$ as the constant steady-state density of all motile mitochondria. From the boundary condition at

the proximal end, we can relate this density (as well as the stopped mitochondria at each site) to the rate of mitochondrial production.

$$\rho = 2k_p/v, \quad S = vp_s\rho/k_w$$

The linear density of mitochondrial health (ie: the sum of health levels for all mitochondria that happen to be present at a given position in the domain) can be described by very similar equations, with additional terms for decay at rate k_d. Equation 3.2 describes the evolution of this field over time.

Setting Eq. 3.2b- 3.2c to zero at steady-state yields the relations

$$vH^+(x_i^+) = vH^+(x_i^-)(1-p_s) + \frac{k_w v p_s \left[H^+(x_i^-) + H^-(x_i^+)\right]}{2(k_d + k_w)}. \tag{3.11}$$

Furthermore, Eq. 3.2a implies that the steady-state distribution of motile mitochondrial health exhibits an exponential decay across each interval between consecutive demand sites $i-1$ and i. This gives the set of conditions:

$$H^+\left(x_i^-\right) = e^{-xk_d/v}H^+\left(x_{i-1}^+\right), \quad H^-\left(x_{i-1}^+\right) = e^{xk_d/v}H^-\left(x_i^-\right), \tag{3.12}$$

Together, Eq. 3.11, 3.12, and 3.2c - 3.2e constitute a set of linear equations for the health levels in stationary mitochondria at the demand sites $[H_i]$ and the motile health densities on either edge of the demand sites $[H^{\pm}(x_i^{\pm})]$. This system of equations is then solved using standard matrix methods.

3.6.3 Steady-state mean field solution for SS model

A key feature of the Space Shuttle model is that a fixed number of permanently immobile mitochondria (S) are stationed at each discrete demand site. These mitochondria are assumed to

have a well defined order, but to be positioned arbitrarily close together within the point-like site. We define $H_{i,j}$ (with $1 \leq i \leq n$ and $1 \leq j \leq S$) as the health of the j^{th} stationary mitochondrion at the i^{th} demand site. An anterograde moving mitochondrion encounters each of the stationary ones in order as it passes the demand site. The quantity $H^{+}_{i,j-1}$ describes the linear health density of all anterograde mitochondria just after they pass the $(j-1)^{\text{th}}$ stationary organelle at the i^{th} site, and are approaching the j^{th} stationary organelle. Similarly, retrograde mitochondria encounter the stationary organelles in reverse order and their health density is given by $H^{-}_{i,j+1}$ as they approach the j^{th} stationary organelle from the distal side. Each time a moving mitochondrion passes a stationary one, there is a probability p_f that they will fuse. When such a fusion event occurs, the health levels of the two mitochondria are averaged together and both are left with a health equal to that average. It should be noted that $H^{\pm}$ and $H^{\pm}_{i,j}$ are densities and have units of health level per unit length, while the quantities $H_{i,j}$ have units of health level.

Motile anterograde mitochondria are produced at the proximal end with rate k_p. They then move forward and back throughout the domain, never stopping and instantaneously reversing their direction from anterograde to retrograde once they reach the distal end. The density of motile mitochondria is not affected by the fusion behavior, and evolves according to Equations 3.9a, 3.9d, 3.9e. At steady state, this density must be a constant value $\rho = (M - nS)/L$, equally split between anterograde and retrograde organelles.

The set of mean-field equations describing the mitochondrial health in the SS model is, for $1 \leq j \leq S$,

$$\frac{dH^{\pm}}{dt} = \mp v \frac{\partial H^{\pm}}{\partial x} - k_d H^{\pm} \tag{3.13a}$$

$$\frac{dH_{i,j}}{dt} = \frac{v p_f}{2}\left[H^{+}_{i,j-1} + H^{-}_{i,j+1}\right] - \left[\frac{v\rho p_f}{2} + k_d\right] H_{i,j} \tag{3.13b}$$

$$H^{\pm}_{i,j} = H^{\pm}_{i,j\mp 1}\left(1 - \frac{p_f}{2}\right) + \frac{p_f \rho}{4} H_{i,j} \tag{3.13c}$$

$$H^{+}(L) = H^{-}(L) \tag{3.13d}$$

$$vH^{+}(0) = k_p. \tag{3.13e}$$

Equation 3.13b describes the time evolution of the health of each stationary mitochondrion. The first term corresponds to the flux of incoming mitochondrial health multiplied by the probability of fusion (p_f) and the probability ($1/2$) that a given protein will stay with the stationary mitochondria after the fusion-and-fission cycle is complete. The second term gives the rate at which health markers leave the stationary mitochondrion through being transferred to the motile partner during a fission and fusion cycle, and through decay. The edge values at each site are defined by $H^+_{i,0} = H^+(x_i^-)$, $H^+_{i,S} = H^+(x_i^+)$, $H^-_{i,1} = H^-(x_i^-)$, and $H^-_{i,S+1} = H^-(x_i^+)$, where x_i^- refers to the limit approaching site i from the proximal side and x_i^+ is the limit approaching from the distal side. Equation 3.13c sets the flux of motile health leaving a stationary mitochondrion equal to the flux of health approaching that mitochondrion from the opposite side and going straight through without transfer, plus the flux of health carried out of the stationary mitochondria as a result of fusion events. Overall, Eq. 3.13 provides a closed set of equations that can be solved at steady state.

In the case where there is one stationary mitochondrion at each demand site ($S = 1$), the equations above become equivalent the the dynamic equations for the CoG model (Eq. 3.2), with the restarting rate k_w replaced by an effective rate at which proteins in a stationary mitochondrion leave the organelle via fusion and fission ($\widehat{k}_w = v\rho p_f/2$). The stopping rate p_s is replaced by an effective rate of a protein ending up in a stationary mitochondrion each time there is a passage event ($\widehat{p}_s = p_f/2$). In the case where there are multiple mitochondria per site, the total stationary health at each site is given by $H_i = \sum_{j=1}^{S} H_{i,j}$. Solving together Equations 3.13b- 3.13c then yields

$$\begin{aligned}\frac{dH_i}{dt} &= v\left[1-\left(1-\frac{p_f}{2}\right)^S\right]\left[H^+(x_i^-)+H^-(x_i^+)\right]-\left[\frac{v\rho p_f}{2}+k_d\right]H_{i,j}\\ &\quad+\frac{p_f}{2}\sum_{k=1}^{S}\left[1-\left(1-\frac{p_f}{2}\right)^{S-k}\right]\left(H_{i,k}+H_{i,S-k+1}\right).\end{aligned} \tag{3.14}$$

For small values of p_f, the last term can be neglected, and the SS model becomes equivalent to

the CoG model (Eq. 3.2b), with the effective stopping rate given by $\widehat{p}_s = 1 - \left(1 - p_f/2\right)^S$, and the effective restarting rate given by Eq. 3.5. Intuitively, the effective stopping rate is simply obtained by finding one minus the probability that a protein is not left behind in any of the S independent fusion events, each of which occurs with probability p_f while passing the multiple mitochondria stationed at a site.

3.6.4 Discrete stochastic simulations

Discrete stochastic simulations for both the CoG and the SS model were carried out by tracking the positions and health levels of individual point-like mitochondria on a finite linear interval representing a neuronal axon. All length units were normalized by the domain length and all time units by the mitochondrial velocity, such that $L = 1$ and $v = 1$ in the simulations. High-demand sites where mitochondria could stop (in the CoG model) or fuse (in the SS model) were represented as point sites equispaced in the domain. Simulations were propagated forward for 10^5 time-steps of duration $\Delta t = 10^{-3}$. Each simulation was carried out as 100 independent iterations and the average results are reported.

At each time-step, a new mitochondrion was generated at position 0 with probability $1 - \exp(-k_p \Delta t)$. For the CoG model, each mitochondrion was labeled as being in the anterograde, retrograde, or stationary state. At each time-step, a motile mitochondrion took a step of $\pm v\Delta t$, depending on whether it was in the anterograde or retrogtrade step. An anterograde mitochondrion that reached the domain end (at L) was flipped to a retrograde state. A retrograde mitochondrion that reached 0 was removed from the simulation. A stationary mitochondrion restarted with probability $1 - \exp(-k_w \Delta t)$, with its new directionality equally likely to be set to antegrograde or retrograde. Whenever a motile mitochondrion crossed the demand site, it had probability p_s of switching to a stationary state. Each mitochondrion had a continuous health variable associated with it, set to 1 when the mitochondrion was formed and multiplied by $\exp(-k_d \Delta t)$ during each simulation time-step.

The SS model was simulated in a similar manner. A fixed number of permanently

stationary mitochondria were evenly distributed among the demand sites at the beginning of the simulation. Each time a motile mitochondrion crossed over the demand site, it attempted to fuse with each stationary mitochondrion at that site, in sequence, with probability p_f. Whenever a fusion successfully occurred, the health levels of both fusing mitochondria were set to the average of their two health levels. The motile mitochondrion would then proceed to attempt the next fusion or move further down the domain. Fission and fusion events were assumed to be instantaneous.

Mitophagy in the stochastic simulations was implemented by setting a cutoff level ϕ for the health of an individual mitochondrion. Whenever a mitochondrion's health dropped below that cutoff, it was labeled as "engulfed". An engulfed mitochondrion moved in the retrograde direction ($-v\Delta t$) on each time-step and was not subject to fusion, fission, or stopping events. Once it reached the proximal end of the domain (position 0) it was removed from the simulation. The total number of mitochondria in the domain (M) included these engulfed particles. However, their health levels were not included in any calculations of health at the demand sites. Simulations with mitophagy (Fig. 3.8, 3.9, 3.10) were carried out with $M = 300$.

For S7 Fig, additional stochastic simulations were carried out for a variant of the CoG model with explicitly fixed total number of mitochondria in the domain. Specifically, M mitochondria were initially placed uniformly at random in the domain in a motile state. Each time a retrograde mitochondrion reached $x = 0$, it switched immediately into an anterograde mitochondrion with health level reset to 1. No new mitochondria were produced, and the system was allowed to run for 10^5 time-steps to reach steady-state. The number of mitochondria therefore stayed fixed throughout, regardless of the presence of mitophagy.

3.6.5 Optimizing performance in the presence of mitophagy

For each of the plots showing the effect of mitophagy in Fig. 3.8, 3.9, the effective stopping rate was set to give a particular value of N_s. Simulations were carried out with $n = 10$ demand sites, and $M = 300$ average total mitochondria in the domain.

For the data shown in Fig. 3.8, 3.9, the fraction of stopped mitochondria was set to $f_s(\phi = 0) = 0.53$ in the absence of mitophagy. In the SS model, a number $f_s M_0$ of permanently stationary mitochondria were placed evenly distributed among all the demand sites. In the CoG model, the restarting rate k_w was set according to Eq. 3.4, for each value of N_s. The production rate was then set according to Eq. 3.3, to give the desired number of motile mitochondria in the domain at steady-state. The value of k_p was not changed as the mitophagy cutoff increased, so that higher mitophagy in Fig. 3.8 corresponds to fewer total mitochondria in the domain.

In Fig. 3.9, the value of k_p was also kept constant, but the resulting health levels were normalized by the total actual number of mitochondria in the domain. Because properly normalized health levels are not sensitive to the absolute number of mitochondria, this procedure was equivalent to explicitly fixing the total number of mitochondria. A direct comparison for the CoG model with explicitly fixed M is provided in Supporting Information (S7 Fig).

Optimization of normalized health over all parameters (Fig. 3.10) was carried out by running simulations with 100 independent iterations each for a 10×10 grid of N_s and f_s values, for each mitophagy cutoff ϕ. The normalized average health and normalized last region health was computed for each set of parameter values, and the maximum of each for a given ϕ was found. The parameters that led to this maximum were then used to run another set of 10 identical simulations of 100 iterations each, to compute the standard deviation in the resulting normalized health. Error bars in Fig. 3.10 correspond to the standard error of the mean from these independent replicates.

3.7 Acknowledgements

Chapter 3, in full, is a reprint of the material as it appears in Agrawal, A. and Koslover, E.F. "Optimizing mitochondrial maintenance in extended neuronal projections", *PLOS Computational Biology*, 17(6), p.e1009073. (2021). The dissertation author was the primary author of this paper.

Table 3.1. Physiological parameter values estimated from published data for Chapter 3

Input Parameters		
Symbol	Description	Value used
L	Length of axonal domain	1 - 10 cm
k_d	Decay rate of mitochondrial protein	$(4\text{days})^{-1}$
M	total number of mitochondria in the axonal domain	Variable (depending on length of domain)
n	Demand sites in axonal domain	Variable
k_p	Production rate of mitochondria at the soma	Variable
v	Speed of mitochondria in an axon	0.5 μm/s
k_w	Rate of re-entry of stationary mitochondria to motile pool	Variable
p_s	Stopping probability of motile mitochondria at demand sites	Variable
p_f	Probability of transient fusion between a motile and stationary mitochondria	Variable
ϕ	Health threshold for mitophagy	Variable
α	local translation fraction	$5-30\%$
Effective Derived Parameters		
Symbol	Description	Formula
ρ	Steady-state density of motile mitochondria	$2k_p/v$
S	Steady-state number of stationary mitochondria at each demand site	$v\rho p_s/k_w$
f_s	Fraction of mitochondria in the stationary pool	$\frac{nS}{M}$
$\widehat{k}_w$	Effective restarting rate in Space Station model	$\frac{p_f}{2}v$
$\widehat{p}_s$	Effective probability of protein stopping at a demand site in Space Station model	$1-(1-p_f/2)^S$
$\widehat{k}_d$	Non-dimensionalized decay rate	k_dL/v
N_s	Number of stopping events during a protein's back and forth journey in the domain	$2\widehat{p}_sn$
r	rate of local translation per mitochondrion; only stationary mitochondria import local proteins	$\alpha v/(2L)$

Chapter 4

Dendritic architecture determines mitochondrial distribution patterns in vivo

4.1 Abstract

Mitochondria are critical for neuronal function and must be reliably distributed through complex neuronal architectures. By quantifying in vivo mitochondrial transport and localization patterns in the dendrites of Drosophila visual system neurons, we show that mitochondria make up a dynamic system at steady-state, with significant transport of individual mitochondria within a stable global pattern. Mitochondrial motility patterns are unaffected by visual input, suggesting that neuronal activity does not directly regulate mitochondrial localization in vivo. Instead, we present a mathematical model in which four simple scaling rules enable the robust self-organization of the mitochondrial population. Experimental measurements of dendrite morphology validate key model predictions: to maintain equitable distribution of mitochondria across asymmetrically branched subtrees, dendritic branch points obey a parent-daughter power law that preserves cross-sectional area, and thicker trunks support proportionally bushier subtrees. Altogether, we propose that "housekeeping" requirements, including the need to maintain steady-state mitochondrial distributions, impose constraints on neuronal architecture.

4.2 Introduction

Neurons are energetically demanding cells with complex morphologies. Mitochondria produce most of the ATP in neurons, and all parts of the neuron need ATP. In addition, some subcellular structures (e.g. synapse) are more energetically demanding than others, so mitochondria must be distributed throughout neurons in specific patterns in order to meet energetic demands. Mitochondria are also highly dynamic: they grow and degrade, divide and fuse, and move through the cell. Thus, in order to maintain stable mitochondrial distribution patterns over time, neurons must somehow coordinate mitochondrial dynamics over large, elaborately branched axonal and dendritic arbors. Mitochondrial motility, in particular, has been extensively studied in neurons[196, 68, 170]. Mitochondrial motility in neurons is bidirectional: mitochondria can move away from the soma and into axonal and dendritic processes, or out of the processes back towards the soma. For an individual mitochondrion, the mechanics governing motility are relatively clear [14]. In brief, the motor proteins kinesin and dynein transport mitochondria along microtubules[158]. Adaptor proteins link mitochondria to motor proteins[137], and anchoring proteins oppose mitochondrial movement [97]. Whether a particular mitochondrion moves, and in which direction, depends on the number and orientation of microtubule tracks, as well as the relative amount of force generated by populations of motor proteins versus anchoring interactions [2]. It is unclear, however, how neurons regulate these molecular scale interactions across space and time in order to maintain large-scale mitochondrial distribution patterns. In some cases, neurons may control mitochondrial localization patterns by regulating the spatial distribution of signals that trigger motility arrest (by modifying motor-adaptor proteins or activating anchoring interactions), resulting in mitochondrial enrichment within regions where mitochondria are most likely to stop. Along these lines, one attractive hypothesis in the field is that neuronal activity contributes to mitochondrial localization patterns by regulating motor engagement[118]. Specifically, kinesin and dynein are known to bind to mitochondria via the Miro/Milton adaptor complex[209]; Miro is a mitochondrial outer membrane protein[59], and

Milton is an adaptor protein[196]. Several lines of evidence from cultured cells have shown that high levels of calcium induce a conformational change in Miro that results in motor disengagement and motility arrest[216, 119, 176]. Synaptic activity drives local calcium influx in neurons, and calcium-dependent arrest of mitochondrial movement could enrich mitochondria in subcellular regions with high synaptic densities and energetic demands[119]. However, there is no evidence that physiological calcium signals arrest mitochondrial movement in vivo. On the contrary, a small number of studies suggest that calcium signals have no effect on mitochondrial movement in neurons in vivo [50, 194, 190]. Similarly, high glucose levels have been shown to trigger mitochondrial halting in cell culture, through the O-GlcNacylation of the Milton adaptor [153]. However, the role and extent of such glucose-mediated localization in vivo remains unclear. In addition to regulating mitochondrial localization patterns by controlling the balance between movement and arrest, neurons could control the flux of mitochondria in subcellular compartments. In this scenario, mitochondria would be enriched in regions where more microtubule tracks allow for higher rates of mitochondrial delivery. EM studies have shown that microtubule numbers are proportional to the thickness of neuronal processes in various cell types[92], so the shape of a neuron is likely to play a role in mitochondrial transport patterns. The relationship between transport rates and scaling across branch points in tree-like structures — i.e. the relative thickness of parent and daughter branches, as well as the relative sizes of sister subtrees that sprout from each branch point — has been studied in various contexts, from botanical trees[48, 105] to the vascular system [139]. In neurons, theoretical work has defined various scaling rules to optimize wiring economy [30, 37, 221], electrical signaling [164, 32], and, to a lesser extent, transport [112]. However, there is no comprehensive theory or experimental evidence that defines the relationship between neuronal architecture, mitochondrial transport, and large-scale mitochondrial distribution patterns.

To interrogate the relationship between neuronal architecture and dynamic mitochondrial localization patterns, it is important to conduct experiments in vivo, such that neurons retain their physiological morphologies. To that end, neurons in the *Drosophila* visual system called

horizontal system (HS) neurons were used as a model system in this work. There are three HS neurons per optic lobe of the fly (six in total), all of which are functionally equivalent [179]. HS neurons detect global optic flow patterns by dendritic integration of local motion input signals [15]. HS dendrites are highly branched and amenable to in vivo imaging [219]. In this work, we combined experimental measurements of in vivo mitochondrial transport, mitochondrial localization patterns, and the architecture of HS dendrites with mathematical modeling to determine how dendritic branching patterns contribute to steady-state mitochondrial localization patterns. We found that although mitochondria in HS dendrites are highly motile, large-scale mitochondrial distribution patterns are conserved across HS cells, with mitochondria consistently enriched in distal dendrites, relative to primary dendrites, and equitably distributed across asymmetrically branched arbors. Our experimental measurements are consistent with a mathematical model in which simple dendritic scaling rules enable robust self-organization of steady-state mitochondrial localization patterns in HS dendrites. Consistent with previously published work [50, 194, 190], our experimental observations also indicate that physiological neuronal activity does not affect mitochondrial motility. Altogether, this work demonstrates that dendritic architecture, not neuronal activity, determines mitochondrial localization patterns in vivo in *Drosophila* HS dendrites.

4.3 Results

4.3.1 Experimental measurements of mitochondrial localization patterns and motility

In order to understand how neurons reliably distribute mitochondria throughout complex architectures, members of the Barnhart group at Columbia University used publicly available serial section transmission electron microscopy (ssTEM) images of an entire fly brain ("Female Adult Fly Brain," or FAFB) to measure mitochondrial localization patterns in HS neurons. Dendrites, but not axons, often contained large, branched mitochondria that spanned multiple

dendritic branches (Figure 4.1A). On average, the total mitochondrial density in HS neurons is 20 % (mitochondrial density = 0.19 +/- 0.04 STE), but there was significant variation in the total mitochondrial density across the six HS neurons in the FAFB dataset. Whereas the total mitochondrial density in four of the cells was 12%, the density in the other two cells was 33%. Despite this variation in overall mitochondria density, it was found that mitochondrial localization patterns were conserved across all six HS neurons in the FAFB dataset. In dendrites but not axons, mitochondrial densities increased with distance from the soma, such that mitochondrial densities were approximately three times higher in the distal-most dendrites compared to the primary dendrite (Figure 4.1 C). At each branch point within a dendritic arbor, a parent branch splits into two daughter branches, and the entire arbor can be decomposed into successive pairs of sister subtrees. (Figure 4.1D). Whereas in some cases the dendritic arbor splits in a symmetric fashion (Figure 4.1D), it was found that sister subtrees are often asymmetric: one subtree is, on average, 2.5 times longer than the other (Figure 4.1E; fold difference in total sister subtree length = 2.5x +/- 0.4. STE). Despite this asymmetry in sister subtree size, mitochondria are equitably distributed across branch points such that sister subtrees have equivalent mitochondrial densities (Figure 4.1D-E). Altogether, these results show that mitochondria in HS dendrites follow a specific distribution pattern, with equitable distribution across sister subtrees and mitochondrial enrichment in distal dendrites.

We hypothesized that the observed localization patterns emerge from a dynamic steady-state in which individual mitochondria are continually reorganizing within a stable, global pattern. To test this hypothesis by measuring mitochondrial motility patterns, the Barnhart group used the GAL4/UAS binary system to drive expression of GFP-tagged mitochondria (mitoGFP) and a cytosolic volume marker (tdTomato) in HS neurons. Then, in vivo confocal microscopy was used to image HS dendrites in living, head-fixed Drosophila. Measurements of mitochondrial motility in primary and distal dendritic branches indicate that mitochondria moving in the anterograde direction in distal dendrites were significantly slower and less persistent than in the primary dendrite (Figure 4.2B). Measurements further indicated that there was balanced anterograde

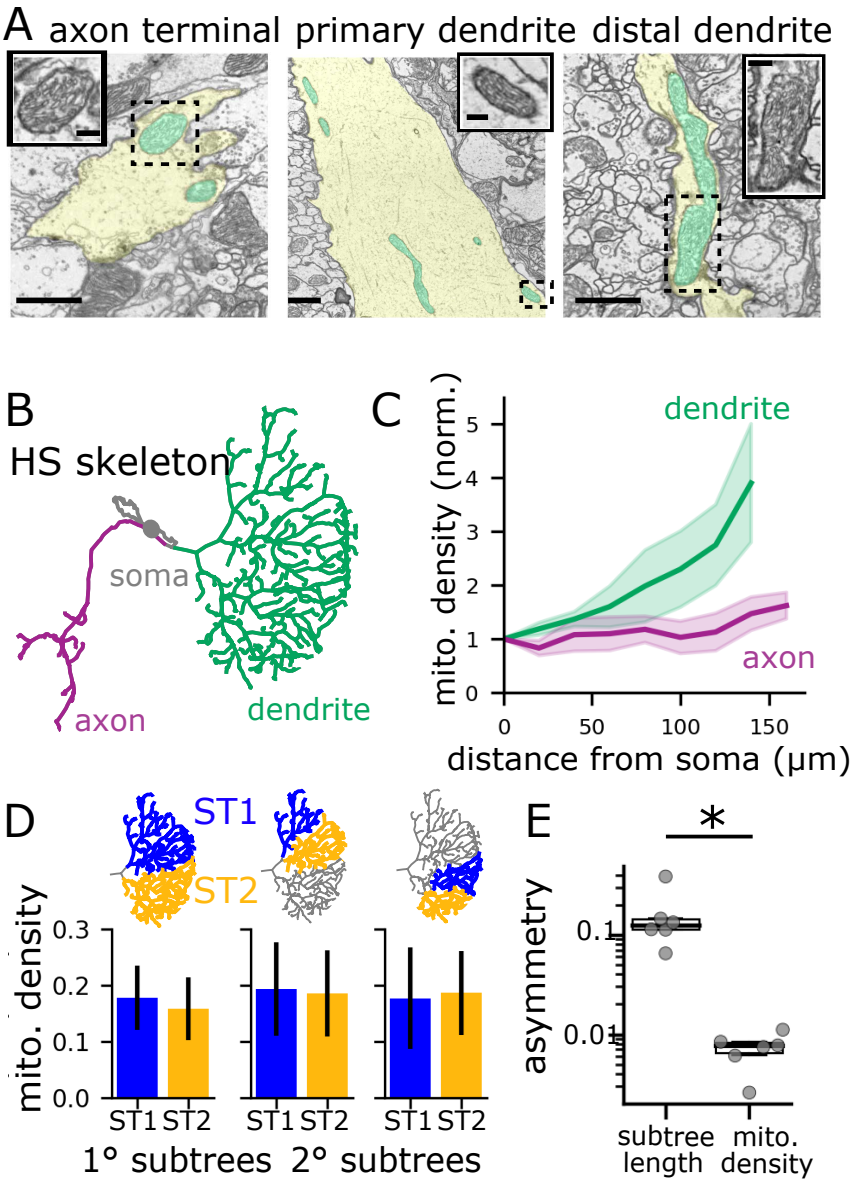

Figure 4.1. Mitochondrial localization patterns in HS dendrites Figure courtesy of Barnhart Lab, Columbia University.
A: TEM images of mitochondria (cyan) in different compartments of an HS neuron (yellow); scale bars are 1 μm. Dashed boxes indicate the regions enlarged in the inset images (inset scale bars are 200 nm). B: Skeleton of an HS neuron traced through ssTEM images. C: Average mitochondrial densities plotted versus distance from the soma in the dendrite (green) and axon (magenta). $N = 6$ neurons; shaded regions indicate the standard error of the mean. For each cell, mitochondrial densities are normalized to the density in the primary dendrite near the soma. D: Mitochondrial densities in sister subtree pairs. Error bars are bootstrap 95% confidence intervals. E: Sister subtree asymmetries in subtree length and mitochondrial density (asymmetry $= ((ST1 - ST2)^2/(ST1 + ST2)^2)^{1/2}$, averaged over all sister subtree pairs per cell); $p < 0.01$ (T-test).

and retrograde transport through the primary dendrite, suggesting that the total amount of mitochondria in the HS arbor remains constant over time. The measurements of mitochondrial density and motility can be leveraged to estimate the fraction of dendritic mitochondrial volume that is motile versus stationary. The mitochondrial mass exchange rate was measured to be 1 μm^3 every minute for the primary dendrite (Figure 4.2 D). Based on this rate of mitochondrial volume exchange ($J \sim 1\mu m^3$/min), the typical speed of motile mitochondria ($v \sim 0.4\mu m/s$), the mitochondrial volume density in primary dendrites ($c_{primary} \sim 10\%$), and its cross-sectional area ($A_d \sim 30\mu m^2$) in the primary dendrite, we estimated that the fraction of motile mitochondria in this proximal region is $f_m = 2J/(vcA_d) \sim 3\%$. Mitochondrial density is higher in the distal dendrites ($c_{distal} \sim 30\%$), and we therefore estimate an even lower motile fraction for the distal portions of the dendritic arbor ($\sim 1\%$). Thus, the majority of the mitochondrial population is stationary at any given moment. However, we also estimate that the total volume of mitochondria in the dendritic arbor exchanges through the primary dendrite many times over the lifetime of the neuron. Based on the mitochondrial density in the whole dendrite ($c \sim 20\%$), the total volume of the dendritic tree ($V_d \sim 2000\mu m^3$ [37]), and the rate of mitochondrial volume exchange ($J \sim 1\mu m^3$/min), we estimate a mitochondrial volume exchange rate normalized to the total mitochondrial volume in the dendrite: $J_{norm} = J/(cV_d) \sim 15\%/\text{hr}$. At this rate, the entire mitochondrial volume in an HS arbor reorganizes in less than ten hours, or more than one hundred times over the course of a fly's lifetime. Altogether, these results are consistent with the idea that the mitochondria in HS dendrites make up a dynamic system at steady-state.

How do HS dendrites maintain steady-state mitochondrial distribution patterns, given rapid reorganization of mitochondrial mass? HS neurons are part of global motion detection circuits in Drosophila, and they are selectively activated by specific patterns of global motion [179, 94]. Previous work from the Barnhart group found that global motion stimuli drive calcium increases in the distal dendrites of HS neurons [15]. Calcium arrests mitochondrial motility in cultured neurons ([216]). If stimulus-evoked calcium signals are stronger in the distal dendrites than in the primary dendrite, then calcium-dependent arrest of mitochondrial transport could

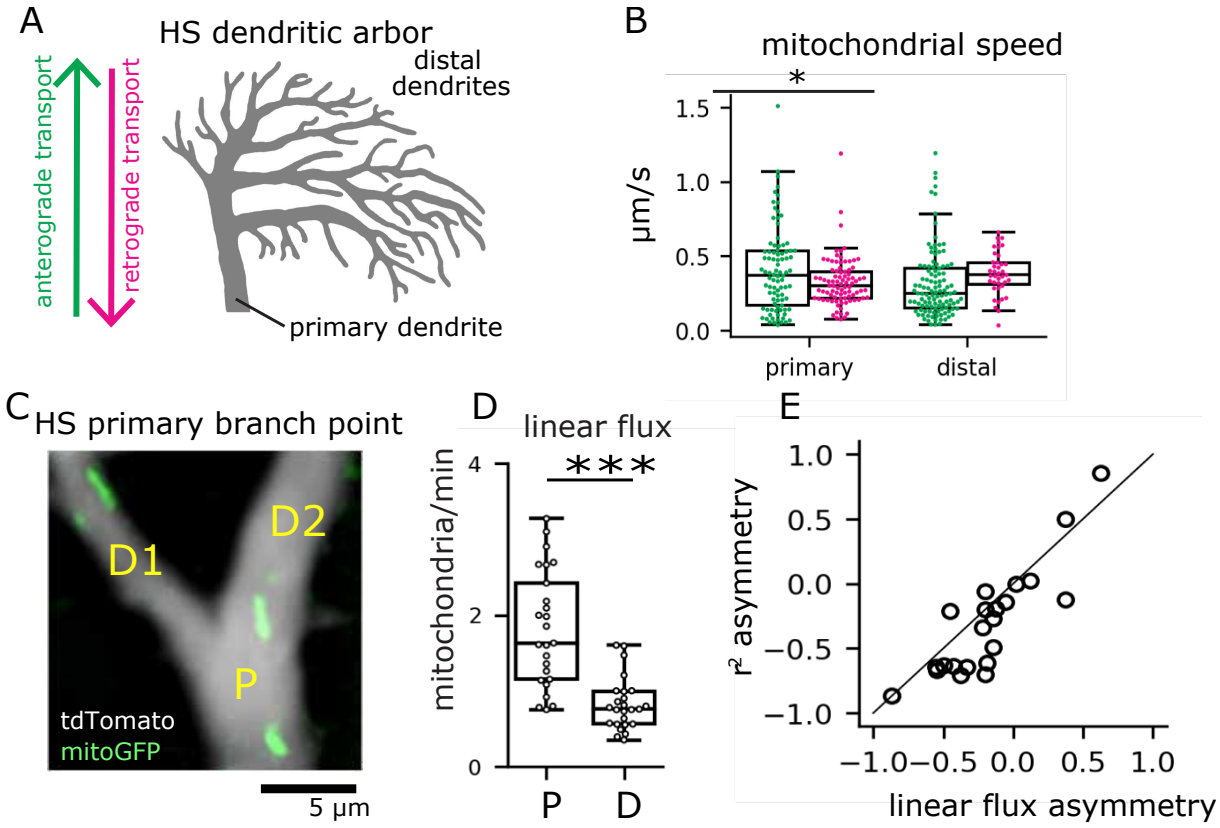

Figure 4.2. Mitochondrial transport in HS dendrites. Figure courtesy of Barnhart Lab, Columbia University.

A: Schematic depicting an HS dendritic arbor, including primary and distal dendrites and the direction of anterograde versus retrograde transport. B: Average speed of mitochondria moving through primary or distal mitochondria in the anterograde (green) or retrograde (magenta) directions. Each dot represents an individual mitochondrion. The asterisk indicates a signicant dierence (one way ANOVA, post-hoc Tukey's test). C: Confocal image of an HS primary branch point. A parent branch (P) splits into two daughter branches (D1 and D2). D: Mitochondrial linear flux rates in parent and daughter branches; asterisks indicate a signicant dierence (Student's T-test, $p < 0.001$). E: Asymmetry in daughter branch cross-sectional areas (r^2) plotted versus asymmetry in mitochondrial linear flux rates; asymmetry $= (D1 - D2)/(D1 + D2)$, $N = 25$ branch points

increase the density of mitochondria in the distal dendrites, relative to the primary dendrite. Experimental measurements did indicate that stimulus-evoked calcium signals correlate with mitochondrial density, with larger calcium response amplitudes and mitochondrial densities in the distal dendrites compared to the primary dendrites. However, it was found that visual stimulus-evoked calcium signals are not sufficient to arrest mitochondrial motility in HS distal dendrites (Supplemental Figure C.1). The stimulus did not affect mitochondrial speeds (Supplemental Figure C.1C), nor mitochondrial transport rates (Supplemental Figure C.1D). Thus, physiologically-relevant calcium signals do not affect mitochondrial motility in HS dendrites in vivo.

4.3.2 Simple scaling rules recapitulate experimental measurements of mitochondrial localization patterns

We next hypothesized that dendritic architecture, rather than neuronal activity, determines steady-state mitochondrial localization patterns in HS cells. To test this idea, we developed a quantitative model of mitochondrial transport and localization patterns in HS dendrites. In developing this model, we assumed the mitochondrial distribution to be governed by the morphology of the dendritic arbor (relating branch widths with subtree structures) as well as the local relationship between dendrite width and mitochondrial transport rates. Specifically, we defined four simple scaling relationships governing mitochondrial localization patterns:

1. **Splitting of mitochondria at branch points** When mitochondria move in the anterograde direction across branch points (i.e. from a parent branch into one of two daughter branches), more mitochondria move into the thicker daughter branch. We assume that the probability of a mitochondrion moving into a given daughter branch is proportional to the cross-sectional area of the branch, according to $p_1/p_2 = r_1^2/r_2^2$, where p_1 and p_2 are the probabilities that a mitochondrion moves from the parent into daughter 1 or 2, and r_1 and r_2 are the radii of the two daughters. Since thicker branches have thicker microtubule bundles, more mitochondria can enter a thicker vs thinner branch. This assumption is supported by

experimental measurements (Figure 4.2) indicating that mitochondrial downstream fluxes split proportional to the cross-sectional area of daughter branches at each junction.

2. **Power law scaling of parent and daughter branch widths** Consistent with several previous studies, we assume that parent and daughter radii scale according to the power law $r_0^\alpha = r_1^\alpha + r_2^\alpha$, where r_0 is the radius of the parent branch. The exponent α determines the extent to which the total dendritic cross-sectional area increases or decreases in the daughter branches, relative to the parent: area is conserved if $\alpha = 2$, decreases if $\alpha < 2$, and increases if $\alpha > 2$. Although experimental evidence for any particular form of power law scaling in neurons is sparse, optimal values for α have been derived based on theoretical arguments for preservation of graded electrical signals across dendritic branch points ($\alpha = 3/2$, often called "Rall's Law" after the neuroscientist Wilfrid Rall), action potential propagation in axons ($\alpha = 3$, often called "Murray's Law" and first derived for the vasculature system), or efficient intracellular transport ($\alpha = 2$, often called "Da Vinci scaling" after Da Vinci's rule for trees). Recent work in larval Drosophila sensory neurons indicates that Da Vinci scaling, along with a correction for minimal radius at the distal tips, is consistent with observed arbor morphologies [112].

3. **Scaling of mitochondrial transport with dendrite radius** Our in vivo measurements of mitochondrial transport show that mitochondria are significantly more likely to arrest motility in thin distal dendrites than in the thick primary dendrite. Based on this, we assume that the rate of mitochondrial arrest, k_s, scales with dendrite radius according to $k_s \sim 1/r^\beta$. This relationship incorporates a width-dependence for the population-averaged speed of mitochondrial transport in different dendritic branches.

4. **Scaling of sister subtree size with trunk thickness** Finally, we assume that larger subtrees are supported by proportionally thicker trunks, with trunk radii scaling with either total subtree length, volume, or some other measure of subtree size. This scaling, along with

proportional mitochondrial transport at branch points, should ensure that larger subtrees receive a proportionally larger supply of mitochondria.

To determine how these scaling rules contribute to steady-state mitochondrial localization patterns, we developed a mathematical model of mitochondrial transport in dendritic trees. In this model, each dendrite is a binary tree, with each junction node connecting a parent edge to two daughter edges. We assume that each edge e_i is a cylinder with fixed radius r_i along its entire length ℓ_i. In our model, the connectivity and length of each edge in a tree are known attributes, either extracted from skeletons of real HS neurons in the FAFB dataset, or from synthetic trees with varying branching patterns. Radii of each branch are set according to various rules for parent-daughter and sister subtree scaling (rules 2. and 4., Fig. 4.3).

Within this dendritic structure, we assume that discrete mitochondrial units undergo active transport, which includes processive motion in the anterograde and retrograde directions, as well as arrest and restarting. The ratio of arrest and restarting rates (k_s/k_w) determines the local fraction of stationary mitochondria in each dendritic branch. We assume the restarting rate is constant throughout the arbor, but allow the arrest rate to vary in dendrites of different width (scaling rule 3., Fig. 4.3). Finally, in all model versions, the anterograde mitochondrial linear flux entering a junction node is split in proportion to the cross-sectional area of the daughter branches, so that wider daughter branches receive proportionally more mitochondria (rule 1., Fig 4.3).

Figure 4.3. A mean field model for mitochondrial distributions recapitulates experimental measurements when dendrites obey specific scaling rules.
A: Scaling rules included in the model. 1. Mitochondrial arrest rate increases as branch thickness decreases, $k_s \sim 1/r^{\beta}$ 2. Mitochondria split equitably across branch points 3. There is a scaling relationship of the form $r_0^{\alpha} = r_1^{\alpha} + r_2^{\alpha}$ between the parent (r_0) and daughter (r_1, r_2) widths parametrized by the exponent α. 4. Sister subtrees scale such that thicker trunks support proportionally larger subtrees. Subtree size can be subtree volume, length, or bushiness, where bushiness is length/depth. B: In the model, dendrites are binary trees in which each junction node connects a parent edge to two daughter edges (center panel). Each edge is a cylinder with fixed radius (r) along its entire length (l). The connectivity and length of each edge are extracted from real HS dendrite skeletons (left panel); radii are set according to various forms of parent-daughter and sister subtree scaling rules. Within this dendritic structure, mitochondria can move persistently in either the anterograde (v^+) or retrograde (v^-) direction, as well as arresting and initiating motility (right panel). For simplicity, we assume a constant motility initiation rate (k_w) and constant velocities v^+ and v^-. C-F: Model results. Dendrite topologies (edge length and connectivity for each dendritic branch) were extracted from HS skeletons traced through ssTEM images (circles, N = 6 dendrites, Michael Reiser, unpublished results) or previously published HS dendrite reconstructions (triangles, N = 20 dendrites, [38]). Mitochondrial density asymmetry across sister subtrees (C,D) and distal mitochondrial enrichment (E, F) were calculated for $\beta = 0$ (C,E) or $\beta = 2$(D,F), $\alpha = 2$ (cyan), 3/2 (red), or 3 (purple), and sister subtree scaling with subtree trunks splitting according to $r_1 = r_2$ (eq.), $r^2 \sim L$, or $r^2 \sim L/D$. The mitochondrial density asymmetry is the root-mean squared asymmetry across sister subtrees ST1 and ST2, where asymmetry = (ST1-ST2)/(ST1+ST2). Distal enrichment is mitochondrial density in the distal-most dendritic branches, defined as branches with path distance from the root node $\geq 75\%$ of the maximum path distance, divided by the mitochondrial density in the primary dendrite. Box plots show the median, interquartile range, and 1.5x the interquartile range.

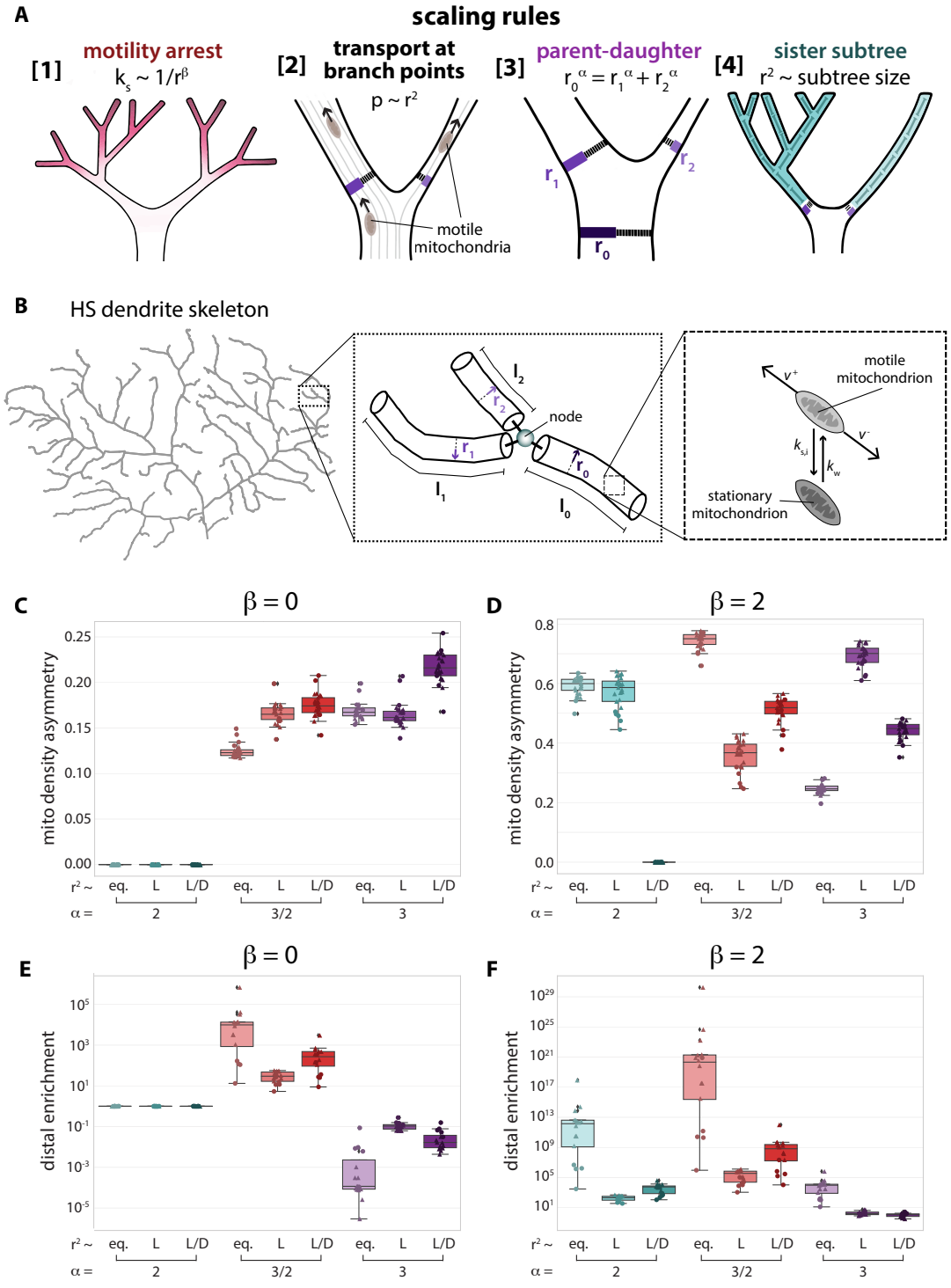
A
scaling rules
[1]
motility arrest
$k_s \sim 1/r^{\beta}$
[2]
transport at branch points
$p \sim r^2$
motile mitochondria
[3]
parent-daughter
$r_0^{\alpha} = r_1^{\alpha} + r_2^{\alpha}$
[4]
sister subtree
$r^2 \sim$ subtree size
B
HS dendrite skeleton
node
motile mitochondrion
stationary mitochondrion
C
β = 0
D
β = 2
mito density asymmetry
E
β = 0
F
β = 2
distal enrichment
$r^2 \sim$ eq. L L/D eq. L L/D eq. L L/D
α = 2 3/2 3

We implemented several versions of this model, using different forms of parent-daughter, sister subtree, and transport scaling rules (rules 2., 3., 4.), through analytical solutions of mean-field equations for mitochondrial density and stochastic simulations. For all model versions, we calculated mitochondrial densities as a function of distance from the soma and across sister subtrees to determine which scaling rules recapitulate our experimental measurements (i.e. distal enrichment and equitable distribution of mitochondria across sister subtrees). In the first, simplest iteration of our model, we incorporated two of the four scaling relationships described above: equitable splitting of mitochondria at branch points (rule 1), and power law scaling of parent and daughter radii (rule 2.), with $\alpha = 3/2$ (Rall's law), $\alpha = 2$ (Da Vinci scaling), or $\alpha = 3$ (Murray's law). The mitochondrial arrest rates and transport speeds are assumed to be independent of dendrite thickness ($\beta = 0$ in Rule 3.), so that the fraction of stationary versus motile mitochondria is constant throughout the arbor. Because the linear flux of mitochondria at each junction splits in proportion to the daughter branch cross-section, the steady-state volume density of mitochondria in two sister branches is equal. When $\alpha = 2$, the total cross-sectional area is conserved at each junction, giving rise to constant mitochondrial volume densities throughout the arbor, regardless of the tree topology and regardless of the choice of sister subtree trunk radii (Rule 4). Thus, Da Vinci parent-daughter scaling results in equitable distribution of mitochondria across sister subtrees, but not distal enrichment in this minimal version of our model. In contrast, when the narrowing of daughter branches is governed by Rall's Law ($\alpha = 3/2$), the reduction in total cross-sectional area at each branch point results in distal enrichment of mitochondria. For this model, the relative volume density of mitochondria in sister subtrees depends on the choice of splitting rule for the sister trunk radii at each junction (Rule 4). In Appendix Section C.0.1, we show that for an arbor obeying Rall's Law it is impossible to establish equitable mitochondrial distributions between asymmetric sister subtrees with any single functional form for the sister trunk radii as a function of the subtree morphology. In particular, subtrees with more splitting junctions tend to accumulate higher mitochondrial densities due to the reduction of dendritic cross-sectional area below each junction in a tree with $\alpha = 3/2$.

For the case of Murray scaling ($\alpha = 3$), the cross-sectional area increases below each junction point, so that mitochondrial volume densities are lower in more distal regions of the arbor. Altogether, when mitochondrial transport parameters are spatially uniform, our model recapitulates either distal enrichment of mitochondria (for Rall-scaled dendrites), or equitable distribution of mitochondrial across sister subtrees (for Da Vinci-scaled dendrites), but not both.

In the first version of our model, we assumed spatially uniform mitochondrial transport parameters. However, our experimental measurements indicate that in thin distal dendrites, average mitochondrial speeds are lower and arrest rates are higher than in the thick primary dendrite, and we reasoned that scaling of mitochondrial transport with dendrite radius could result in increased mitochondrial densities in thin distal dendrites. We therefore updated our initial model such that mitochondrial transport rates scale with dendrite radii. Specifically, we begin by assuming that mitochondrial arrest rates are inversely proportional to dendrite cross-sectional area, $k_s \sim 1/r^2$ ($\beta = 2$ in scaling rule 3), while mitochondrial motility initiation rates and speeds are still spatially uniform. Different assumptions about the scaling of mitochondrial transport with branch thickness (e.g. scaling of mitochondrial speed with dendrite radius, such that mitochondria move more slowly in thin dendrites) give the same results when the fraction of motile mitochondria is very small fraction (see Appendix), as we observed experimentally. We consider a version of this model with equitable splitting of mitochondria at branch points (rule 1), and Da Vinci scaling of parent and daughter branch width ($\alpha = 2$ in rule 2). This model predicts that motile mitochondria densities will be constant throughout the tree, while stationary mitochondria densities will be higher in distal dendrites. If we assume that daughter branch radii are split equally ($r_1 = r_2$) at each junction, then asymmetric topologies of sister subtrees lead to asymmetry in the mitochondrial distribution, with more-branched subtrees acquiring a higher mitochondrial density. Next, we investigated whether an alternate relationship between the trunk widths of sister subtrees could restore equitable distribution of mitochondria across subtree pairs. According to our analytical calculations (see Appendix Section C.0.2), when $k_s \sim 1/r^2$, the ratio of stationary mitochondrial densities in a pair of sister subtrees is

given by $c_1^{(s)}/c_2^{(s)} = \frac{(L_1/V_1)}{(L_2/V_2)}$, where $c^{(s)}$ is the density of stationary mitochondria and L and V are subtree length and volume. Equitable distribution of mitochondria therefore depends on a specific morphological relationship between sister subtrees: the total subtree volume must be proportional to its length, such that $L_1/V_1 = L_2/V_2$. For an arbor that follows the Da Vinci scaling law, the preservation of cross-sectional area across branch points implies that the total volume of a tree can be expressed as $V = r_0^2 D$, where r_0 is the radius of the tree trunk and D describes the effective depth of the tree. For a tree where all terminal dendritic branch tips are the same distance d from the trunk, the effective tree depth is $D = d$; for trees with distal tips at varying distances from the trunk, the effective depth we define D can be computed recursively (see Appendix Section C.0.2). In a tree with Da Vinci parent-daughter scaling, all subtrees will exhibit a volume proportional to their total branch length if and only if the sister subtree trunk areas scale according to the following relation: $r_1^2/r_2^2 = \frac{(L_1/D_1)}{(L_2/D_2)}$. The ratio of total length over depth (L/D) can be thought of as the "bushiness" of a tree. In trees with no branch points, $L = D$ and thus $L/D = 1$. In trees with many branch points (i.e. bushier trees), $L \gg D$ and $L/D \gg 1$. Trees that follow different sister subtree scaling rules (e.g. with radii splitting proportional to subtree length) do not exhibit equitable distribution of mitochondria across sister subtrees. Altogether, we show that this model (with dendritic trees obeying Da Vinci parent-daughter scaling, inverse scaling of mitochondrial arrest and dendrite thickness, and sister subtree trunk areas proportional to tree bushiness) successfully recapitulate the key features of experimentally observed mitochondrial distributions: equitable densities between sister subtrees and increased density in distal branches.

4.3.3 HS dendrites follow simple dendritic scaling rules

Our model results indicate that realistic mitochondrial localization patterns can be achieved in two scenarios. If HS dendrites follow Da Vinci parent-daughter scaling, realistic mitochondrial distributions can be achieved if motility arrest rates are inversely proportional to dendrite thickness (measured as the cross sectional area r^2) and sister subtree trunk areas

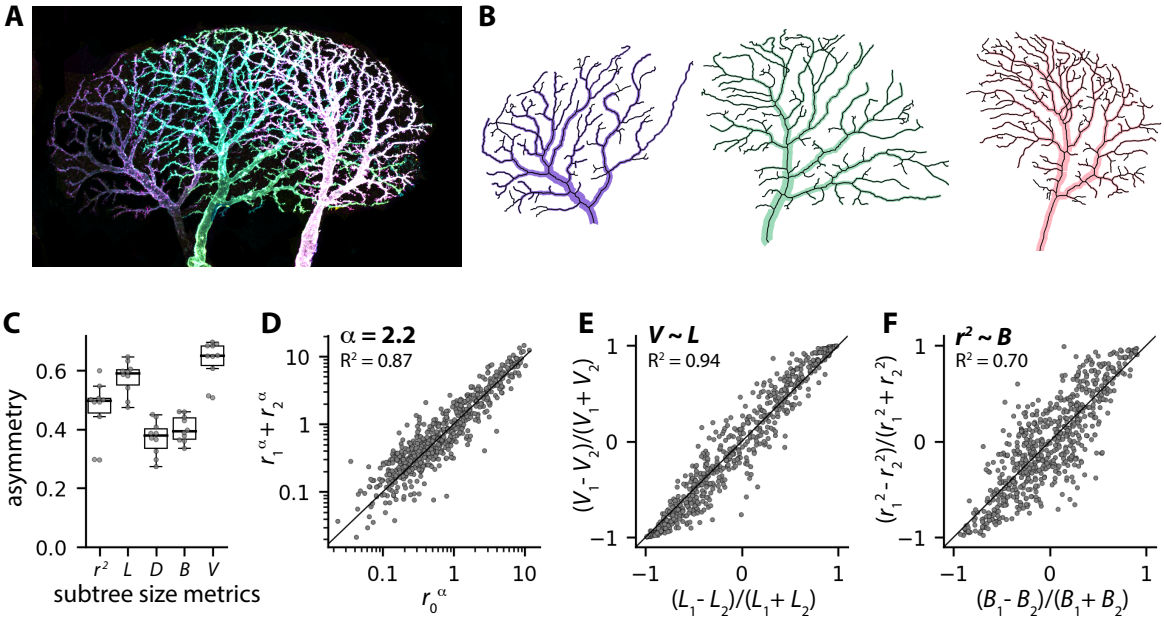

Figure 4.4. Drosophila HS dendrites follow proposed morphological scaling rules.
A-B: MCFO image of three HS dendrites (A) and extracted skeletons and radii (B). C: Box plots showing sister subtree asymmetries in trunk thickness (r^2), length (L), depth (D), bushiness (B), and volume (V). Black lines, boxes, and whiskers indicate the median, interquartile range, and 1.5 times the interquartile range, respectively, and each gray dot indicates the average value for a single cell (N = 10 HS dendrites). D-F: HS dendrites follow parent-daughter scaling $r_0^\alpha = r_1^\alpha + r_2^\alpha$, $\alpha = 2.2$ (D), and sister subtree scaling with subtree volume proportional to subtree length (E) and trunk thickness (r^2) proportional to subtree bushiness (F). N = 649 branch points from 10 dendrites.

are proportional to the bushiness $b = L/D$ of the subtree. Alternatively, if HS dendrites follow Rall's law parent-daughter scaling, no single rule for sister trunk widths as a function of subtree morphology will yield equitable splitting of mitochondria across all sister subtrees (see Appendix Section C.0.1). Instead, bushier subtrees with more junctions will tend to accumulate higher mitochondrial densities, due to the decrease in total daughter cross-sectional area at each junction. To determine whether HS dendrites exhibit power law parent-daughter scaling with $\alpha = 2$ (Da Vinci scaling) or $3/2$ (Rall's law), we measured HS dendritic architecture. We used stochastic multicolor FlpOut labeling to label individual HS dendrites, which we then imaged by confocal microscopy. Next, we segmented and skeletonized each dendrite before measuring parent and daughter branch radii and the length, volume, and bushiness of the subtrees sprouting from each branch point. We found, first, that HS dendrites are asymmetrically branched, with significant asymmetry in daughter branch thickness and subtree length, volume, and bushiness. Second, we fit our measurements of parent and daughter radii to the power law $r_0^\alpha = r_1^\alpha + r_2^\alpha$ for $\alpha = 2$ or $3/2$. We found that $\alpha = 2$ gave a reasonably good fit ($R2 = 0.86$) with a minor improvement for best fit parameter $\alpha = 2.2$ ($R2 = 0.87$), indicating that HS dendrites exhibit Da Vinci parent-daughter scaling. Next, our model predicts that Da Vinci-scaled dendrites can only achieve equitable distribution of mitochondria if sister subtrees have volumes proportional to their length.. To test this prediction, we compared the asymmetry in subtree lengths $(L_1 - L_2)/(L_1 + L_2)$ with the asymmetry in volumes $(V_1 - V_2)/(V_1 + V_2)$ for sister subtree pairs emerging from the same branch point. We found that length asymmetry is equal to volume asymmetry for a population of 649 subtree pairs extracted from 10 HS dendritic arbors ($R2 = 0.94$), indicating that longer sister subtrees have proportionally larger volumes, as predicted. Thus, HS dendrites obey two separate morphological rules: Da Vinci power law scaling of parent and daughter branches ($r_0^2 = r_1^2 + r_2^2$), and sister subtree splitting with volume proportional to length ($L_1/V_1 = L_2/V_2$). According to our model, for dendrites that follow these two rules ,daughter branch cross-sectional areas must be proportional to subtree bushiness: $r_1^2/r_2^2 = \frac{(L_1/D_1)}{(L_2/D_2)}$. To test this prediction, we compared asymmetry in branch cross-sectional area $(r_1^2 - r_2^2)/(r_1^2 + r_2^2)$ to asymmetry in subtree

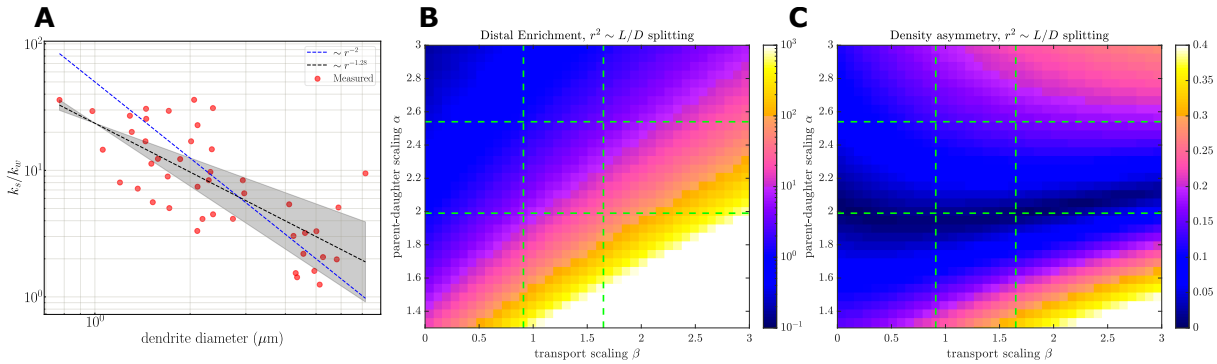

Figure 4.5. Equitable mitochondrial distributions are robust to changes in transport scaling. A: Dendrite diameters plotted versus mitochondrial arrest rate k_s. The dashed line indicates the best fit, with $k_s \sim 1/r^{1.3}$. B-C: Model results showing average distal mitochondrial enrichment (B) and mitochondrial density asymmetry across sister subtrees (C) calculated as a function of α (parent-daughter scaling) and β (transport scaling). HS dendrite topologies were extracted from MCFO images (N = 10 cells) and dendrite radii were set according to sister subtree scaling rule $r^2 \sim L/D$, as well as power law parent-daughter scaling with the indicated range of values for α.

bushiness $\frac{(L_1/D_1)-(L_2/D_2)}{(L_1/D_1)+(L_2/D_2)}$. We found that area and bushiness asymmetry are also correlated ($R2 = 0.70$), indicating that thicker trunks support proportionally bushier subtrees, as predicted. These experimental results, along with our model, strongly suggest that dendrite morphology plays a key role in determining steady-state mitochondrial localization patterns in neurons in vivo.

4.3.4 Robust self-organization of equitably distributed mitochondria for a range of transport parameters

In our model, we assume that mitochondrial arrest rates are inversely proportional to the cross-sectional area of each dendritic branch ($k_s \sim 1/r^2$). Inverse scaling of mitochondrial arrest and dendrite thickness results in increased mitochondrial densities in thin distal dendrites, as well as the length-volume constraint on sister subtrees. To measure the relationship between mitochondrial arrest rates and dendrite thickness directly, we used our in vivo imaging setup to image mitochondria moving through dendritic branches with a range of radii. We measured the fraction of mitochondria that stopped or paused as a function of dendrite radius and found that mitochondrial arrest is indeed more frequent in thinner branches, as expected. However,

arrest rate scaled with dendrite radius according to $k_s \sim 1/r^{1.3}$, indicating that mitochondrial arrest rates have a weaker dependence on branch radius than we originally assumed ($\beta = 1.3$ in rule 3). To determine how this scaling affects equitable distribution of mitochondria in our model, we computed mitochondrial densities across sister subtrees for mitochondrial arrest rates that obey power law scaling with dendrite radius ($k_s \sim 1/r^{\beta}$) for a range of exponents ($\beta = 0$ to 3) as well as a range of $\alpha = 1.4 - 3$. In Figure 4.5 we use $r^2 \sim L/D$. We found that when parent and daughter radii follow Da Vinci scaling ($\alpha = 2$) and sister subtree trunks split according to subtree bushiness, perfectly equitable distribution of mitochondria occurs for $\beta = 0$ (spatially uniform mitochondrial arrest rates) and $\beta = 2$ (arrest rates inversely proportional to dendrite cross-sectional area). Intermediate values for β, including $\beta = 1.3$, result in very small asymmetries across sister subtrees, comparable to what we measured experimentally. In contrast, other parent-daughter scaling rules (i.e. Rall's law or Murray's law) failed to yield equitable mitochondrial distributions for any choice of non-zero β. Other sister subtree scaling rules (e.g. trunks splitting according the subtree length, rather than bushiness, Supplemental Figure C.5) only yielded equitable mitochondrial distributions when $\beta = 0$. Thus, equitable mitochondrial distributions are robust to changes in β specifically when dendrites follow the morphological scaling rules we measured for HS dendrites.

In contrast, we found that distal enrichment of mitochondria does depend on β. Higher values of β correspond to increased sensitivity of arrest rates to the narrowing of distal dendritic branches. Hence, higher β implies increased distal enrichment of mitochondria (Figure 4.5B). In our model, values for α and β in the range of our experimental measurements result in both realistic distal enrichment ($\sim$ 10 fold enrichment) and equitable mitochondrial densities in dendrites that obey $r^2 \sim L/D$ sister subtree scaling.

The predicted distal enrichment is reduced when we deviate from the Da Vinci scaling law and implement a 'minimum radius' r_m, such that the relationship between parent and daughter

branch widths is expressed according to:

$$r_0^2 + r_m^2 = r_1^2 + r_2^2 \tag{4.1}$$

.

This modification was previously introduced to describe Drosophila ClassIV dendritic arbors [112]. We fit a value of $r_m^2 \sim 0.2\mu m^2$ to our measured branch width data, and calculate expected results (Supplemental Figure C.5). Including a minimum radius brings the predicted mitochondrial enrichment closer to the experimental prediction of 3-fold distal enrichment.

4.4 Discussion

4.4.1 Summary of main results

Mitochondria form a dynamic, interconnected network, organized across neuronal architecture in order to meet energetic demands that fluctuate over spatial and temporal scales. Here, we provide in vivo evidence for mitochondrial localization over time in neurons, which simultaneously maintain dynamic transport, and specific localization patterns. From previous studies using cultured neurons, neuronal activity has long been thought to play a role in regulating mitochondrial localization patterns [216, 119]. Neuronal stimulation evokes global calcium transients which is thought to arrest mitochondria through detachment of mitochondria from microtubules [216, 119]. However, our results demonstrate that stimulus-induced calcium signals do not affect mitochondrial motility in *Drosophila* HS dendrites *in vivo*. Instead, our results suggest that dendritic architecture, not neuronal activity, determines steady-state mitochondrial localization patterns. By combining mathematical modeling with experimental measurements, we define scaling rules that link dendritic architecture and mitochondrial transport rates to steady-state mitochondrial localization patterns. We find that we can recapitulate our experimental findings by modeling mitochondrial localization with four simple scaling relationships. First, mitochondrial transport scales with branch radius. Second, mitochondria split according to cross-sectional area

at branch points. Third, sister subtrees length and volumes scale proportionally. Finally, parent and daughter branches follow power scaling laws. Our work demonstrates that mitochondria form a dynamic and reorganizing network in which simple dendritic scaling laws enable robust self-organization of steady-state mitochondrial localization patterns.

4.4.2 Molecular and physical mechanisms underlying motility arrest in distal dendrites

Mitochondrial arrest rates are inversely proportional to dendrite branch radius in HS cells (Figure 4.5A), and this scaling is critical for distal enrichment of mitochondria in our model (Figure 4.5). What is the mechanism underlying inverse scaling of motility arrest and branch thickness? The simplest possibility is that non-specific viscous friction between motile mitochondria and the cell boundary opposes mitochondrial movement in thin distal dendrites, similar to those observed in axons [227]. If mitochondrial arrest is determined by the friction of the dendrite membrane opposing mitochondrial transport, then we would expect to see larger mitochondria subject to higher friction and thus, higher mitochondrial arrest. As previously reported in cultured *Drosophila* neurons, there is an inverse relationship between mitochondrial size and mitochondrial velocity [140]. Larger mitochondria are expected to experience greater opposition to motion due to increased friction between the mitochondria and membrane [140]. However, cultured neurons do not form morphologically complex neurite branching structures or distinct axons and dendrites. When we assess the relationship between mitochondrial velocity and mitochondrial size in HS dendrites, we do not see any significant differences in vivo. Therefore, viscous friction alone is not likely to explain in vivo HS mitochondrial arrest rates, since there is not a significant relationship between the size and the arrest rate of mitochondria. Alternatively, anchoring interactions mediated by specific protein tethers may promote mitochondrial arrest in thin distal dendrites. Previous studies have identified a role for the microtubule tether syntaphilin in arresting mitochondria [89, 211]. Syntaphilin is a mammalian, neuron-specific protein which docks mitochondria to microtubules. However, since syntaphilin is axon-specific [86] and

not conserved in *Drosophila*, it cannot explain our results of scaling mitochondrial arrest with dendrite diameter. Even with extensive studies into mitochondrial transport machinery [77], there are no studies which have identified any specific protein anchors of mitochondria in dendrites. Another possibility is that actin-based anchoring, potentially mediated by myosin V may result in higher arrest rates in thin dendrites. There are several contexts where actin based anchoring has been shown to oppose microtubule based transport [151, 90, 117]. Other organelles have also been studied, including lysosomes which tether near actin patches at dendritic spines via myosin Va [16]. This competition between actin based anchoring and microtubule transport could become more pronounced with dendrite narrowing in the distal dendrites due to the localization of actin and microtubules. While microtubules fill the dendrite shaft and number scales with branch radius squared [92], actin localizes around the branch perimeter and should scale with branch radius [107]. Within the literature, there is reported enrichment of actin in multiple cell types, including in the dendritic spines of lobula plate tangential cells (LPTCs) [107] and terminal dendrites in da neurons [144]. Thus, in thicker dendrites, microtubule based transport could be favored, while in thinner dendrites, actin might compete with transport, and lead to higher mitochondrial arrest rates. Finally, although we measure a correlation between dendrite radius and mitochondrial arrest rates, reduced dendrite radii in distal dendrites may not cause increased arrest. Instead, arrest rates may depend upon spatial differences in microtubule orientation (more mixed orientation distally) [200, 90], fusion rates (higher distally), and spatial patterning of either anchoring proteins (increased concentration in thin dendrites) or adaptor proteins (reduced concentration in thin dendrites). For example, rates of fission and fusion depend upon the size of the mitochondrion and the contact rates [22]. Although we did not find any siginificant difference in the length of motile mitochondria in the primary or distal dendrites, we do know the overall density of mitochondria increases in thinner distal dendrites which should increase their contact rates and therefore lead to greater fusion in distal dendrites. Further studies to assess the spatial dynamics of microtubules, fission and fusion rates, and adapator proteins will elucidate their role in determination of mitochondrial arrest localization.

4.4.3 Functional consequences of specific localization patterns

Mitochondria in HS dendrites are enriched in distal dendrites (Figure 4.1C) and localize equitably across sister subtrees (Figure 4.1 1D). What are the functional implications of this specific localization pattern? The equitable distribution of mitochondria across sister subtrees can be rationalized given the function of HS neurons. HS neurons detect front-to-back global optic flow patterns by selectively sampling and pooling local motion inputs from their upstream elementary motion detectors [15]. Since HS cell function relies on integrating synaptic inputs across its entire dendritic arbor, summing individual dendritic branches with approximately equal weight [15], the energy demands in HS dendritic branches are also expected to be equitably distributed. Given mitochondria produce the majority of the ATP needed for the neuron [71], we expect sister subtrees to have equitable mitochondrial distributions in order to meet those equivalent energetic demands. Furthermore, we expect synapse density to increase with distance from the soma. Even though we did not measure synapse density, and there have been efforts to do so in the past [175], we expect from previous studies that most of the synaptic connections in HS are expected to occur in the distal regions of the cell [124]. In addition to their role in energy homeostasis, mitochondria are also known to buffer calcium which may be important at sites with high fluctuations including synapses [39]. Although we consistently measured relatively higher mitochondrial densities in the distal than proximal dendrites across all HS neurons, we also found variation in the absolute amount of mitochondrial volume. This varied absolute volume of mitochondria across HS cells may indicate that that mitochondrial densities may not be as tightly linked to energy homeostasis as we had predicted. Alternatively, the distal enrichment of mitochondria may be linked to the dynamics of mitochondrial fission and fusion. The splitting and mixing of mitochondria through fission and fusion may provide a path for maintaining homogeneous mitochondrial health throughout the entire mitochondrial network [22]. In the distal dendrites, there is higher density of mitochondria where more fusion of mitochondria could lead to higher mixing rates than in the primary dendrites. Quantifications of fission and fusion

rates are limited [22, 173], but there is evidence of morphological differences in mitochondria across compartment which may be due to differential fission and fusion rates. Through our sparse 3D reconstructions throughout the arbor, we have found evidence of large, branching mitochondria throughout the distal dendrites, which is supported by previous reports in other systems [161, 57]. Distal enrichment of mitochondria due to higher rates of fusion in the distal dendrites could support mitochondrial health in regions far from the soma.

4.4.4 General applicability of scaling laws

We find that all HS reconstructed neurons have distal enrichment of mitochondria (Figure 4.1) and equitable distribution across sister subtrees (Figure 4.1). However, there are cell to cell differences in the relative scales of mitochondrial volume and neuronal volume across HS cells. How generalized are our proposed scaling rules across diverse neuronal morphologies? Power law scaling relationships are expected to be conserved across neuronal cell types. Power-law scaling relationships are found throughout the natural world and have been used to describe relationships at bifurcations ranging from rivers and trees [129] to vasculature [139]. The power-law is $r_1^\alpha + r_2^\alpha = r_0^\alpha$, where r_0 is the diameter of the parent branch, and r_1 and r_2 are the diameters of the respective daughter branches, and α is an exponent. Power law scaling is scale-invariant [58], indicating that a change in the relative size of the parent branch should relatively scale with the change in size of the daughter branches. This scale transformation should preserve the functional relationship between parent and daughter branches across cell types. Our model for dendritic scaling uses parent and daughter diameters scaling with $\alpha = 2$ (Da Vinci's law) in order to maintain proper mitochondrial localization patterns. Da Vinci's law ($\alpha = 2$), originally derived from a tree's branching system, suggests a conservation of cross-sectional area across branch points[48]. Da Vinci used this pattern to explain how trees can withstand wind and load stress on their branches. This scaling has also been assessed in other tree-like structures, such as a river course feeding into a mainstream [105] and neuronal dendrites [112, 100]. Although experimental support for Da Vinci scaling remains comparably

scarce, it points to an important transport constraint, as the cross-sectional area of a branch is invariantly linked to microtubule density, and thus motor-driven transport [221, 112]. Our original estimation of $\alpha = 2$ is consistent with experimental evidence that distal dendritic tips contribute to the major energetic demands of the neuron [50], and thus dendrites need to be optimized for transport mechanisms as mitochondria are trafficked far from the site of biogenesis in the soma. Other theoretical derivations include Rall's law ($\alpha = 3/2$), which models neuronal processes as cables with electrical conductivity. Assuming that impedance remains uniform across branch points, Rall's law minimizes the dissipation of electrical signal and action potential delays by decreasing the size of the daughter branches relative to the parent branches [164] . While this scaling was originally derived using cat motoneurons, there has been little further experimental evidence of neurons following Rall's law, likely since the neuron must balance other constraints, such as transport and wiring costs [32]. Murray's law ($\alpha = 3$) minimizes the energetic loss arising from the frictional dissipation of pumping fluid through a vessel and the burden of fluid size on the system [139, 103]. This has been experimentally verified in the mammalian cardiovascular system [103, 198] throughout all stages of development, suggesting that fluid mechanics govern the morphogenesis of blood vessel formation. Interestingly, a value of $\alpha = 3$, which minimizes the cost functions, has also been experimentally observed in myelinated neuronal axons such as to minimize the combined cost of signal propagation delays and axonal volume [32]. Regardless of the exponent of branch diameter thinning, the wealth of morphological data available due to connectome efforts will allow us to test how generally applicable our model holds in morphologically and functionally diverse neurons.

4.4.5 Extent to which we think neuronal activity could affect motility and localization in other neuronal cell types

In HS dendrites, mitochondrial transport is unaffected by visually evoked physiological stimulus (Figure C.1). This lack of mitochondrial arrest with induced calcium transients contrasts with previous in vitro results [118, 216, 176] but is supported by more recent in vivo studies

[50, 190, 194]. Given our model and evidence from similar LPTCs being structurally hard-wired [183] meaning unaffected by neuronal activity, then we would not expect the mitochondrial network to reorganize with changes in neuronal activity. If neuronal activity does not impact mitochondrial localization in HS dendrites, then does it have other effects on mitochondria? Rather than affect mitochondrial localization, neuronal activity may alter mitochondrial function, cristae structure, total mitochondrial volume or rates of other mitochondrial dynamics. ATP production is thought to be regulated through a variety of mechanisms from calcium homeostasis [199] to cristae morphology [152]. The function of mitochondria, such as the rate of ATP production, is affected by neural activity which drive both ATP consumption and ATP synthesis via oxidative phosphorylation [165, 127]. The structure of the inner folds of the mitochondrial membrane are also thought to contribute to the capacity to produce ATP: lamellar, straight cristae are more closely associated with high energy dissipation capacity. Since ATP synthase requires curvature of the inner mitochondrial membrane to dimerize [33], then lamellar mitochondria may produce less ATP than more open mitochondria. Thus, mitochondria with various degrees of folding of inner cristae may have variations in energy production [157]. We found that although the localization of mitochondria and normalized mitochondrial densities were consistent across HS neurons, the overall volumes of mitochondria varied from cell to cell. This fluctuation in volume could indicate differences in the efficiency of mitochondrial ATP production and therefore total volume needed to achieve required energy production or a lower level of regulation in mitochondrial volumes in HS cells. Further work to characterize the relationship between mitochondrial morphology and ATP production would allow us to incorporate the energy production of mitochondria across the neuron into our model for predicting mitochondrial localization patterns based on energetic demands.

Alternatively, the localization of mitochondria in cell types with activity-dependent plasticity may be altered in parallel with changes to the neuron [9]. The main structural changes include changes to neuronal branching [63], and volume [172], or functional plasticity altering synaptic components [195, 148]. In our model, these alterations in neuronal structure could

therefore induce alterations in mitochondrial localization and transport patterns.

4.4.6 Model as framework for understanding localization - adding in additional layers of complexity

Our model formulates a quantitative model for understanding mitochondrial localization in neurons using assumptions of mitochondrial transport and neuronal architecture in one cell type (Figure 4.3). In order to build this model we have made several assumptions of mitochondrial dynamics. With further quantification of dynamic properties of mitochondria, this initial framework can have more elements added to more precisely predict mitochondrial distribution patterns across diverse neuronal morphologies. Our first assumption is all mitochondrial mass originates and terminates within the soma. This would mean that biogenesis and degradation are exclusive to the soma, however, degradation of mitochondria can occur outside of the soma [4]. Mitochondria are degraded and regenerated by a variety of mechanisms [5]. First, misfolded or damaged proteins can get degraded by mitochondrial proteases [42]. Second, mitochondria-derived vesicles (MDVs) bud off from the mitochondria containing damaged components which then fuse with peroxisomes, lysosomes or undergo exocytosis [197]. Third, depolarized mitochondria are targeted with phospho-ubiquitin to trigger the formation of autophagosome membranes that completely engulf the mitochondria [135]. It has been shown that this macroautophagic process is active at synaptic points [101]. Lastly, mitochondria can also be degraded transcellularly as they shed from their neuron through the formation of large protrusions and are subsequently incorporated into surrounding glial cells where they fuse with lysosomes [41]. In Drosophila, there are more glial cells near the edges of the neuropils [55], meaning that for HS dendrites, glial cells are predominantly found near the dorsal subtrees, closer to the border of the lobula plate. Since our model assumes biogenesis and degradation occur within the soma, further work to characterize these local mechanisms of mitochondrial clearance could account for the variation in total mitochondrial volume across HS cells (Figure 1). Next, our model does not account for the dynamics of mitochondrial fission and fusion which

alter mitochondrial volumes throughout the cell [232]. Although the machinery of mitochondrial fission, relying on proteins Drp1 and Fis1, and fusion, relying on MFN1 and OPA1, are well described [95], the mechanisms regulating their dynamics at the cellular level are not well understood [22]. Previous studies have characterized the cyclical dynamics of mitochondrial fission and fusion [23, 215] and how these dynamics are affected by mitochondrial size and motility in rates of fission and fusion [23]. Further studies will seek to build onto this model by incorporating models of mitochondrial fission and fusion dynamics. Our next assumption is mitochondria have equitable energy production and health. Our model accounts for the localization of mitochondria across the entire network, but does not distinguish mitochondria based on the state of mitochondrial health or energy production. Whether anterograde moving mitochondria are healthier than retrograde mitochondria remains a contested issue. Bidirectional transport is crucial as disruptions in retrograde movement have been shown to lead to an accumulation of damaged mitochondria in the periphery of axons [125, 45]

4.5 Methods

4.5.1 Image segmentation and tree morphology extraction

Tree morphologies were extracted using custom MATLAB [130] code available at https://github.com/lenafabr/networktools.

To obtain the skeletons for the dendritic trees from MCFO images, we processed the images in Ilastik using a trained pixel classifier to generate probability maps. We subsequently used thresholding, morphological operations, and connected component analysis to generate a binary mask in python. We cleaned-up and skeletonized these masks in Fiji/ImageJ using the plug-in function “Skeletonize (2D/3D)”. Skeleton data was translated into a set of nodes (including junction nodes, parent node, and distal tips) with three-dimensional coordinates, and curved edge paths connecting the nodes. Once the initial network structure was extracted, manual clean-up was carried out with a custom Matlab GUI, involving the removal of short spurious

branches ('shrubs') from the network. A degree of subsequent manual editing was performed for each cell, such that shorter branches with a discernable thickness were reintroduced into the network object and those without an identifiable thickness were removed.

We used Fiji with its built-in line tool function to measure parent and daughter diameters and Matlab to measure total subtree length, volume, depth, and bushiness following each branch. The widths of network branches were also adjusted with the aid of the Matlab GUI. The interface allows the user to add and adjust width measurements across a given edge. For longer edges, one measurement point close to the branching point and the other closer to the end of the edge are chosen.

For the calculation of predicted mitochondrial densities (Figures 4.3, 4.5), the extracted tree topology and branch lengths were used as input for imposing putative branch radii according to various scaling laws, as described below.

4.5.2 Synthetic tree construction

Synthetic binary trees were constructed in Python 3.7.6 using the NetworkX library [69]. First, the skeleton of a binary tree was created, starting with a single junction consisting of a parent branch and two daughter branches of unit length. Moving downstream along the tree, each daughter branch either terminated as a distal tip (with probability $\frac{1}{3}$), increased in length by an additional unit (probability $\frac{1}{3}$), or branched into two more daughter branches (probability $\frac{1}{3}$). This process was repeated up to a preset maximum path distance from the arbor parent node to the distal tips. The resulting random-topology binary tree structures were used as the ensemble of synthetic arbors in Figures 4.3, 4.5, C.3 and C.4.

In addition, 20 arbor structures for Drosophila HSN neurons were obtained from previously published data [37].

4.5.3 Computing imposed radii

Skeletons with well-defined branch lengths and connectivity were obtained either from images of Drosophila HSN neurons, from published data [37], or from synthetically constructed trees. For each skeleton, the widths of the branches (r_i) were calculated, starting with $r_0 = 1$ at the parent trunk (in dimensionless units). At each junction node, the daughter branch radii were defined by a combination of scaling rule 1. for parent and daughter radii: $r_1^\alpha + r_2^\alpha = r_0^\alpha$ and rule 4. for sister subtree radii $r_1^2/r_2^2 = \mu_{12}$. Da Vinci arbors have $\alpha = 2$, Rall's Law arbors have $\alpha = 3/2$, and Murray's Law arbors have $\alpha = 3$.

The daughter branch splitting rules included equal splitting ($\mu_{12} = 1$), splitting in proportion to total subtree length ($\mu_{12} = \sum_{i \in ST1} \ell_i / \sum_{i \in ST2} \ell_i$), and splitting in proportion to subtree bushiness (total branch length over depth), defined in Appendix Section C.0.2.

To estimate the effect of measurement error in branch width (Supplemental Figure C.4), we added a Gaussian noise term with standard deviation equal to 30% of the computed radius to all branch widths r_i. Supplemental Figure C.4 shows that such measurement noise is more apparent when comparing the splitting of individual sister trunk radii as opposed to the length and volume proportionality of sister subtrees (which include summation over many subtree branches).

4.5.4 Mean-field model for mitochondrial distribution

Our minimal mean-field model allows the calculation of steady-state mitochondrial densities along each branch of a dendritic arbor with prescribed topology, branch lengths, and branch radii. We assume punctate mitochondria are produced at the soma (parent node of the arbor), and undergo processive bidirectional motion with pause free velocity v_i (where i is the branch index), pausing rate $k_{s,i}$, and constant restarting rate k_w. The linear densities of anterograde, retrograde, and stationary mitochondria in each branch are given by $\rho_i^+, \rho_i^-, \rho_i^s$,

respectively. At steady-state, these densities obey the transport equations:

$$\frac{d\rho_i^{\pm}}{dt} = \mp v_i \frac{d\rho_i^{\pm}}{dx} - k_{s,i}\rho_i^{\pm} + \frac{k_w}{2}\rho_i^s = 0 \tag{4.2a}$$

$$\frac{d\rho_i^s}{dt} = k_{s,i}(\rho_i^+ + \rho_i^-) - k_w \rho_i^s = 0 \tag{4.2b}$$

The steady-state solutions have densities that are constant along each individual branch, with the relationship between different branch densities determined by boundary conditions at the junctions. Distal tips are treated as reflecting boundaries (yielding $\rho_i^+ = \rho_i^-$). At the branch junctions, the boundary conditions are set by the conservation of incoming and outgoing mitochondrial flux, together with the assumption that anterograde mitochondria split in proportion to the cross sectional area of the daughter branches:

$$v_i\rho_i^{\pm} = v_j\rho_j^{\pm} + v_k\rho_k^{\pm}, \frac{v_j\rho_j^+}{v_k\rho_k^+} = \frac{r_j^2}{r_k^2} \tag{4.3a}$$

where i is the parent branch, and j, k the two daughter branches at the junction. Finally, we set the boundary condition at the soma by fixing the motile mitochondria linear density in the parent trunk to a constant, ρ_0. The steady-state linear densities of mitochondria in each branch are then found by solving this set of linear equations. The density of stationary mitochondria is given by:

$$\rho_i^s = \frac{k_{s,i}}{k_w}\rho_i^w \tag{4.4a}$$

where $\rho_i^w = \rho_i^+ + \rho_i^-$ is the motile mitochondrial density.

4.5.5 Volume densities and equitability metric

Volume density on each branch is computed as $c_i = \rho_i / r_i^2$. The average volume density in a subtree is given by:

$$\left\langle c^{(s)} \right\rangle_{\mathrm{ST}} = \frac{\sum_{i \in ST} \rho_i^{(s)} \ell_i}{\sum_{i \in ST} r_i^2 \ell_i} \tag{4.5}$$

Where the summation is carried out over all branches i of the subtree, with corresponding length ℓ_i and radius r_i.

We define a single metric ζ for the deviation from equitability of mitochondrial distribution throughout the entire tree. Specifically, this metric gives the root-mean-squared asymmetry of mitochondrial densities in sister subtrees, averaged over all junctions in the arbor. We focus on the regime where most mitochondria are in the stationary state, and hence compute the asymmetry metric based specifically on distributions of stationary mitochondria:

$$\zeta = \sqrt{\frac{1}{N_b} \sum_b \left(\frac{\langle c^s \rangle_{b,1} - \langle c^s \rangle_{b,2}}{\langle c^s \rangle_{b,1} + \langle c^s \rangle_{b,2}} \right)^2}. \tag{4.6}$$

Here, the index b enumerates the junctions, N_b is the total number of junctions in the tree, and subscripts 1 and 2 refer to the two daughter subtrees emanating from a junction.

4.5.6 Agent-based simulations of mitochondrial transport

Stochastic simulations of mitochondrial transport in a network were carried out using custom code written in Fortran 90. An initial tree structure is initialized to contain information on the junction connectivity, as well as lengths and radii of individual branches. The tree skeletons were generated using the NetworkX library as described in section 4.5.2. A typical example is presented in Figure C.3. The widths of these synthetic trees were calculated by imposing either Da-Vinci scaling law with $r^2 \sim L/D$, or rall's splitting law with $L \sim V$ scaling applied. For demonstrating the simulated results showing the difference in equitability of mitochondrial distribution in trees following Da-Vinci vs Rall's scaling, $N = 10$ synthetic trees were used. The

edge lengths for the synthetic tree were fixed to $\ell_0 = 10\mu$m, consistent with average edge length measurements observed in HS dendrites. While these synthetic trees were shorter in extent compared to real HS neurons due to computational limitations (going a maximum of $D/\ell_0 = 4$ levels down), the synthetic trees incorporated a range of heterogeneity in branching structure.

The tree is then populated by a fixed number ($N = 1000$) of punctate of mitochondria, distributed uniformly throughout. The position of each mitochondrion is tracked in terms of the branch on which it is located and its position along the branch. Each mitochondrion is associated with a transport state (anterograde, retrograde, or stationary).

On every timestep, an anterograde mitochondrion steps distance $v\Delta t$ downstream along the branch, and a retrograde mitochondrion steps distance $v\Delta t$ upstream. The velocity of an individual mitochondrion was assumed to be $v = 0.4\mu$m/s. One time step corresponds to $\Delta t = 2.5$ s, so that the stepping distance $v\Delta t = 1\mu$m. A motile mitochondrion switches to a stationary state with probability P_{stop}, whereas a stationary mitochondrion becomes motile with probability P_{start}, according to the corresponding rates:

$$P_{stop} = 1 - e^{k_{s,i}\Delta t} \tag{4.7a}$$

$$P_{start} = 1 - e^{k_w \Delta t} \tag{4.7b}$$

When becoming motile, the mitochondrion is equally likely to enter the enter the anterograde or retrograde state. The rate of switching from motile to stationary state was fixed according to observations of mitochondrial motility in HS dendrites, which yielded the dimensionless ratio $k_s/k_w = 35$ in the primary dendrite. The rate k_s for a primary dendrite was set equal to $0.15/s$ and the rate k_w was set equal to $2 \times 10^{-3}/s$, so that on an average a mitochondrion had a probability $P_{stop} = 0.31$ of stopping in a primary dendrite at each timestep. The stopping to walking rate was tuned as a function of branch radii according to the rule $k_s \sim 1/r^2$.

At each junction, an anterograde mitochondrion chooses which daughter branch to enter with probability proportional to the cross-sectional area of the branch: $p_1/p_2 = r_1^2/r_2^2$. When

an anterograde mitochondrion reaches the distal tip, it reverses and becomes retrograde. When an retrograde mitochondrion reaches the soma, it becomes anterograde again. The simulations were run for $N_{steps} = 10^8$ to ensure convergence in observed mitochondrial distributions, as monitored by the time-shifted edge concentration autocorrelation function calculated for each edge: $C_{c_{edge}}(\tau) = \frac{1}{t}\sum_0^t (c_{edge}(t) - < c_{edge} >_t)(c_{edge}(t+\tau) - < c_{edge} >_t)$

Where $c_{edge}(t)$ is the density at the edge at time t, $< c_{edge} >_t$ is the time-averaged density at that edge. The convergence time τ is when $C_{c_{edge}}(\tau) \to 0$.

4.6 Acknowledgements

Chapter 4, in part, is currently being prepared for submission for publication of the material. Donovan, E. J.*, Agrawal, A.*, Liberman, N., Kalai, J. I., Chua, N. J., Koslover, E. F. and Barnhart, E. L. , 2021. "Dendritic Architecture Determines Mitochondrial Distribution Patterns *in vivo*." The dissertation author was one of the primary authors of this material.

Appendix A

Appendix for Chapter 2

A.1 Estimating physiological parameter values

In this appendix we describe our approach to estimating the parameter values summarized in Table 2.1 from published experimental data.

A.1.1 Glucose diffusivity (D)

glucose is a small molecule of comparable molecular weight to ATP, which has a diffusion coefficient of $140\mu m^2/s$ [134, 210]

A.1.2 Glucose consumption rate per mitochondrion (k_g)

The oxidative capacity of muscle mitochondria has been measured at 5.8 mL of O_2 per min per mL mitochondria[72, 182]. We assume 6 glucose molecules are consumed per molecule of oxygen, and a volume of $0.3\mu m^3$ for globular mitochondria[162]. The corresponding glucose turnover rate of a mitochondrion is then calculated as 1.3×10^5 glucose per second per mitochondrion.

A.1.3 Axon radius (r)

The thickness of mammalian brain axons varies widely from 0.1μm to 10μm[156]. Statistical measurements in the human brain show that most axon diameters fall below 1μm, with a long-tailed distribution of substantially thicker axons[113]. We take as our estimate a median

diameter of 0.8μm, which is consistent with measurements in human brain regions[113], in the rat corpus collosum[13], guinea pig retinal neurons[155], and in a number of other mammalian tracts[156].

A.1.4 Internodal distance (L)

Typical internodal lengths vary widely from 200μm to 1500μm [83, 35]. We use a value of $L = 250\mu$m as measured in the axons of rat anterior medullary velum[81].

A.1.5 Mitochondrial density ($\overline{M}$)

Measurements of mitochondrial concentration in human spinal muscular nerves give a linear density of about 15 mitochondria per 100μm of axon[228]. Similar densities are observed in Fig. 1, 2 of Ref. [153]. Assuming an axonal radius of $r \approx 0.4\mu$m gives a corresponding density of $0.3\mu\text{m}^{-3}$. EM measurements in rat brain neurons indicate that mitochondria occupy approximately 8% of the neuronal cytoplasmic volume[163]. Assuming a mitochondrial volume of $0.3\mu\text{m}^3$[162] would give the same density estimate of 0.3 mitochondria per μm^3.

A.1.6 Hexokinase Michaelis-Menten constant (K_M)

The Michaelis-Menten constant for glucose phosphorylation by the neuronal isoform of hexokinase (HKI) has been measured as $K_m = 0.03$mM[224].

A.1.7 Ratio of stopped to moving mitochondria (k_s/k_w)

In Ref. [153], mammalian neurons grown under high (30mM) glucose conditions were found to have mitochondria that spent approximately 5% of their time in motion. This fraction should correspond to $k_w/(k_s + k_w) \approx 0.05$ under our simplified model for mitochondrial motility.

A.1.8 Membrane permeability to glucose (P, K_{MP})

The neuronal glucose transporter GLUT3 in rat cerebellar granule neurons has been measured to have a turnover rate of $k_{\text{glut3}} = 853\text{s}^{-1}$ and a Michaelis-Menten constant of

$K_{M,\text{glut3}} = 3\text{mM}$ [123]. In the same study, the density of GLUT3 channels was measured as 18pmol / mg cell membrane. We assume the cell membrane has a density of order 1g/cm^3 and forms a sheet of thickness 4nm. This allows us to calculate the area density of GLUT3 channels in cerebellar neurons as approximately $a = 43$ transporters/μm^2.

In the case where the difference in external and internal glucose concentration (ΔG) is below $K_{M,\text{glut3}}$, we can approximate the net flux into the cell as,

$$\text{flux} = k_{\text{glut3}} a \frac{\Delta G}{K_{M,\text{glut3}}} = P \Delta G, \tag{A.1}$$

allowing an estimate of the permeability $P = \frac{k_{\text{glut3}} a}{K_{M,\text{glut3}}} \approx 0.02 \mu\text{m/s}$

A.2 Effective Michaelis-Menten kinetics for glycosylation of Milton

We assume individual steps in glucose metabolism follow classic Michaelis-Menten kinetics, with the rate of product formation given by $dP/dt = v_i S/(K_{Mi} + S)$. We further assume that all pathways considered here are operating in steady-state, with a stationary concentration of all intermediates. When several Michaelis-Menten reactions are connected in series (*eg:* A $\rightarrow$ B $\rightarrow$ C), steady state requires that the dependence of final product formation C on the initial reactant A is given by,

$$\frac{dC}{dt} = \frac{v_{AB} A}{K_{AB} + A} \tag{A.2}$$

where v_{AB}, K_{AB} are the maximum rate and saturation constant for the initial A $\rightarrow$ B reaction.

If two pathways branch from a single intermediate, as occurs when the hexosamine biosynthetic pathway splits off first from the pentose phosphate pathway and then from glycolysis, then we have an additional reaction B $\rightarrow$ D that alters the rate of C formation. We make the key assumption that the saturation constants in the first step of both branching pathways are

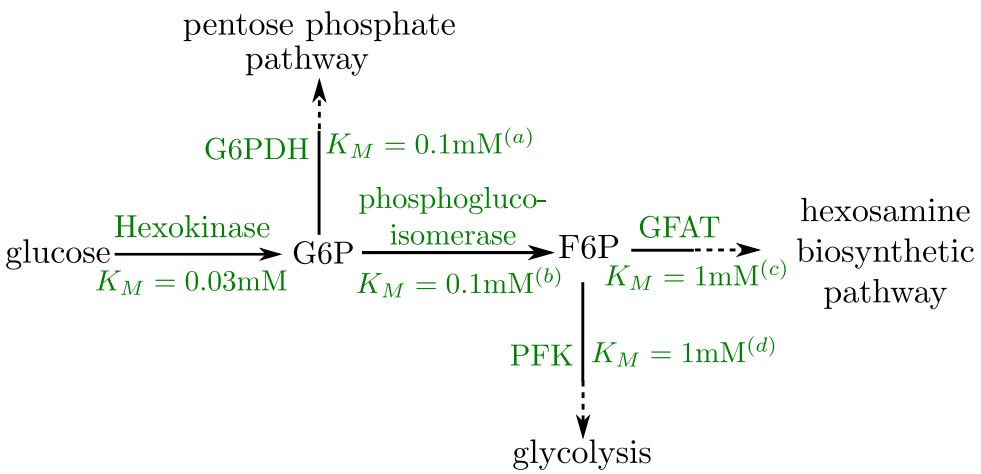

Figure A.1. Schematic of early pathway branches in glucose metabolism, showing the branching of the pentose phosphate pathway and glycolysis from the hexosamine biosynthetic pathway that leads to UDP-GlcNAc formation.
Saturation concentrations are labeled for each of the initial branching reactions. Note that in both cases, the splitting branches have comparable values of K_M.
$^{(a)}$ [47]; $^{(b)}$ [88]; $^{(c)}$ [110]; $^{(d)}$ [207]

comparable ($K_{BC} \approx K_{BD}$). Steady state then requires

$$\begin{aligned} \frac{v_{AB}A}{K_{AB}+A} &= \frac{(v_{BC}+v_{BD})B}{K_{BC}+B} \\ \frac{dC}{dt} &= \left(\frac{v_{BC}}{v_{BC}+v_{BD}}\right)\frac{v_{AB}A}{K_{AB}+A} \end{aligned} \tag{A.3}$$

Thus, if the saturation concentrations of the splitting reactions are similar, then the formation of the final product occurs at a rate proportional to the initial substrate consumption, with the same saturation constant. As illustrated in the pathway schematic (Appendix 2 Fig.A.1), the branching of both the pentose phosphate pathway and glycolysis from the pathway leading to UDP-GlcNAc formation involves similar values of the Michaelis-Menten constant. We therefore assume that the rate of Milton glycosylation by OGT (dC/dt) is proportional to the rate of initial glucose consumption by hexokinase ($|dA/dt|$). This assumption justifies our use of the same K_M for both glucose consumption and mitochondrial stopping. The fraction of metabolic flux funneled into Milton glycosylation is subsumed into the effective rate constant k_s.

A.3 Effect of domain length L in uniform permeability model

Dimensional analysis of Eq. 2.6 indicates that the diffusive term for glucose dynamics will be negligible compared to the consumption and entry terms in the limit $L \gg \sqrt{D(G+K_M)/(k_g\overline{M})}$. We assume that external glucose concentrations are well below 10mM, indicating that the diffusive term is irrelevant for $L \gg 150\mu$m. If diffusion is neglected, the only length units in the model are found within external glucose and mitochondrial concentrations, both of which are fixed parameters independent of axonal length. We therefore expect in this limit that the model results will not depend on the interval length L.

To verify the accuracy of this limit, we plot glucose and mitochondrial distributions for the full model (including diffusion) for interval lengths of $L = 100\mu$m, 1mm 1 cm (Appendix 3, Fig. A.2a,b). All other parameters are from our physiological estimates in Table(2.1). We note that for lengths well above 100μm, the distributions are independent of L and are nearly identical to those expected for the model with diffusion excluded. We also plot mitochondrial accumulation and metabolic enhancement in the distal 10% of the interval obtained from solutions of the full model with diffusive transport, which match well to the plots in the main text (Fig.2.6) that neglect diffusive transport. We can thus assume that glucose entry and turnover are much faster than diffusive spread for biologically relevant parameter regimes.

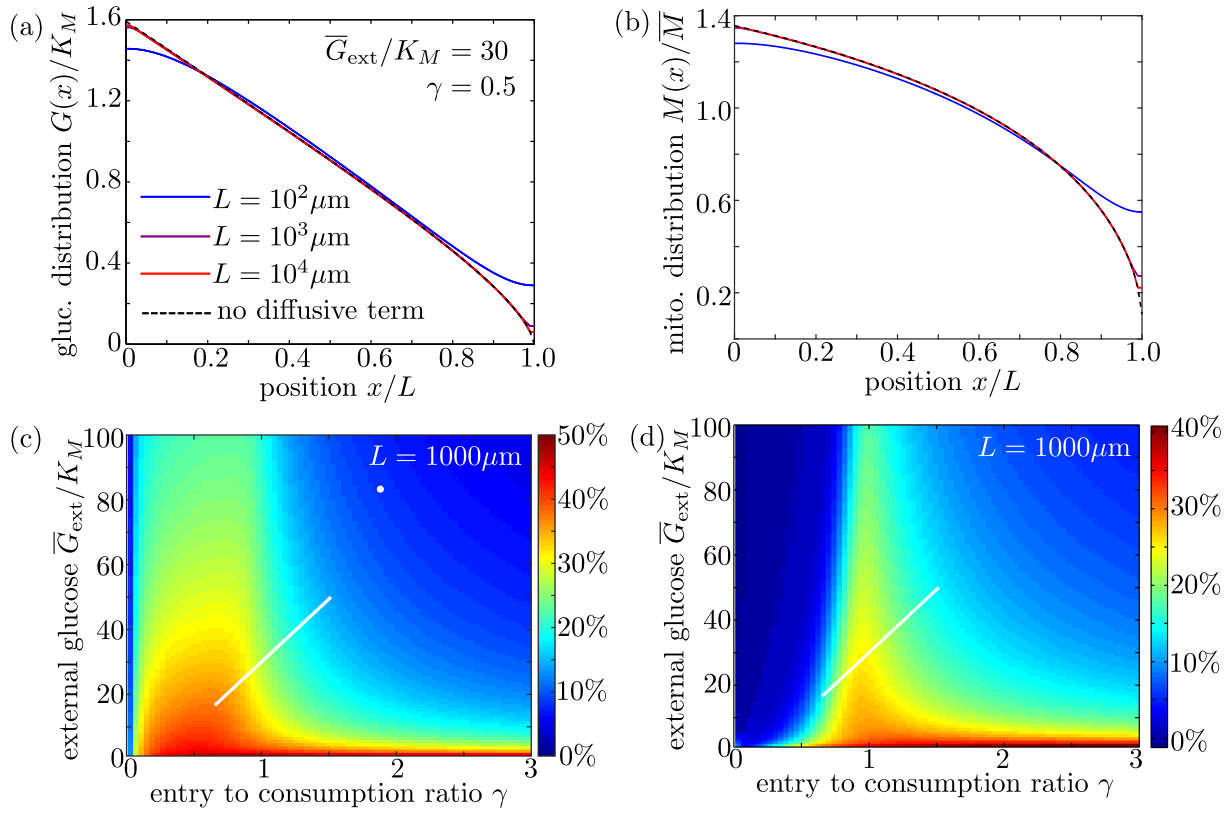

Figure A.2. Long cell length limit can be approximated by a simplified model without diffusive transport.
(a-b) Steady-state intracellular glucose and mitochondrial distributions from numerical solutions of Eq. 2.6 using different values of interval length L. Black dashed line shows solution of the simplified model with the diffusive term removed.(c) Mitochondrial enrichment in the distal 10% of the interval subject to highest external glucose, as compared to a uniform distribution. White line indicates physiological brain glucose levels, while white dot indicates glucose levels in cultured neurons [153]. (d) Enhancement in metabolic flux in the distal 10% of the interval, compared to uniform mitochondrial distribution. Plots (c) and (d) are obtained from solutions of the full model with diffusive transport and are indistinguishable from Fig. 2.6d-e for an interval length of 1000μm.

Appendix B

Appendix for Chapter 3

B.1 Generalization to Branched Axons

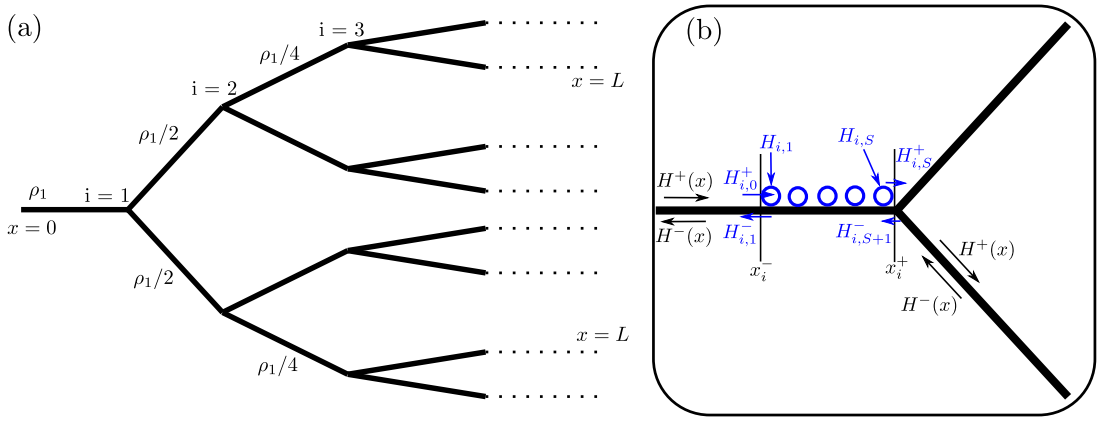

Figure B.1. Cartoon demonstrating demand sites in a branched tree and corresponding health parameters.
(a) Symmetric tree network used for branched axon calculations. Each segment branches into $g = 2$ identical downstream segments. The soma is at position $x = 0$ and distal tips at position $x = L$. (b) Zoomed-in schematic of a demand site at a branching junction. Demand site is located at position x_i, with $S = 5$ stationary mitochondria shown (blue). The health of the j^{th} mitochondrion is given by $H_{i,j}$, and the motile health leaving and entering on each side of the region is labeled. In our simplified model, the demand site is assumed to be infinitely narrow, and $x_i^{\pm}$ refers to the positions in the domain immediately after and before the demand site.

Throughout this work we focus on the interplay between mitochondrial transport, interchange, and aging, assuming a linear geometry to minimize the geometric complexity. However, *in vivo* axons have a tree-like branched structure, with mitochondrial localization observed at the branching points[135]. In this section we present a generalization of the 'Space Station' model

for a simple symmetric tree structure with stationary mitochondria localized at the branching points.

We assume that each branching junction splits into $g = 2$ identical downstream branches of equal length. The "demand sites" are placed immediately upstream of each branch point, with an equal number of mitochondria (S) situated at each site. The model geometry is sketched in Fig B.1. The symmetry of the system allows us to define a coordinate system $0 \leq x \leq L$, with 0 corresponding to the soma and L to the distal tips. The motile mitochondria health distribution $H_i^{\pm}(x)$ gives the health density at position x in any one of the corresponding branches. As before, we define $H_{i,j}$ to be the health of the j^{th} mitochondrion at demand site (junction) i. The quantity $H_{i,j}^{+}$ gives the anterograde-moving health density in the infinitesimally small space between mitochondrion j and $j+1$ at site i; similarly, $H_{i,j}^{-}$ gives the retrograde-moving health density between mitochondrion $j-1$ and j. With these definitions, the branched system obeys Equations 3.13 after replacing the general mitochondrial density ρ with a branch-dependent density ρ_i, defined by

$$\rho_1 = \frac{M - nS}{L}, \quad \rho_{i+1} = \rho_i / g. \tag{B.1a}$$

Here ρ_1 is the motile mitochondria density in the initial branch arising from the soma, and this density splits evenly at each junction point to give the downstream density ρ_i between junction $i-1$ and i.

In addition to Eq. 3.13,the boundary conditions that complete the branched system are:

$$H^{+}(x_i^{-}) = H_{i,0}^{+}, \quad H^{+}(x_i^{+}) = H_{i,S}^{+}/g \tag{B.2a}$$

$$H^{-}(x_i^{-}) = H_{i,1}^{-}, \quad H^{-}(x_i^{+}) = H_{i,S+1}^{-}/g \tag{B.2b}$$

Eq. B.2a indicates that the anterograde health density leaving each junction ($H_{i,S}^{+}$) splits into g

equal branches. Similarly, Eq. B.2b defines the retrograde density entering the junction ($H^{-}_{i,S+1}$) as the sum of retrograde densities from g branches.

The branched model with a tree of depth m has a total of $n = 2^m - 1$ demand sites, with each motile mitochondrion passing m of those sites on its way down the axon. When comparing to the linear model, we compare systems with the same total number of mitochondria M servicing the same number of demand sites n, and with the same distance L from soma to distal tip. It should be noted that the average linear density of motile mitochondria is lower in the branched model because the same total number M is spread out over a larger total branch length [$L_{\text{tot}} = (2^{(m+1)} - 1)L/(m+1)$]. The primary model parameters (decay rate $\widehat{k}_d$, fraction of stopped mitochondria f_s, and average number of stopping events for each protein N_s) are defined to be conceptually analogous to the linear model. As before, we have $\widehat{k}_d = k_d L/v$ and $f_s = nS/M$. Because each mitochondrion traverses only one branch at each level of the tree, the number of stopping events is given by $N_s = 2\widehat{p}_s m$.

The steady-state mitochondrial health at the demand sites in a tree of depth 4-level and 8-level tree are plotted in Fig B.2. The overall value of both average and distal mitochondrial health is somewhat decreased, presumably as a result of the lower density of motile mitochondria servicing the more distal branches. Interestingly, increasing the depth of the branching tree (while keeping a constant length L) only slightly lowers mitochondrial health, despite the fact that the distal density of motile mitochondria decreases exponentially. This result further confirms the observation that the primary relevant parameters are fraction of mitochondria stopped (f_s) and number of stopping events N_s rather than the absolute number of demand sites or density of motile mitochondria. Furthermore, we note that the optimal values of f_s and N_s are largely unchanged in the branched system when compared to the linear geometry (Fig. 3.5). We therefore conclude that our main results, which rely on a linear axonal geometry, are more generally applicable.

A number of questions remain regarding mitochondrial maintenance in a branching geometry. Namely, the potential effect of redistributing stationary mitochondria at different depths along the tree, the consequences of asymmetric tree geometries, the effect of bidirectional

motion into multiple branches, and the role of autophagy in tree-like structures, may further elucidate the optimal strategies for mitostasis in realistic axonal geometries. These more in-depth explorations serve as a promising jumping-off point for future expansion of the model described in this manuscript.

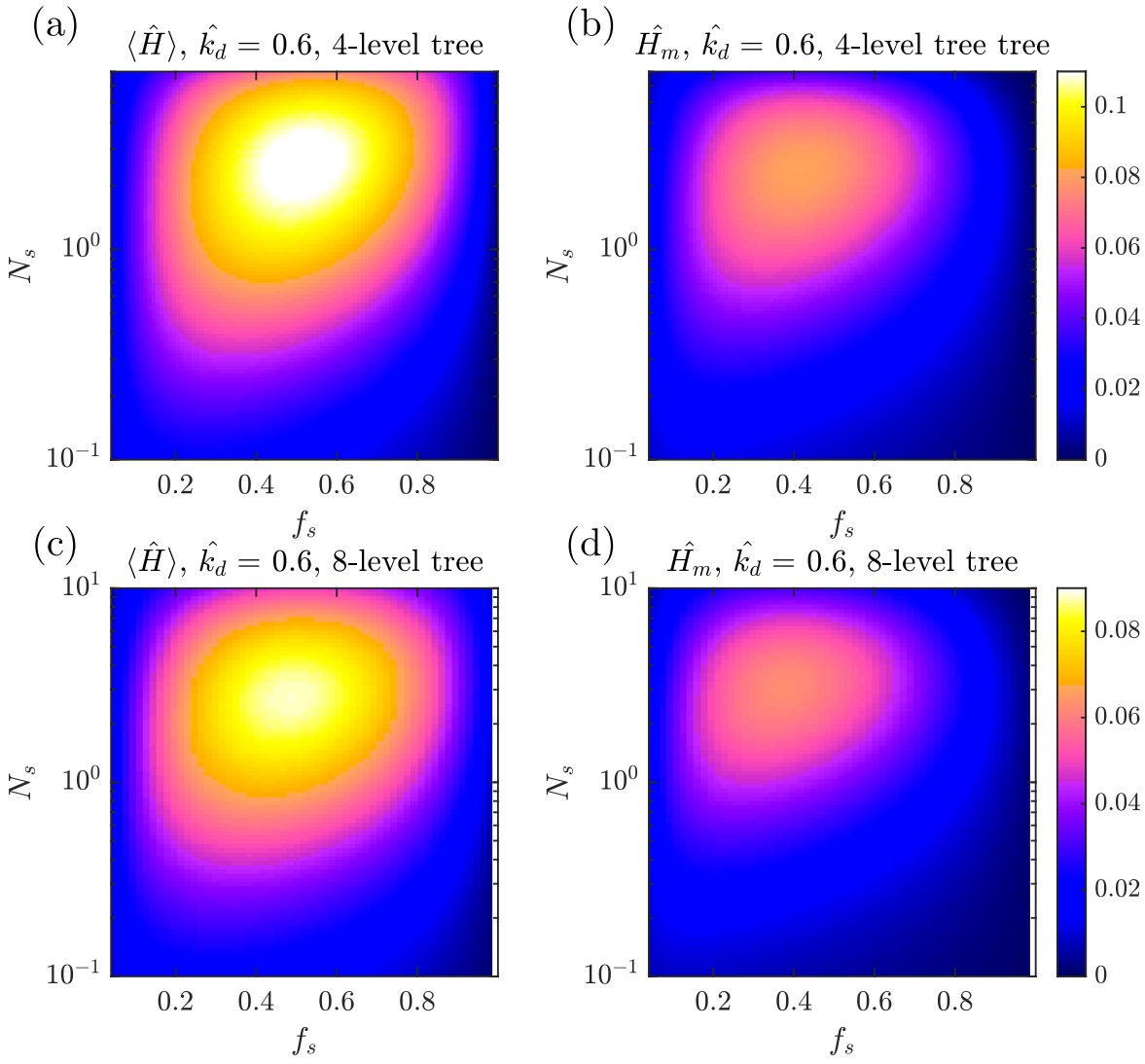

Figure B.2. Mitochondrial health for expanded model in a symmetric branched tree geometry. (a) Average mitochondrial health as a function of f_s and N_s for a tree of depth $m = 4$, with $n = 15$ demand sites at the branch junctions. (b) Corresponding plot for the health of each distal demand site (furthest from the soma). (c-d) Corresponding plots for a tree of depth $m = 8$, with 255 demand sites.

B.2 Contribution of retrograde fusion events

Both the SS and CoG models allow health components to transition from a motile to a stationary state in an unbiased fashion. This means mitochonria moving in both the anterograde and retrograde directions are able to stop at demand sites (CoG model) or fuse with stationary mitochondria (SS) model with equivalent stopping or fusion probabilities. Because retrograde-moving mitochondria tend to have lower health levels compared to anterograde-moving mitochondria, removing fusion events between retrograde-moving mitochondria and stationed mitochondria is expected to result in higher health levels at demand sites. Such a modification would be equivalent to mitophagy that is triggered not by mitochondrial health levels but rather by the arrival of mitochondria at the distal terminus.

The 'Space Station' model equations can be modified as follows to reflect a potential regulatory mechanism that completely prohibits fusion of retrograde-moving mitochondria:

$$\frac{dH^{\pm}}{dt} = \mp v\frac{\partial H^{\pm}}{\partial x} - k_d H^{\pm} \tag{B.3a}$$

$$\frac{dH_{i,j}}{dt} = \frac{vp_f}{2}\left[H^{+}_{i,j-1}\right] - \left[\frac{v\rho p_f}{4} + k_d\right] H_{i,j} \tag{B.3b}$$

$$H^{+}_{i,j} = H^{+}_{i,j-1}\left(1 - \frac{p_f}{2}\right) + \frac{\rho p_f}{4} H_{i,j}, \quad H^{-}(x_{i,j}) = H^{-}_{i,j+1} \tag{B.3c}$$

$$H^{+}(L) = H^{-}(L) \tag{B.3d}$$

$$vH^{+}(0) = k_p. \tag{B.3e}$$

In Eq. B.3b, the quantity $\rho/2$ gives the density of anterograde-moving mitochondria, replacing ρ in the original 'Space Station' equation (Eq. 3.13b).

The steady-state mitochondrial health in the absence of retrograde fusion is plotted in Fig B.3. We see that removing fusion with retrograde mitochondria means that there is no longer an optimum in the number of interaction events between motile and stationary mitochondria.

The disadvantage to high N_s in the original model arose from the fusion of unhealthy retrograde mitochondria picking up proteins from stationary organelles and carrying them prematurely back to the soma for recycling. This disadvantage is no longer present if retrograde mitochondria are incapable of fusion.

Removal of retrograde fusion also results in a 50% increase in average health at demand sites (Fig B.3a), again by preventing fusion of the less healthy retrograde mitochondria with stationary organelles at the proximal sites. Interestingly, the maximum health at the most distal site remains largely unchanged (Fig B.3b).

These results indicate that any cellular mechanism capable of biasing exchange events between the motile and stationary population so that retrograde mitochondria were less likely to fuse or stop could be beneficial for enhancing mitochondrial health in the domain.

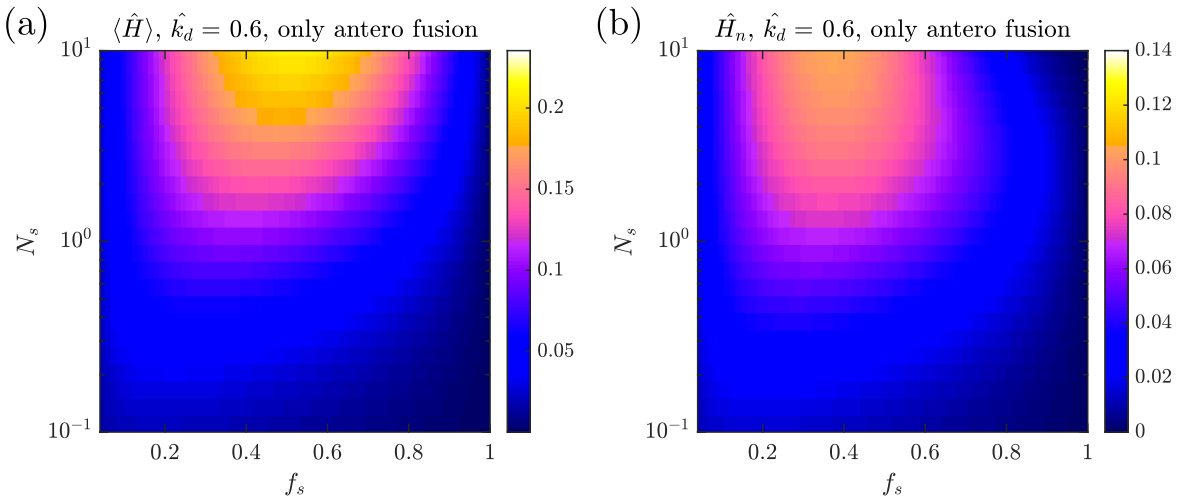

Figure B.3. Mitochondrial health without retrograde fusion; plots analogous to Fig. 3.5. (a) Average health across all demand regions as a function of fraction of stopped mitochondria (f_s) and number of stopping events (N_s), for high decay rate ($\widehat{k_d} = 0.6$). (b) Corresponding mitochondrial health at the most distal demand site.

Appendix C

Appendix for Chapter 4

Supplemental Methods S1: Mean-field models for mitochondrial distributions in a dendritic tree

C.0.1 Comparing average subtree densities in models with uniform transport

We first consider models where the mitochondrial transport parameters are spatially uniform (constant velocity v and stopping rate k_s throughout the arbor). Steady state linear densities of motile mitochondria (ρ_i^w) and stationary mitochondria (ρ_i^s) were computed as described in Methods.

Volume densities in arbors obeying Da Vinci parent-daughter scaling

We consider the case of a tree obeying Da Vinci scaling ($\alpha = 2$) between the parent branch width (r_0) and daughter branch widths (r_1, r_2), which are related according to $r_0^2 = r_1^2 + r_2^2$. We can solve for the linear densities in the daughter branch as follows:

$$\rho_i = \rho_0 \left(\frac{r_i^2}{r_1^2 + r_2^2} \right) = \rho_0 \frac{r_i^2}{r_0^2}, \quad \text{for } i = 1, 2, \tag{C.1}$$

where the relationship holds for both the motile and stationary mitochondria densities. The total volume density of mitochondria in a daughter branch i is then

$$c_i = \frac{\rho_i^w + \rho_i^s}{r_i^2} = \frac{\rho_0^w + \rho_0^s}{r_0^2} = c_0 \tag{C.2}$$

Thus, for the simplest model with uniform mitochondrial transport and conservation of cross-sectional area at each junction (Da Vinci rule), the volume density of mitochondria must be constant throughout the whole tree.

Volume densities in arbors obeying Rall's Law parent-daughter scaling

Alternately, we can compute the mitochondrial volume density in arbors that obey the Rall's Law relationship between parent and daughter branches (Rule 3, $r_0^\alpha = r_1^\alpha + r_s^\alpha$, with $\alpha = 3/2$). The assumptions of uniform mitochondrial transport (Rule 1 with $\beta = 0$) and mitochondria splitting in proportion to daughter branch area (Rule 2) are still maintained. Here we show that such a model leads to increased mitochonrial densities with distance from the soma, and unequal average densities in asymmetric sister subtrees. The relationships below apply to both motile and stationary mitochondrial densities.

We begin by focusing on a single junction with a parent trunk of radius r_0 and linear mitochondrial density ρ_0, and daughter trunk radii r_1, r_2 and linear densities ρ_1, ρ_2. A single parameter $\mu_0 = r_1^\alpha / r_0^\alpha$ describes how the dendritic width is split between sister branches (Rule 4), within the constraints of Rall's law. The fraction of mitochondria that enter the first daughter branch is $\rho_1/\rho_0 = r_1^2/(r_1^2 + r_2^2)$.

The ratio of mitochondrial volume density between the daughter branches and the parent can be written as

$$\frac{c_1}{c_0} = \frac{c_2}{c_0} = \frac{r_0^2}{r_1^2 + r_2^2} = \frac{1}{\mu_0^{2/\alpha} + (1-\mu_0)^{2/\alpha}} \tag{C.3}$$

For $\alpha < 2$, this ratio is always above unity ($c_1/c_0 > 1$), except in the edge cases of $\mu_0 = 0$ or $\mu_0 = 1$, which would correspond to one daughter branch disappearing. Thus, the volume density of mitochondria in the daughter branches of a Rall's Law tree is always higher than in the parent branch. This is a direct consequence of the reduced cross-sectional area in the daughter branches.

We next consider whether it is possible to choose values of the sister trunk splitting μ_i at each junction i in such a way as to ensure equitable mitochondrial distribution in the two sister subtrees. We begin by defining two parameters for a subtree initiating from trunk 0. First, the total volume of the subtree is expressed as $V_0 = \eta_0 r_0^2$. For a symmetric Da Vinci tree, where total cross-sectional area is conserved at each junction, the parameter η_0 represents the depth of the tree (distance from soma to distal tips). For a symmetric Rall's Law tree, however, the value of η_0 is less than the depth, due to the narrowing of total cross-sectional area below each junction. Second, we define a parameter z_0 relating the average volume density of mitochondria within the subtree, relative to the density within the trunk: $\langle c \rangle_0 = z_0 \rho_0 / r_0^2$. For a Da Vinci tree, under the assumption of uniform mitochondrial transport, $z = 1$ for all junctions regardless of the tree morphology. For a Rall's law tree with at least one junction, the increase in density from parent to daughter branches implies that $z_0 > 1$.

For two sister subtrees, the volume densities in the trunk must be the same ($\rho_1/\rho_2 = r_1^2/r_2^2$, from Rule 1, and therefore $c_1/c_2 = 1$). Consequently, the subtrees will have equal average mitochondrial densities if and only if $z_1 = z_2$. If we want to establish a universal rule for splitting sister trunks (ie: definining μ_i values at each junction) that depends only on the morphology of the downstream subtree, then the only way to ensure equitable mitochondrial densities throughout a sister subtrees in the arbor would be for all values of z_i to be set to a single constant $z_i = z^*$. For a Rall's Law arbor, we would need to pick a value $z^* > 1$ when setting such a rule. In this case, any subtree consisting of a single long branch (no downstream junctions) would automatically have $z_i = 1$ and would have a lower mitochondrial density than its sister. Furthermore, we show below that if z^* is set close to 1, then the required splitting of branch widths results in most of

the tree disappearing and one very long sequence of daughter branches receiving most of the cross-sectional area (Supplemental Figure C.2F). Such an extreme rebalancing of branch widths is clearly not representative of tree structure observed *in vivo* and corresponds to an edge case where the arbor is reduced primarily to a single tube rather than a tree. On the other hand, if we set z^* substantially higher than 1, then for many of the junction points it becomes impossible to solve for any value of μ that would enable equal mitochondrial densities in the sister subtrees.

The two parameters describing the volume and average mitochondrial density in a subtree, can be expressed recursively:

$$\eta_0 = \ell_0 + \eta_1 \mu_0^{2/\alpha} + \eta_2 (1-\mu_0)^{2/\alpha}, \tag{C.4a}$$

$$z_0 = \frac{\ell_0 + \frac{z_1 \mu_0^{2/\alpha} + z_2 (1-\mu_0)^{2/\alpha}}{\mu_0^{2/\alpha} + (1-\mu_0)^{2/\alpha}}}{\ell_0 + \eta_1 \mu_0^{2/\alpha} + \eta_2 (1-\mu_0)^{2/\alpha}}, \tag{C.4b}$$

where η_0, z_0 are the values for a tree with parent trunk 0 and $\eta_{1,2}, z_{1,2}$ are values for the daughter subtrees with trunks 1 and 2.

In Supplemental Figure C.2F we consider an example arbor morphology, where the junction connectivities and branch lengths are extracted from a *Drosophila* HS arbor skeleton. Starting from the distal branches of the tree, we recursively solve, where possible, for the value of μ_i at each junction that would set $z_i = z^*$ for the parent trunk leading to that junction. Where a solution is impossible (always due to the maximum value of z_i being below z^*), we pick the splitting that maximizes z_i. Red circles in the figure show junctions where a solution was not found that could enable the two sister subtrees to have equal mitochondrial densities. We see that choosing a high value of z^* makes it impossible to enforce equitable mitochondrial densities in many pairs of sister subtrees, in contrast to experimental observations. On the other hand, choosing $z^* \approx 1$ leads to an unrealistic collapse of the arbor to a single primary path in order to maintain equitable mitochondrial distribution.

Overall, these calculations imply that a Rall's tree morphology, together with uniform

mitochondrial transport kinetics, leads to increased mitochondrial densities in distal branches but cannot allow for a realistic splitting of branch widths that establishes equal mitochondrial densities between sister subtrees.

C.0.2 Subtree densities in a Da-Vinci tree with $k_s \sim 1/r^2$

Rather than assuming spatially constant mitochondrial motility, an alternative model can be constructed where mitochondria are more likely to halt on narrower branches, while the restarting rate k_w and pause-free velocities v remain constant. One simple model for width-dependent stopping would be to set the rate inversely proportional to the cross-sectional area of each branch: $k_{s,i} = k_s^*/r_i^2$, corresponding to $\beta = 2$ in scaling Rule 3. We then consider the distribution of stopped mitochondria in different dendritic branches. With $k_s \sim 1/r^2$, the linear density of stationary mitochondria in branch i is given by

$$\rho_i^{(s)} = \frac{k_s^*}{k_w}\rho_i^{(w)}/r_i^2 \tag{C.5}$$

Where $\rho_i^{(w)} = \rho_{+,i} + \rho_{-,i}$ is the motile linear density of mitochondria. At a junction with daughter branches $1,2$, this motile linear density splits according to $\frac{\rho_1^{(w)}}{\rho_2^{(w)}} = \frac{r_1^2}{r_2^2}$.

Comparing average densities in sister subtrees

In a tree with Da Vinci scaling, the volume density of motile mitochondria is spatially constant, so that all branches have $c_i^{(w)} = c_{\text{trunk}}^{(w)} = \rho_{\text{trunk}}^{(w)}/r_{\text{trunk}}^2$. We can then calculate the average volume density of the stationary population in a subtree with total volume V_{ST} and total branch length L_{ST}:

$$\left\langle c^{(s)} \right\rangle_{\text{ST}} = \frac{\sum_{i\in ST}\rho_i^{(s)}\ell_i}{\sum_{i\in ST} r_i^2\ell_i} = \frac{\frac{k_s^*}{k_w}c_{\text{trunk}}^{(w)}\sum_i \ell_i}{V_{ST}} \sim \frac{L_{ST}}{V_{ST}}, \tag{C.6}$$

where the summations are over all branches in the subtree.

Therefore, the ratio between the average stopped mitochondrial densities in sister subtrees becomes:

$$\frac{\left\langle c^{(s)} \right\rangle_1}{\left\langle c^{(s)} \right\rangle_2} = \frac{L_1/V_1}{L_2/V_2} \tag{C.7}$$

Keeping in mind that $\langle c \rangle = \left\langle c^{(w)} \right\rangle + \left\langle c^{(s)} \right\rangle$ and that $c^{(w)}$ is the same for all branches in a Da Vinci tree, we see that equitable distribution of mitochondria between sister subtrees can be achieved only if the volume of each sister subtree is proportional to its total length:

$$\frac{L_1}{V_1} = \frac{L_2}{V_2}. \tag{C.8}$$

Notably, increased stopping of mitochondria in narrower branches implies that more distal sections of the dendritic tree will tend to have higher mitochondrial densities. We therefore predict that the combination of Da Vinci scaling of branch widths ($r_0^2 = r_1^2 + r_2^2$) together the the proportionality of subtree length and total volume (Eq. C.8) will give rise to mitochondrial densities that both increase with distance from the soma and are equal between sister subtrees, as observed for experimental data.

Sister branch radii splitting for $L \sim V$ relationship

For a Da Vinci arbor, the proportional relationship between sister subtree length and volume (Eq. C.8) can be achieved via a particular morphological rule governing the relative trunk widths of sister substrees emerging from the same junction (Rule 4).

We begin by defining the depth of a tree (D) via a recursive approach. For a subtree consisting of a single branch of length ℓ_1, the depth is simply defined as that branch length ($D_1 = \ell_1$). Next, we consider a tree with trunk of index 0, splitting at a downstream junction between subtree trunks 1 and 2. We define the depth of the tree according to the following

formula:

$$D_0 = \ell_0 + \frac{L_1 + L_2}{L_1/D_1 + L_2/D_2}, \tag{C.9}$$

where D_1, D_2 are the depths and L_1, L_2 are the total branch lengths of the subtrees starting with branch 1 and 2, respectively. Conceptually, this expression averages the inverse depths of the two subtrees, weighted by their respective lengths, and adds on the length of the parent trunk. We note that in the case where the two subtrees have the same depth ($D_1 = D_2$) then the overall depth of the tree becomes $D_0 = \ell_0 + D_1$. Thus, in an arbor where all distal tips are the same distance from the parent node, the depth of the tree will simply be equal to that distance.

We now consider the specific case of a Da Vinci arbor that additionally obeys the criterion in Eq. C.8, where the volume of a sister subtree is proportional to its total length. As before, we express the volume of the arbor in terms of the prefactor η_0 according to $V = \eta_0 r_0^2$. We then show by induction that under these assumptions the prefactor is equal to the depth: $D_0 = \eta_0$. First, we use the length-volume proportionality to express the volume of each subtree in terms of the parent volume and the subtree lengths according to:

$$\begin{aligned} V_0 &= \ell_0 r_0^2 + V_1 + V_2, \\ V_i &= \frac{L_i}{L_1 + L_2}(V_1 + V_2) = \frac{L_i}{L_1 + L_2}\left(V_0 - \ell_0 r_0^2\right) = \eta_i r_i^2, \quad i = 1, 2 \end{aligned} \tag{C.10}$$

Next, we can apply the Da Vinci law relating parent and daugher branch widths:

$$\begin{aligned} r_0^2 = r_1^2 + r_2^2 &= \frac{L_1/\eta_1 + L_2/\eta_2}{L_1 + L_2}\left(V_0 - \ell_0 r_0^2\right), \\ V_0 &= \left(\ell_0 + \frac{L_1 + L_2}{L_1/\eta_1 + L_2/\eta_2}\right) r_0^2 = \eta_0 r_0^2 \end{aligned} \tag{C.11}$$

Thus, we see that if the two subtrees have depths $D_1 = \eta_1$ and $D_2 = \eta_2$, then the overall tree will also have $D_0 = \eta_0$, where depth is defined according to Eq. C.9. Since single branches have $\eta_i = D_i$ by definition, this argument implies that all trees obeying Da Vinci scaling and

length-volume proportionality, have volume given by $V_0 = D_0 r_0^2$.

Finally, we note that, for a Da Vinci tree, the proportionally of length and volume can now be translated directly into a relationship between sister subtree trunk widths:

$$\begin{aligned} \frac{L_1/V_1}{L_2/V_2} &= \frac{L_1/(D_1 r_1^2)}{L_2/(D_2 r_2^2)} = 1, \\ \frac{r_1^2}{r_2^2} &= \frac{L_1/D_1}{L_2/D_2} = \frac{b_1}{b_2} \end{aligned} \tag{C.12}$$

where we define the 'bushiness' of a subtree (b_i) as its total length divided by its depth: $b_i = L_i/D_i$. Trees with high bushiness are broader, in the sense of having a greater total length of branches at a given depth, arising from more frequent junctions (Figure 4b).

Overall, we have shown that in an arbor obeying the Da Vinci rule ($\alpha = 2$), where mitochondrial stopping is inversely proportional to branch area ($\beta = 2$), equal densities of mitochondria between sister subtrees will be obtained if the sister trunk areas are split in proportion to the subtree bushiness (Eq. C.12).

C.0.3 Average subtree densities for general transport behavior in Da Vinci arbors

We next consider a generalization of the mitochondrial distribution model to the case where both the stopping rate $k_{s,i}$ and the pause-free velocity v_i can vary depending on the branch width. At steady state, the conservation of incoming and outgoing flux into a branch junction gives a relationship between the motile mitochondria density $\rho_0^{(w)}$ in the parent trunk 0 and the daughter branches $1, 2$. We maintain the assumption that the splitting of mitochondrial flux into each daughter branch is proportional to the cross-sectional area. Specifically, this gives the two

conditions:

$$v_o \rho_o^{(w)} = v_1 \rho_1^{(w)} + v_2 \rho_2^{(w)} \tag{C.13a}$$

$$\frac{v_1 \rho_1^{(w)}}{v_2 \rho_2^{(w)}} = \frac{r_1^2}{r_2^2}. \tag{C.13b}$$

The density of stationary mitochondria in each branch is given by $\rho_i^{(s)} = \frac{k_{s,i}}{k_w} \rho_i^{(w)}$.

Assuming a Da Vinci relationship between parent and daughter branch widths, we can solve for the volume density of mitochondria in daughter branches as follows:

$$\begin{aligned} v_0 \rho_0^{(w)} &= v_1 \rho_1^{(w)} \left(1 + \frac{r_2^2}{r_1^2}\right) = \frac{v_1 \rho_1^{(w)} r_0^2}{r_1^2} \\ c_1^{(w)} &= \rho_1 / r_1^2 = c_0^{(w)} \frac{v_0}{v_1}. \end{aligned} \tag{C.14}$$

Consequently, throughout the entire arbor, the motile volume density in each branch can be written in terms of the local velocity and the density in the parent trunk of the full tree: $c_i^{(w)} = c_{\text{trunk}}^{(w)} \frac{v_{\text{trunk}}}{v_i}$. The total volume density on a branch, including motile and stationary mitochondria, can be expressed in terms of the average velocity (with pauses included), given by $\overline{v}_i = \frac{k_w}{k_w + k_{s,i}} v_i$. Specifically:

$$c_i = c_i^{(w)} + c_i^{(s)} = \left(\frac{k_{s,i} + k_w}{k_w}\right) c_{\text{trunk}}^{(w)} \frac{v_{\text{trunk}}}{v_i} = c_{\text{trunk}}^{(w)} v_{\text{trunk}} / \overline{v}_i \tag{C.15}$$

The average volume density of mitochondria in a subtree is then given by

$$\langle c \rangle_{\text{ST}} = \frac{\sum_{i \in \text{ST}} c_i^{(w)} r_i^2 \ell_i}{\sum_{i \in \text{ST}} r_i^2 \ell_i} = \frac{1}{V_{\text{ST}}} \sum_{i \in \text{ST}} \frac{r_i^2 \ell_i c_{\text{trunk}}^{(w)} v_{\text{trunk}}}{\overline{v}_i} = c_{\text{trunk}}^{(w)} v_{\text{trunk}} \left\langle \frac{1}{\overline{v}} \right\rangle_V, \tag{C.16}$$

where the final term denotes the volume-weighted average of the inverse velocity over the subtree: $\left\langle \frac{1}{\overline{v}} \right\rangle_V = \left(\sum_{i \in \text{ST}} r_i^2 \ell_i (1/\overline{v}_i)\right) / V_{\text{ST}}$.

We consider the case where the average velocity (including pauses) along a branch scales

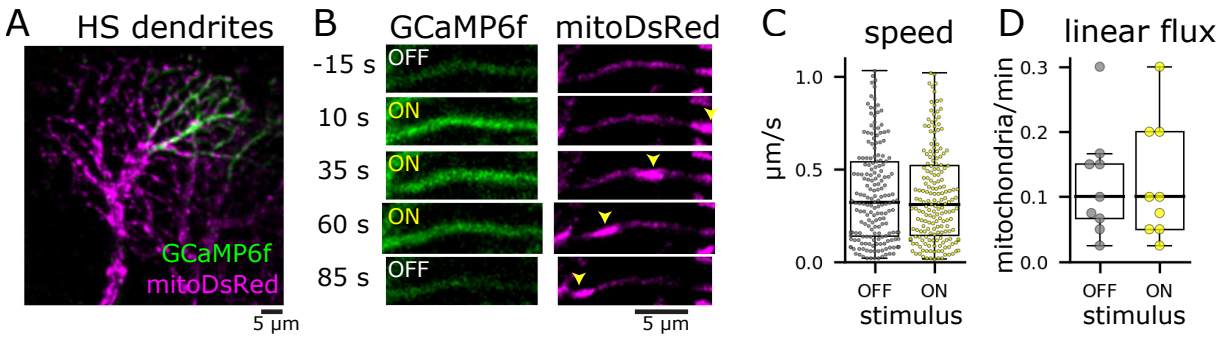

Figure C.1. Stimulus-evoked calcium signals do not affect mitochondrial motility in HS dendrites. Figure courtesy of Barnhart Lab, Columbia University.
A: HS dendrites, labeled with mitoDsRed (magenta) and GCaMP6f (green), imaged while a visual stimulus drove calcium signals in distal HS dendrites. B: Calcium responses to the motion stimulus (GCaMP6f, left) and mitochondria (mitoDsRed, right) in an HS dendritic branch. Yellow arrows indicate a moving mitochondrion. C-D: Mitochondrial speeds (C) and linear flux rates (D) when the visual stimulus was OFF versus ON. Dots indicate instantaneous speeds or average linear fluxes for individual flies.

as a power law of the branch width: $\bar{v}_i \sim r_i^{\gamma}$. Under this assumption, the ratio of sister subtree densities is given by

$$\frac{\langle c \rangle_1}{\langle c \rangle_2} = \frac{\left\langle \frac{1}{\bar{v}} \right\rangle_{V_1}}{\left\langle \frac{1}{\bar{v}} \right\rangle_{V_2}} = \frac{V_2}{V_1} \frac{\sum_{i \in \mathrm{ST}_1} r_i^{2-\gamma} \ell_i}{\sum_{i \in \mathrm{ST}_2} r_i^{2-\gamma} \ell_i}. \tag{C.17}$$

In the case that $\gamma = 2$, this relationship reduces to $\langle c \rangle_1 / \langle c \rangle_2 = (L_1/V_1)/(L_2/V_2)$, and equal densities of mitochondria between sister subtrees are again achieved when the subtree volume is proportional to its total length. A particular case that leads to $\gamma = 2$ is where restarting rates are low ($k_{s,i} \gg k_w$ throughout most of the tree), pause-free velocities are constant, and the stopping rate scales inversely with cross-sectional area ($k_{s,i} \sim 1/r_i^2$). This is the simplified case considered in the main text.

C.0.4 Supplemental Figures

Figure C.2. Model mitochondrial distributions in synthetic dendritic trees.
A: Representative examples of synthetic trees with random (four left images) or symmetric (right) topologies. B-E: Model results. Mitochondrial density asymmetry across sister subtrees (B,C) and distal mitochondrial enrichment (D,E) were calculated for $\beta = 0$ (B,D) or $\beta = 2$ (C,E), $\alpha = 2$ (cyan), 3/2 (red), or 3 (purple), and sister subtree scaling with subtree trunks splitting according to $r_1 = r_2$ (eq.), $r^2 \sim L$, or $r^2 \sim L/D$. N = 19 synthetic arbors (circles) and 1 symmetric arbor (stars). F: HS dendrites with radii that obey Rall's parent-daughter scaling ($\alpha = 3/2$); $\beta = 0$. The parameter z* determines the ratio of sister subtree trunk thickness (r_1 and r_2) at each branch point (see Appendix). Red circles indicate branch points for which there is no solution for equal sister subtree densities. For high values of z* (left), there are many junctions with no solution. As z* approaches 1 (right), there are fewer junctions with no solution. However, arbor morphologies become unrealistic, with many thin dendrites branching from a single thick branch.

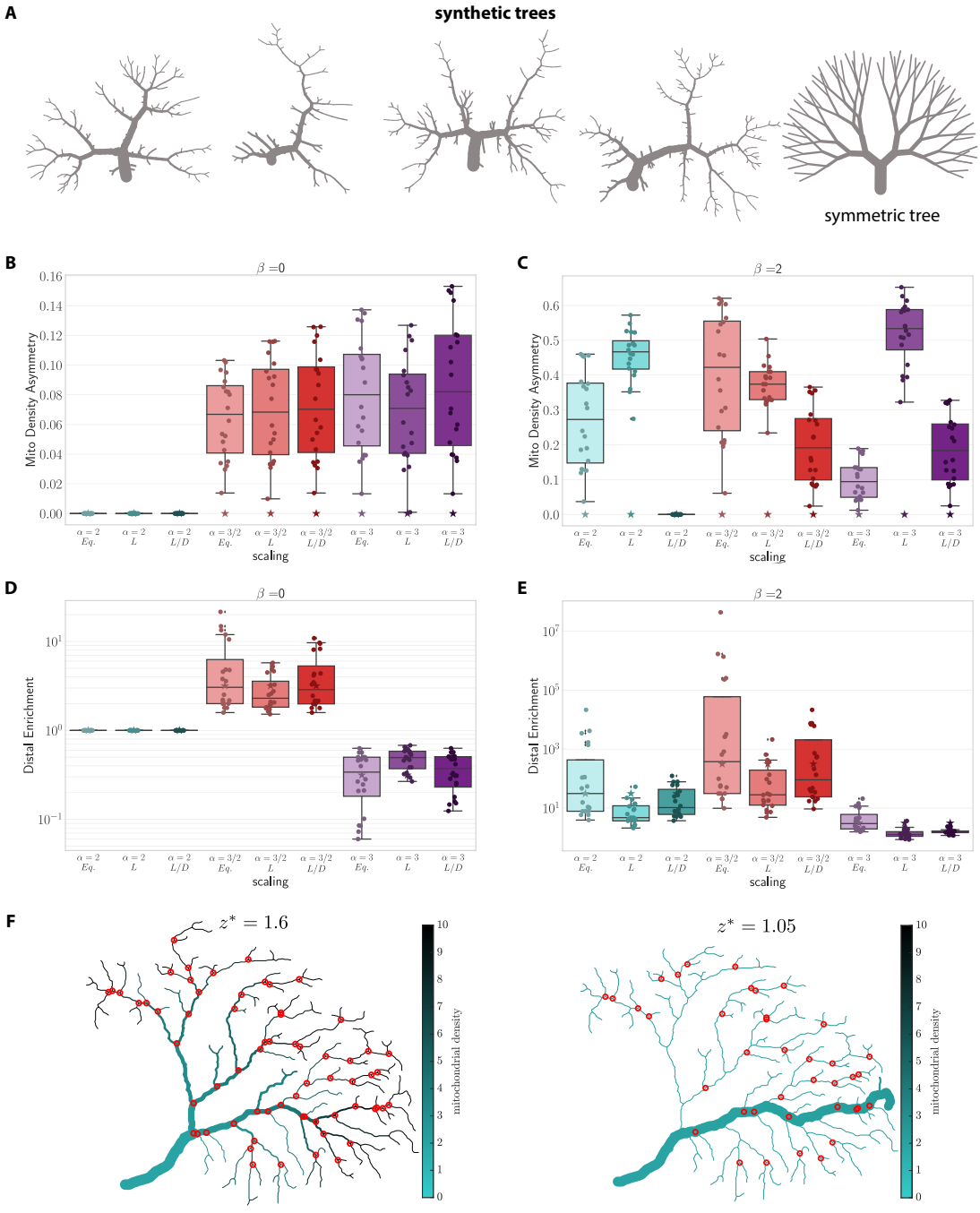
A
synthetic trees
symmetric tree
B
$\beta = 0$
Mito Density Asymmetry
scaling
C
$\beta = 2$
Mito Density Asymmetry
scaling
D
$\beta = 0$
Distal Enrichment
scaling
E
$\beta = 2$
Distal Enrichment
scaling
F
$z^* = 1.6$
$z^* = 1.05$
mitochondrial density

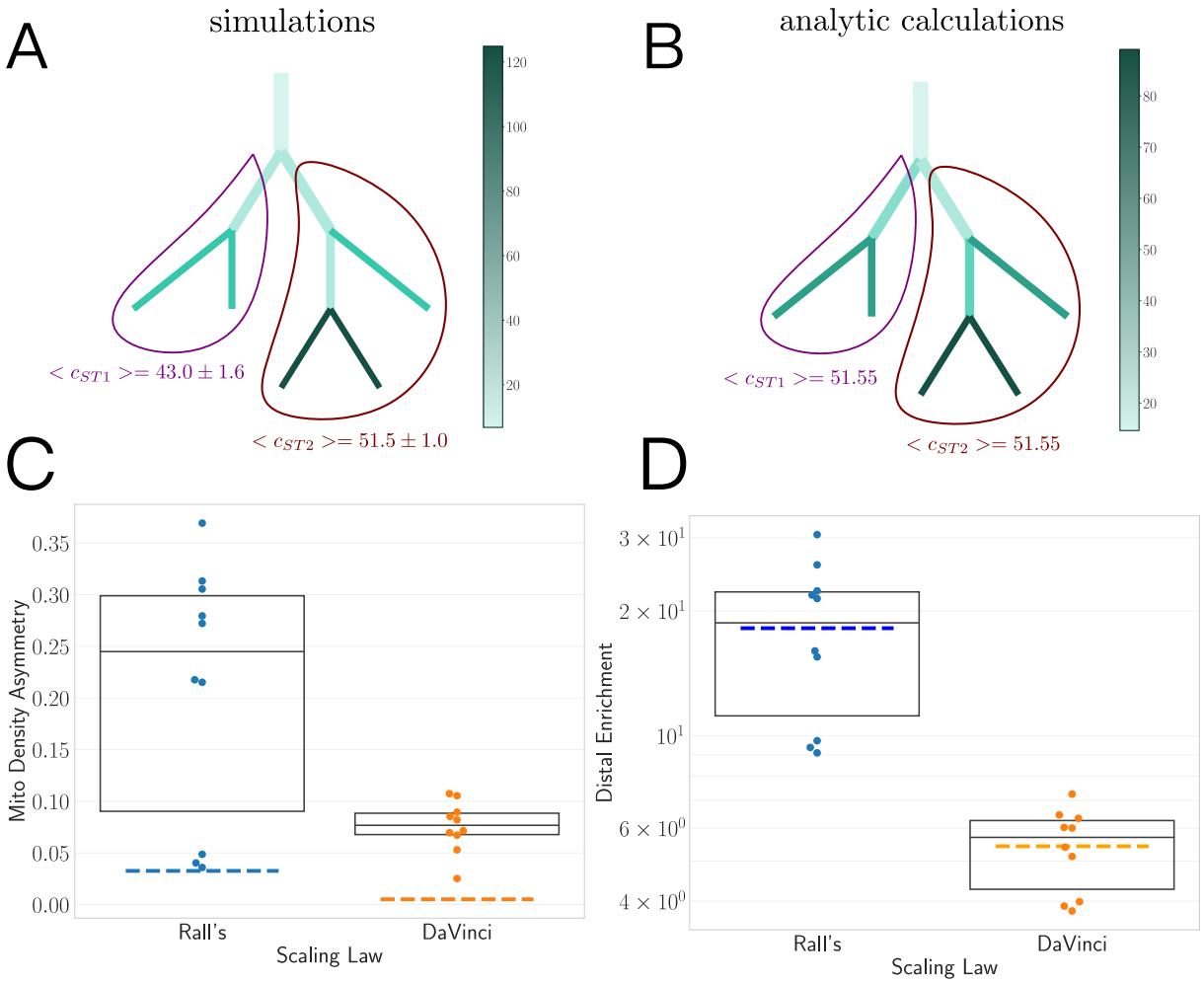

Figure C.3. Numerical simulations of mitochondrial distributions.
A: Simulated mitochondrial densities in a small synthetic arbor scaled according to Da Vinci's rule ($\alpha = 2$), sister subtree splitting with $L \sim V$, and transport scaling with $\beta = 2$. Total mitochondrial densities in the two largest subtrees ($\langle c_{ST1} \rangle$ and $\langle c_{ST2} \rangle$) are indicated on the plot. B: Analytical calculations of mitochondrial densities for the same arbor as in A. Note that whereas mitochondria are equitably distributed across ST1 and ST2 in the analytical solution, stochastic effects result in asymmetry in the simulated results. C-D: Mitochondrial densities were simulated for 10 synthetic arbors, and mitochondrial density asymmetry (C) and distal enrichment (D) were measured for two parent-daughter scaling rules: Rall's law ($\alpha = 3/2$) and Da Vinci's rule ($\alpha = 2$). Sister subtrees split with $L \sim V$, and transport scaled with $\beta = 2$. Box plots indicate the mean and interquartile range for simulation results; dashed lines indicate average values for numerical solutions for the same arbors.

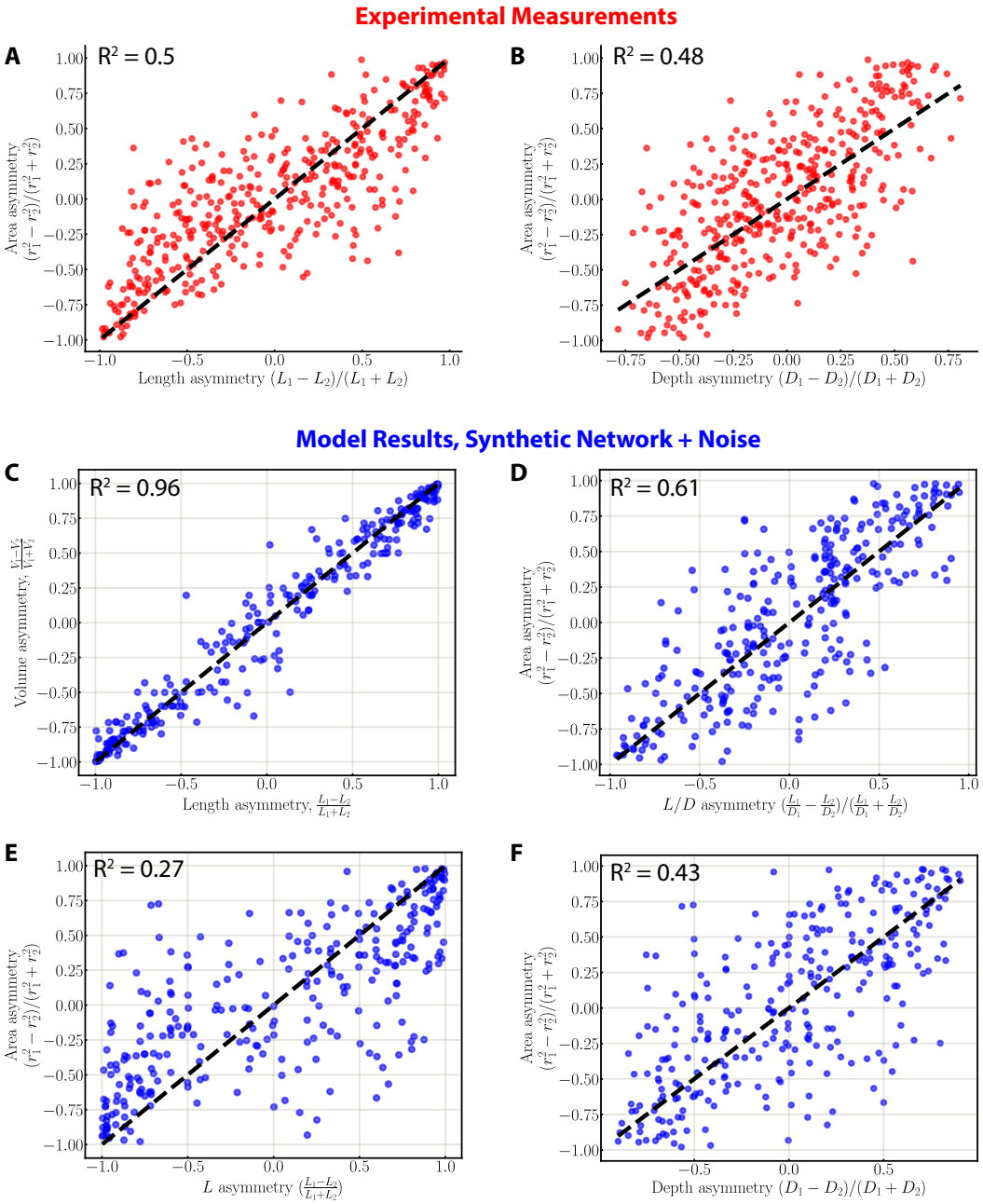

Figure C.4. HS dendrites do not obey sister subtree scaling with $r^2 \sim$ subtree length or depth
A-B: Measurements of HS dendrites sister subtree asymmetries (N = 649 branch points from 10 HS dendrites). Trunk thickness (r^2) asymmetry is more weakly correlated with length (A) or depth (B) asymmetry than with bushiness asymmetry (Figure 4.4). C-F: Sister subtreecorrelations in a synthetic tree. Branch radii were set according to parent-daughter scaling with $\alpha = 2$ and sister subtree scaling with $L \sim V$, plus a gaussian noise term (see Methods). The noise has a small effect on measurements of $L \sim V$ scaling (C), and a larger effect on $r^2 \sim L/D$ scaling (D). Subtree length (E) and depth (F) asymmetries show weaker correlations with r^2 asymmetry, as in the experimental results (A-B).

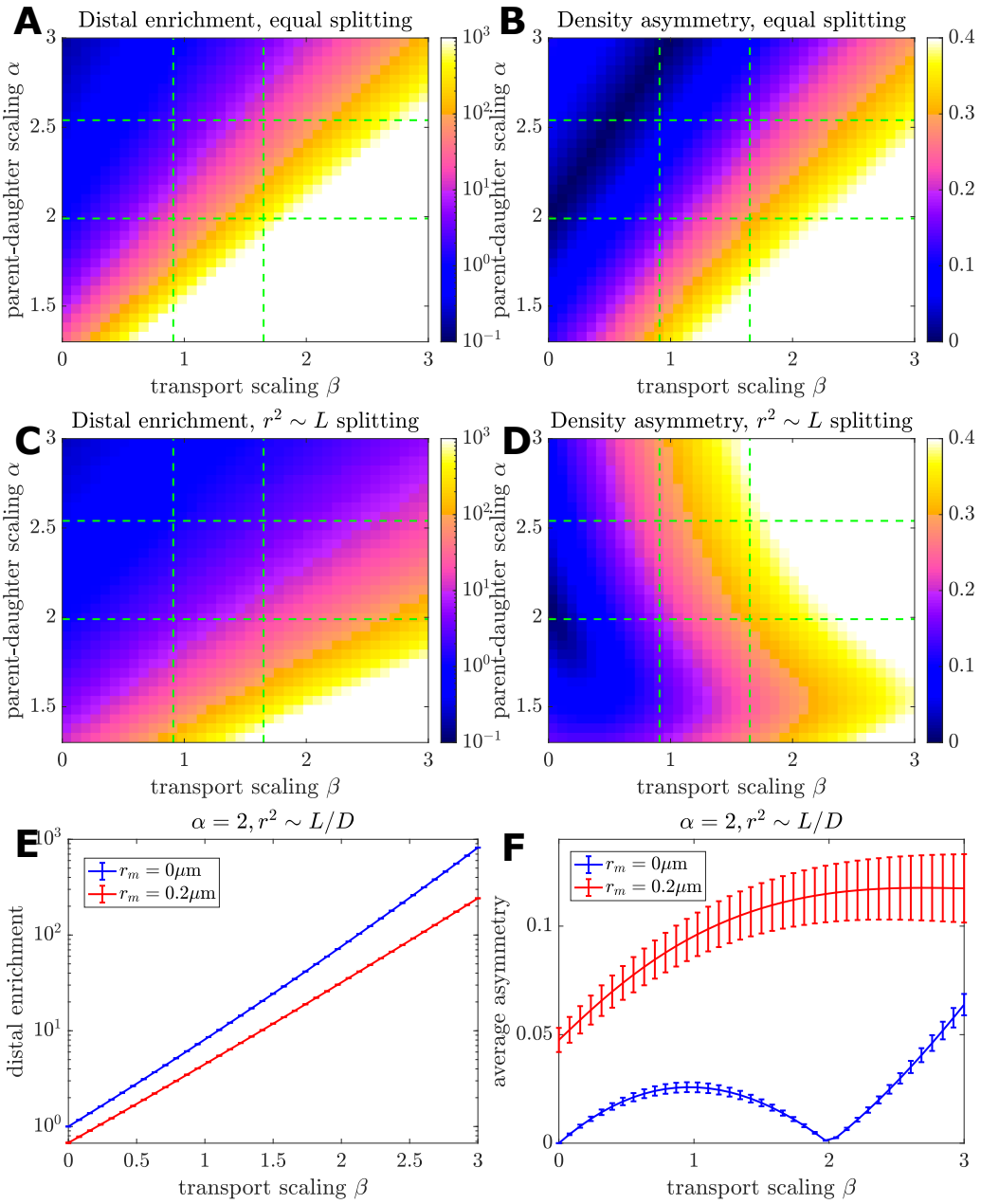

Figure C.5. Model mitochondrial distributions in dendrites that obey different scaling rules. A-D: Average mitochondrial distal enrichment (A,C) and density asymmetry (B,D) calcu- lated as a function of α (parent-daughter scaling) and β (transport scaling) for dendrites that obey sister subtree scaling with $r_1 = r_2$ (equitable splitting; A-B) or $r^2 \sim L$ (C-D). Green dashed lines indicate 95% confidence intervals for experimental measurements of α and β. E-F: Average distal enrichment (E) and density asymmetry (F) calculated as a function of β, for $r^2 \sim L/D$ and parent-daughter scaling with (red) or without (blue) a minimum radius (r_m). Including the minimum radius leads to less distal enrichment (E) and greater density asymmetry (F).

Bibliography

[1] Figure generated with the aid of servier medical art, licensed under a creative common attribution 3.0 generic license. http://smart.servier.com/.

[2] Anamika Agrawal, Zubenelgenubi C Scott, and Elena F Koslover. Morphology and transport in eukaryotic cells. *Annual review of biophysics*, 51, 2022.

[3] Patrick Amar, Guillaume Legent, Michel Thellier, Camille Ripoll, Gilles Bernot, Thomas Nystrom, Milton H Saier, and Vic Norris. A stochastic automaton shows how enzyme assemblies may contribute to metabolic efficiency. *Bmc Syst Biol*, 2(1):27, 2008.

[4] G. Ashrafi, J.S. Schlehe, M.J. LaVoie, and T.L. Schwarz. Mitophagy of damaged mitochondria occurs locally in distal neuronal axons and requires pink1 and parkin. *Journal of Cell Biology*, 206:655–670, 2014.

[5] G. Ashrafi and T.L. Schwarz. The pathways of mitophagy for quality control and clearance of mitochondria. *Cell Death Differ*, 20:31–42, 2013.

[6] Ghazaleh Ashrafi and Timothy A Ryan. Glucose metabolism in nerve terminals. *Curr Opin Neurobiol*, 45:156–161, 2017.

[7] Ghazaleh Ashrafi, Julia S Schlehe, Matthew J LaVoie, and Thomas L Schwarz. Mitophagy of damaged mitochondria occurs locally in distal neuronal axons and requires pink1 and parkin. *Journal of Cell Biology*, 206(5):655–670, 2014.

[8] Ghazaleh Ashrafi, Zhuhao Wu, Ryan J Farrell, and Timothy A Ryan. Glut4 mobilization supports energetic demands of active synapses. *Neuron*, 93(3):606–615, 2017.

[9] Y. Bai and T. Suzuki. Activity-dependent synaptic plasticity in drosophila melanogaster. *Front Physiol*, 11:161, 2020.

[10] Robert S Balaban, Shino Nemoto, and Toren Finkel. Mitochondria, oxidants, and aging. *cell*, 120(4):483–495, 2005.

[11] Robert H Baloh. Mitochondrial dynamics and peripheral neuropathy. *Neuroscientist*, 14(1):12–18, 2008.

[12] Robert H Baloh, Robert E Schmidt, Alan Pestronk, and Jeffrey Milbrandt. Altered axonal mitochondrial transport in the pathogenesis of charcot-marie-tooth disease from mitofusin 2 mutations. *J Neurosci*, 27(2):422–430, 2007.

[13] Daniel Barazany, Peter J Basser, and Yaniv Assaf. In vivo measurement of axon diameter distribution in the corpus callosum of rat brain. *Brain*, 132(5):1210–1220, 2009.

[14] Erin L Barnhart. Mechanics of mitochondrial motility in neurons. *Current opinion in cell biology*, 38:90–99, 2016.

[15] Erin L Barnhart, Irving E Wang, Huayi Wei, Claude Desplan, and Thomas R Clandinin. Sequential nonlinear filtering of local motion cues by global motion circuits. *Neuron*, 100(1):229–243, 2018.

[16] B. Bommel, A. Konietzny, O. Kobler, J. Bar, and M. Mikhaylova. F-actin patches associated with glutamatergic synapses control positioning of dendritic lysosomes. *Embo J*, 38:101183, 2019.

[17] Frank Bradke, James W Fawcett, and Micha E Spira. Assembly of a new growth cone after axotomy: the precursor to axon regeneration. *Nature Reviews Neuroscience*, 13(3):183–193, 2012.

[18] Barry Bunow, Jean-Pierre Kernevez, Gislaine Joly, and Daniel Thomas. Pattern formation by reaction-diffusion instabilities: Application to morphogenesis in drosophila. *J Theor Biol*, 84(4):629–649, 1980.

[19] Dana A Burow, Maxine C Umeh-Garcia, Marie B True, Crystal D Bakhaj, David H Ardell, and Michael D Cleary. Dynamic regulation of mrna decay during neural development. *Neural development*, 10(1):11, 2015.

[20] AM Butt, M Ibrahim, and M Berry. Axon-myelin sheath relations of oligodendrocyte unit phenotypes in the adult rat anterior medullary velum. *J Neurocytol*, 27(4):205–217, 1998.

[21] Zoltán Bódi, Zoltán Farkas, Dmitry Nevozhay, Dorottya Kalapis, Viktória Lázár, Bálint Csörgő, Ákos Nyerges, Béla Szamecz, Gergely Fekete, Balázs Papp, Hugo Araújo, José L. Oliveira, Gabriela Moura, Manuel A. S. Santos, Tamás Székely Jr, Gábor Balázsi, and Csaba Pál. Phenotypic heterogeneity promotes adaptive evolution. *PLoS biology*, 15(5):e2000644, 2017.

[22] M. Cagalinec, D. Safiulina, M. Liiv, J. Liiv, V. Choubey, P. Wareski, V. Veksler, and A. Kaasik. Principles of the mitochondrial fusion and fission cycle in neurons. *J Cell Sci*, 126:2187–2197, 2013.

[23] Michal Cagalinec, Dzhamilja Safiulina, Mailis Liiv, Joanna Liiv, Vinay Choubey, Przemyslaw Wareski, Vladimir Veksler, and Allen Kaasik. Principles of the mitochondrial fusion and fission cycle in neurons. *Journal of cell science*, 126(10):2187–2197, 2013.

[24] Qian Cai, Hesham Mostafa Zakaria, Anthony Simone, and Zu-Hang Sheng. Spatial parkin translocation and degradation of damaged mitochondria via mitophagy in live cortical neurons. *Current Biology*, 22(6):545–552, 2012.

[25] Iván J Cajigas, Georgi Tushev, Tristan J Will, Susanne tom Dieck, Nicole Fuerst, and Erin M Schuman. The local transcriptome in the synaptic neuropil revealed by deep sequencing and high-resolution imaging. *Neuron*, 74(3):453–466, 2012.

[26] Roberto Caminiti, Filippo Carducci, Claudia Piervincenzi, Alexandra Battaglia-Mayer, Giuseppina Confalone, Federica Visco-Comandini, Patrizia Pantano, and Giorgio M Innocenti. Diameter, length, speed, and conduction delay of callosal axons in macaque monkeys and humans: comparing data from histology and magnetic resonance imaging diffusion tractography. *Journal of Neuroscience*, 33(36):14501–14511, 2013.

[27] ANTHONY Carruthers. Facilitated diffusion of glucose. *Physiol Rev*, 70(4):1135–1176, 1990.

[28] Diane TW Chang and Ian J Reynolds. Mitochondrial trafficking and morphology in healthy and injured neurons. *Prog Neurobiol*, 80(5):241–268, 2006.

[29] Jeremy B Chang and James E Ferrell Jr. Mitotic trigger waves and the spatial coordination of the xenopus cell cycle. *Nature*, 500(7464):603, 2013.

[30] Christopher Cherniak, Mark Changizi, and Du Won Kang. Large-scale optimization of neuron arbors. *Physical Review E*, 59(5):6001, 1999.

[31] Shing Y Chiu. Matching mitochondria to metabolic needs at nodes of ranvier. *The Neuroscientist*, 17(4):343–350, 2011.

[32] Dmitri B Chklovskii and Armen Stepanyants. Power-law for axon diameters at branch point. *BMC neuroscience*, 4(1):1–7, 2003.

[33] S. Cogliati, J.A. Enriquez, and L. Scorrano. Mitochondrial cristae: Where beauty meets functionality. *Trends Biochem Sci*, 41:261–273, 2016.

[34] Christopher J Costa and Dianna E Willis. To the end of the line: axonal mrna transport and local translation in health and neurodegenerative disease. *Developmental neurobiology*, 78(3):209–220, 2018.

[35] Felipe A Court, Diane L Sherman, Thomas Pratt, Emer M Garry, Richard R Ribchester, David F Cottrell, Susan M Fleetwood-Walker, and Peter J Brophy. Restricted growth of schwann cells lacking cajal bands slows conduction in myelinated nerves. *Nature*, 431(7005):191–195, 2004.

[36] Robert K Crane and Alberto Sols. The non-competitive inhibition of brain hexokinase by glucose-6-phosphate and related compounds. *J Biol Chem*, 210(2):597–606, 1954.

[37] Hermann Cuntz, Friedrich Forstner, Alexander Borst, and Michael Häusser. One rule to grow them all: a general theory of neuronal branching and its practical application. *PLoS computational biology*, 6(8):e1000877, 2010.

[38] Hermann Cuntz, Friedrich Forstner, Bettina Schnell, Georg Ammer, Shamprasad Varija Raghu, and Alexander Borst. Preserving neural function under extreme scaling. *PloS one*, 8(8):e71540, 2013.

[39] S. Datta and M. Jaiswal. Mitochondrial calcium at the synapse. *Mitochondrion*, 59:135–153, 2021.

[40] Alison F Davis and David A Clayton. In situ localization of mitochondrial dna replication in intact mammalian cells. *The Journal of cell biology*, 135(4):883–893, 1996.

[41] C.H. Davis, K.Y. Kim, E.A. Bushong, E.A. Mills, D. Boassa, T. Shih, M. Kinebuchi, S. Phan, Y. Zhou, N.A. Bihlmeyer, J.V. Nguyen, Y. Jin, M.H. Ellisman, and N. Marsh-Armstrong. Transcellular degradation of axonal mitochondria. *Proc Natl Acad Sci U S A*, 111:9633–9638, 2014.

[42] S. Deshwal, K.U. Fiedler, and T. Langer. Mitochondrial proteases: Multifaceted regulators of mitochondrial plasticity. *Annu Rev Biochem*, 89:501–528, 2020.

[43] Aline R Dörrbaum, Lisa Kochen, Julian D Langer, and Erin M Schuman. Local and global influences on protein turnover in neurons and glia. *Elife*, 7:e34202, 2018.

[44] Michael Doyle and Michael A Kiebler. Mechanisms of dendritic mrna transport and its role in synaptic tagging. *The EMBO journal*, 30(17):3540–3552, 2011.

[45] C.M. Drerup, A.L. Herbert, K.R. Monk, and A.V. Nechiporuk. Regulation of mitochondria-dynactin interaction and mitochondrial retrograde transport in axons. *Elife*, 6, 2017.

[46] Roman Duelli and Wolfgang Kuschinsky. Brain glucose transporters: relationship to local energy demand. *Physiology*, 16(2):71–76, 2001.

[47] Francis Duffieux, Joris Van Roy, Paul AM Michels, and Fred R Opperdoes. Molecular characterisation of the first two enzymes of the pentose-phosphate pathway of trypanosoma brucei. *Journal of Biological Chemistry*, 2000.

[48] Christophe Eloy. Leonardo's rule, self-similarity, and wind-induced stresses in trees. *Physical review letters*, 107(25):258101, 2011.

[49] C Fabricius, C-H Berthold, and M Rydmark. Axoplasmic organelles at nodes of ranvier. ii. occurrence and distribution in large myelinated spinal cord axons of the adult cat. *J Neurocytol*, 22(11):941–954, 1993.

[50] Michelle C Faits, Chunmeng Zhang, Florentina Soto, and Daniel Kerschensteiner. Dendritic mitochondria reach stable positions during circuit development. *Elife*, 5:e11583, 2016.

[51] Don Wayne Fawcett. *The cell: its organelles and inclusions: an atlas of fine structure*. Number 576.31 FAW. 1981.

[52] Andrew W Ferree, Kyle Trudeau, Eden Zik, Ilan Y Benador, Gilad Twig, Roberta A Gottlieb, and Orian S Shirihai. Mitotimer probe reveals the impact of autophagy, fusion, and motility on subcellular distribution of young and old mitochondrial protein and on relative mitochondrial protein age. *Autophagy*, 9(11):1887–1896, 2013.

[53] Jainne M Ferreira, Arthur L Burnett, and Gerald A Rameau. Activity-dependent regulation of surface glucose transporter-3. *J Neurosci*, 31(6):1991–1999, 2011.

[54] Yombe Fonkeu, Nataliya Kraynyukova, Anne-Sophie Hafner, Lisa Kochen, Fabio Sartori, Erin M Schuman, and Tatjana Tchumatchenko. How mrna localization and protein synthesis sites influence dendritic protein distribution and dynamics. *Neuron*, 103(6):1109–1122, 2019.

[55] M.R. Freeman. Drosophila central nervous system glia, cold spring harb perspect biol 7, 2015.

[56] Shinya Fujii and Ernest Beutler. High glucose concentrations partially release hexokinase from inhibition by glucose 6-phosphate. *P Natl Acad Sci*, 82(5):1552–1554, 1985.

[57] R.X. Gao, S.M. Asano, S. Upadhyayula, I. Pisarev, D.E. Milkie, T.L. Liu, V. Singh, A. Graves, G.H. Huynh, Y.X. Zhao, J. Bogovic, J. Colonell, C.M. Ott, C. Zugates, S. Tappan, A. Rodriguez, K.R. Mosaliganti, S.H. Sheu, H.A. Pasolli, S. Pang, C.S. Xu, S.G. Megason, H. Hess, J. Lippincott-Schwartz, A. Hantman, G.M. Rubin, T. Kirchhausen, S. Saalfeld, Y. Aso, E.S. Boydent, and E. Betzig. Cortical column and whole-brain imaging with molecular contrast and nanoscale resolution. *Science*, 363:245–, 2019.

[58] T. Gisiger. Scale invariance in biology: coincidence or footprint of a universal mechanism? *Biol Rev*, 76:161–209, 2001.

[59] Elizabeth E Glater, Laura J Megeath, R Steven Stowers, and Thomas L Schwarz. Axonal transport of mitochondria requires milton to recruit kinesin heavy chain and is light chain independent. *The Journal of cell biology*, 173(4):545–557, 2006.

[60] Caspar Glock, Maximilian Heumüller, and Erin M Schuman. mrna transport & local translation in neurons. *Current opinion in neurobiology*, 45:169–177, 2017.

[61] Ann YN Goldstein, Xinnan Wang, and Thomas L Schwarz. Axonal transport and the delivery of pre-synaptic components. *Current opinion in neurobiology*, 18(5):495–503, 2008.

[62] Abolfazl Golestani, Hassan Ramshini, and Mohsen Nemat-Gorgani. A study on the two binding sites of hexokinase on brain mitochondria. *Bmc Biochem*, 8(1):20, 2007.

[63] R.M. Golovin, J. Vest, D.J. Vita, and K. Broadie. Activity-dependent remodeling of drosophila olfactory sensory neuron brain innervation during an early-life critical period. *J Neurosci*, 39:2995–3012, 2019.

[64] Carolina González and Andrés Couve. The axonal endoplasmic reticulum and protein trafficking: Cellular bootlegging south of the soma. In *Seminars in cell & developmental biology*, volume 27, pages 23–31. Elsevier, 2014.

[65] Thomas Gregor, William Bialek, Rob R de Ruyter van Steveninck, David W Tank, and Eric F Wieschaus. Diffusion and scaling during early embryonic pattern formation. *P Natl Acad Sci Usa*, 102(51):18403–18407, 2005.

[66] R Grima and S Schnell. A systematic investigation of the rate laws valid in intracellular environments. *Biophys Chem*, 124(1):1–10, 2006.

[67] Pedro Guedes-Dias and Erika LF Holzbaur. Axonal transport: Driving synaptic function. *Science*, 366(6462):eaaw9997, 2019.

[68] Xiufang Guo, Greg T Macleod, Andrea Wellington, Fangle Hu, Sarvari Panchumarthi, Miriam Schoenfield, Leo Marin, Milton P Charlton, Harold L Atwood, and Konrad E Zinsmaier. The gtpase dmiro is required for axonal transport of mitochondria to drosophila synapses. *Neuron*, 47(3):379–393, 2005.

[69] Aric A. Hagberg, Daniel A. Schult, and Pieter J. Swart. Exploring network structure, dynamics, and function using networkx. In Gaël Varoquaux, Travis Vaught, and Jarrod Millman, editors, *Proceedings of the 7th Python in Science Conference*, pages 11 – 15, Pasadena, CA USA, 2008.

[70] Catherine N Hall, Miriam C Klein-Flügge, Clare Howarth, and David Attwell. Oxidative phosphorylation, not glycolysis, powers presynaptic and postsynaptic mechanisms underlying brain information processing. *J Neurosci*, 32(26):8940–8951, 2012.

[71] C.N. Hall, M.C. Klein-Flugge, C. Howarth, and D. Attwell. Oxidative phosphorylation, not glycolysis, powers presynaptic and postsynaptic mechanisms underlying brain information processing. *Journal of Neuroscience*, 32:8940–8951, 2012.

[72] Julia J Harris and David Attwell. The energetics of cns white matter. *J Neurosci*, 32(1):356–371, 2012.

[73] Julia J Harris, Renaud Jolivet, and David Attwell. Synaptic energy use and supply. *Neuron*, 75(5):762–777, 2012.

[74] Gerald W Hart, Michael P Housley, and Chad Slawson. Cycling of o-linked β-n-acetylglucosamine on nucleocytoplasmic proteins. *Nature*, 446(7139):1017, 2007.

[75] Gerald W Hart, Chad Slawson, Genaro Ramirez-Correa, and Olof Lagerlof. Cross talk between o-glcnacylation and phosphorylation: roles in signaling, transcription, and chronic disease. *Annu Rev Biochem*, 80:825–858, 2011.

[76] Richard Hawkins, WILLIAM K Hass, and JOSEPH Ransohoff. Measurement of regional brain glucose utilization in vivo using [2 (-14) c] glucose. *Upd Int Car*, 10(6):690–703, 1979.

[77] Nobutaka Hirokawa, Yasuko Noda, Yosuke Tanaka, and Shinsuke Niwa. Kinesin superfamily motor proteins and intracellular transport. *Nature reviews Molecular cell biology*, 10(10):682–696, 2009.

[78] Hanne Hoitzing, Iain G Johnston, and Nick S Jones. What is the function of mitochondrial networks? a theoretical assessment of hypotheses and proposal for future research. *Bioessays*, 37(6):687–700, 2015.

[79] Christine E Holt and Erin M Schuman. The central dogma decentralized: new perspectives on rna function and local translation in neurons. *Neuron*, 80(3):648–657, 2013.

[80] Martin Howard, Andrew D Rutenberg, and Simon de Vet. Dynamic compartmentalization of bacteria: accurate division in e. coli. *Phys Rev Lett*, 87(27):278102, 2001.

[81] M Ibrahim, AM Butt, and M Berry. Relationship between myelin sheath diameter and internodal length in axons of the anterior medullary velum of the adult rat. *J Neurol Sci*, 133(1):119–127, 1995.

[82] Kie Itoh, Ken Nakamura, Miho Iijima, and Hiromi Sesaki. Mitochondrial dynamics in neurodegeneration. *Trends in cell biology*, 23(2):64–71, 2013.

[83] JM Jacobs. On internodal length. *J Anat*, 157:153, 1988.

[84] Scott John, James N Weiss, and Bernard Ribalet. Subcellular localization of hexokinases i and ii directs the metabolic fate of glucose. *PloS one*, 6(3):e17674, 2011.

[85] Scott A John, Michela Ottolia, James N Weiss, and Bernard Ribalet. Dynamic modulation of intracellular glucose imaged in single cells using a fret-based glucose nanosensor. *Pflügers Archiv-European Journal of Physiology*, 456(2):307–322, 2008.

[86] Dinesh C Joshi, Chuan-Li Zhang, Lavanya Babujee, Jason D Vevea, Benjamin K August, Zu-Hang Sheng, Edwin R Chapman, Timothy M Gomez, and Shing Yan Chiu. Inappropriate intrusion of an axonal mitochondrial anchor into dendrites causes neurodegeneration. *Cell reports*, 29(3):685–696, 2019.

[87] Hosung Jung, Byung C Yoon, and Christine E Holt. Axonal mrna localization and local protein synthesis in nervous system assembly, maintenance and repair. *Nature Reviews Neuroscience*, 13(5):308–324, 2012.

[88] Shirley E Kahana, Oliver H Lowry, Demoy W Schulz, Janet V Passonneau, and Elizabeth J Crawford. The kinetics of phosphoglucoisomerase. *Journal of Biological Chemistry*, 235(8):2178–2184, 1960.

[89] Jian-Sheng Kang, Jin-Hua Tian, Ping-Yue Pan, Philip Zald, Cuiling Li, Chuxia Deng, and Zu-Hang Sheng. Docking of axonal mitochondria by syntaphilin controls their mobility and affects short-term facilitation. *Cell*, 132(1):137–148, 2008.

[90] L.C. Kapitein and C.C. Hoogenraad. Building the neuronal microtubule cytoskeleton. *Neuron*, 87:492–506, 2015.

[91] Barry B Kaplan, Anthony E Gioio, Mi Hillefors, and Armaz Aschrafi. Axonal protein synthesis and the regulation of local mitochondrial function. In *Cell biology of the axon*, pages 1–25. Springer, 2009.

[92] Eugene A Katrukha, Daphne Jurriens, Desiree M Salas Pastene, and Lukas C Kapitein. Quantitative mapping of dense microtubule arrays in mammalian neurons. *Elife*, 10:e67925, 2021.

[93] Boris N Kholodenko. Cell-signalling dynamics in time and space. *Nat Rev Mol Cell Bio*, 7(3):165, 2006.

[94] Yongsung Kim, Xinde Zheng, Zoya Ansari, Mark C. Bunnell, Joseph R. Herdy, Larissa Traxler, Hyungjun Lee, Apua C.M. Paquola, Chrysanthi Blithikioti, Manching Ku, Johannes C.M. Schlachetzki, Jürgen Winkler, Frank Edenhofer, Christopher K. Glass, Andres A. Paucar, Baptiste N. Jaeger, Son Pham, Leah Boyer, Benjamin C. Campbell, Tony Hunter, Jerome Mertens, and Fred H. Gage. Mitochondrial aging defects emerge in directly reprogrammed human neurons due to their metabolic profile. *Cell reports*, 23(9):2550–2558, 2018.

[95] A.B. Knott, G. Perkins, R. Schwarzenbacher, and E. Bossy-Wetzel. Mitochondrial fragmentation in neurodegeneration. *Nat Rev Neurosci*, 9:505–518, 2008.

[96] Shigeru Kondo and Takashi Miura. Reaction-diffusion model as a framework for understanding biological pattern formation. *Science*, 329(5999):1616–1620, 2010.

[97] Lauren M Kraft and Laura L Lackner. Mitochondrial anchors: positioning mitochondria and more. *Biochemical and biophysical research communications*, 500(1):2–8, 2018.

[98] Nicholas J Kruger and Antje von Schaewen. The oxidative pentose phosphate pathway: structure and organisation. *Current opinion in plant biology*, 6(3):236–246, 2003.

[99] Rep Kubo. The fluctuation-dissipation theorem. *Reports on progress in physics*, 29(1):255, 1966.

[100] Yoshiyuki Kubota, Fuyuki Karube, Masaki Nomura, Allan T Gulledge, Atsushi Mochizuki, Andreas Schertel, and Yasuo Kawaguchi. Conserved properties of dendritic trees in four cortical interneuron subtypes. *Scientific reports*, 1(1):1–13, 2011.

[101] V.V. Kulkarni, A. Anand, J.B. Herr, C. Miranda, M.C. Vogel, and S. Maday. Synaptic activity controls autophagic vacuole motility and function in dendrites. *J Cell Biol*, page 220, 2021.

[102] Jocelyn D Laughton, Philippe Bittar, Yves Charnay, Luc Pellerin, Enikö Kovari, Pierre J Magistretti, and Constantin Bouras. Metabolic compartmentalization in the human cortex and hippocampus: evidence for a cell-and region-specific localization of lactate dehydrogenase 5 and pyruvate dehydrogenase. *Bmc Neurosci*, 8(1):35, 2007.

[103] J.Y. Lee and S.J. Lee. Murray's law and the bifurcation angle in the arterial microcirculation system and their application to the design of microfluidics. *Microfluid Nanofluid*, 8:85–95, 2010.

[104] Sun-Kyung Lee and Peter J Hollenbeck. Organization and translation of mrna in sympathetic axons. *Journal of Cell Science*, 116(21):4467–4478, 2003.

[105] Romain Lehnebach, Robert Beyer, Véronique Letort, and Patrick Heuret. The pipe model theory half a century on: a review. *Annals of botany*, 121(5):773–795, 2018.

[106] Ben Lehner and Kunihiko Kaneko. Fluctuation and response in biology. *Cellular and Molecular Life Sciences*, 68(6):1005–1010, 2011.

[107] F. Leiss, E. Koper, I. Hein, W. Fouquet, J. Lindner, S. Sigrist, and G. Tavosanis. Characterization of dendritic spines in the drosophila central nervous system. *Dev Neurobiol*, 69:221–234, 2009.

[108] William B Levy and Victoria G Calvert. Communication consumes 35 times more energy than computation in the human cortex, but both costs are needed to predict synapse number. *Proceedings of the National Academy of Sciences*, 118(18), 2021.

[109] Tommy L Lewis Jr, Gergely F Turi, Seok-Kyu Kwon, Attila Losonczy, and Franck Polleux. Progressive decrease of mitochondrial motility during maturation of cortical axons in vitro and in vivo. *Current Biology*, 26(19):2602–2608, 2016.

[110] Yanyan Li, Céline Roux, Sylvie Lazereg, Jean-Pierre LeCaer, Olivier Laprévote, Bernard Badet, and Marie-Ange Badet-Denisot. Identification of a novel serine phosphorylation site in human glutamine: fructose-6-phosphate amidotransferase isoform 1. *Biochemistry-us*, 46(45):13163–13169, 2007.

[111] Zheng Li, Ken-Ichi Okamoto, Yasunori Hayashi, and Morgan Sheng. The importance of dendritic mitochondria in the morphogenesis and plasticity of spines and synapses. *Cell*, 119(6):873–887, 2004.

[112] Maijia Liao, Xin Liang, and Jonathon Howard. The narrowing of dendrite branches across nodes follows a well-defined scaling law. *Proceedings of the National Academy of Sciences*, 118(27), 2021.

[113] Daniel Liewald, Robert Miller, Nikos Logothetis, Hans-Joachim Wagner, and Almut Schüz. Distribution of axon diameters in cortical white matter: an electron-microscopic study on three human brains and a macaque. *Biol Cybern*, 108(5):541–557, 2014.

[114] David M Lipton, Celine I Maeder, and Kang Shen. Rapid assembly of presynaptic materials behind the growth cone in dopaminergic neurons is mediated by precise regulation of axonal transport. *Cell reports*, 24(10):2709–2722, 2018.

[115] Xingguo Liu, David Weaver, Orian Shirihai, and György Hajnóczky. Mitochondrial 'kiss-and-run': interplay between mitochondrial motility and fusion–fission dynamics. *The EMBO journal*, 28(20):3074–3089, 2009.

[116] Ying Liu, Fei Liu, Khalid Iqbal, Inge Grundke-Iqbal, and Cheng-Xin Gong. Decreased glucose transporters correlate to abnormal hyperphosphorylation of tau in alzheimer disease. *Febs Lett*, 582(2):359–364, 2008.

[117] W. Lu, M. Lakonishok, R. Liu, N. Billington, A. Rich, M. Glotzer, J.R. Sellers, and V.I. Gelfand. Competition between kinesin-1 and myosin-v defines drosophila posterior determination. *Elife*, 9, 2020.

[118] Andrew F MacAskill and Josef T Kittler. Control of mitochondrial transport and localization in neurons. *Trends Cell Biol*, 20(2):102–112, 2010.

[119] Andrew F MacAskill, Johanne E Rinholm, Alison E Twelvetrees, I Lorena Arancibia-Carcamo, James Muir, Asa Fransson, Pontus Aspenstrom, David Attwell, and Josef T Kittler. Miro1 is a calcium sensor for glutamate receptor-dependent localization of mitochondria at synapses. *Neuron*, 61(4):541–555, 2009.

[120] Sandra Maday, Karen E Wallace, and Erika LF Holzbaur. Autophagosomes initiate distally and mature during transport toward the cell soma in primary neurons. *Journal of Cell Biology*, 196(4):407–417, 2012.

[121] Paolo Magnani, P Varghese Cherian, Gwyn W Gould, Douglas A Greene, Anders AF Sima, and Frank C Brosius III. Glucose transporters in rat peripheral nerve: paranodal expression of glut1 and glut3. *Metabolism*, 45(12):1466–1473, 1996.

[122] Jordi Magrané, Mary Anne Sahawneh, Serge Przedborski, Álvaro G Estévez, and Giovanni Manfredi. Mitochondrial dynamics and bioenergetic dysfunction is associated with synaptic alterations in mutant sod1 motor neurons. *Journal of Neuroscience*, 32(1):229–242, 2012.

[123] Fran Maher, Theresa M Davies-Hill, and Ian A Simpson. Substrate specificity and kinetic parameters of glut3 in rat cerebellar granule neurons. *Biochem J*, 315(Pt 3):827, 1996.

[124] M.S. Maisak, J. Haag, G. Ammer, E. Serbe, M. Meier, A. Leonhardt, T. Schilling, A. Bahl, G.M. Rubin, A. Nern, B.J. Dickson, D.F. Reiff, E. Hopp, and A. Borst. A directional tuning map of drosophila elementary motion detectors. *Nature*, 500:212–216, 2013.

[125] A. Mandal, H.T.C. Wong, K. Pinter, N. Mosqueda, A. Beirl, R.M. Lomash, S. Won, K.S. Kindt, and C.M. Drerup. Retrograde mitochondrial transport is essential for organelle distribution and health in zebrafish neurons. *Journal of Neuroscience*, 41:1371–1392, 2021.

[126] Amrita Mandal, Hiu-Tung C Wong, Katherine Pinter, Natalie Mosqueda, Alisha Beirl, Richa Madan Lomash, Sehoon Won, Katie S Kindt, and Catherine M Drerup. Retrograde

mitochondrial transport is essential for organelle distribution and health in zebrafish neurons. *Journal of Neuroscience*, 2020.

[127] K. Mann, S. Deny, S. Ganguli, and T.R. Clandinin. Coupling of activity, metabolism and behaviour across the drosophila brain. *Nature*, 593:244–248, 2021.

[128] Fernando M Mar, Anabel R Simões, Sérgio Leite, Marlene M Morgado, Telma E Santos, Inês S Rodrigo, Carla A Teixeira, Thomas Misgeld, and Mónica M Sousa. Cns axons globally increase axonal transport after peripheral conditioning. *Journal of Neuroscience*, 34(17):5965–5970, 2014.

[129] P.A. Marquet, R.A. Quinones, S. Abades, F. Labra, M. Tognelli, M. Arim, and M. Rivadeneira. Scaling and power-laws in ecological systems. *J Exp Biol*, 208:1749–1769, 2005.

[130] MATLAB. *version 9.5 (R2018b)*. The MathWorks Inc., Natick, Massachusetts, 2018.

[131] Wakoto Matsuda, Takahiro Furuta, Kouichi C Nakamura, Hiroyuki Hioki, Fumino Fujiyama, Ryohachi Arai, and Takeshi Kaneko. Single nigrostriatal dopaminergic neurons form widely spread and highly dense axonal arborizations in the neostriatum. *J Neurosci*, 29(2):444–453, 2009.

[132] Ewan C McNay, Richard C McCarty, and Paul E Gold. Fluctuations in brain glucose concentration during behavioral testing: dissociations between brain areas and between brain and blood. *Neurobiol Learn Mem*, 75(3):325–337, 2001.

[133] Kyle E Miller and Michael P Sheetz. Axonal mitochondrial transport and potential are correlated. *Journal of cell science*, 117(13):2791–2804, 2004.

[134] Sergej L Mironov. Adp regulates movements of mitochondria in neurons. *Biophys J*, 92(8):2944–2952, 2007.

[135] Thomas Misgeld and Thomas L Schwarz. Mitostasis in neurons: maintaining mitochondria in an extended cellular architecture. *Neuron*, 96(3):651–666, 2017.

[136] Prashant Mishra and David C Chan. Metabolic regulation of mitochondrial dynamics. *J Cell Biol*, pages jcb–201511036, 2016.

[137] Albert Misko, Sirui Jiang, Iga Wegorzewska, Jeffrey Milbrandt, and Robert H Baloh. Mitofusin 2 is necessary for transport of axonal mitochondria and interacts with the miro/milton complex. *Journal of Neuroscience*, 30(12):4232–4240, 2010.

[138] Pradeep K Mouli, Gilad Twig, and Orian S Shirihai. Frequency and selectivity of mitochondrial fusion are key to its quality maintenance function. *Biophysical journal*, 96(9):3509–3518, 2009.

[139] Cecil D Murray. The physiological principle of minimum work: I. the vascular system and the cost of blood volume. *Proceedings of the national academy of sciences of the united states of america*, 12(3):207, 1926.

[140] Babu Reddy Janakaloti Narayanareddy, Suvi Vartiainen, Neema Hariri, Diane K O'Dowd, and Steven P Gross. A biophysical analysis of mitochondrial movement: differences between transport in neuronal cell bodies versus processes. *Traffic*, 15(7):762–771, 2014.

[141] David G Nicholls. Mitochondrial membrane potential and aging. *Aging cell*, 3(1):35–40, 2004.

[142] Robert F Niescier, Sang Kyu Kwak, Se Hun Joo, Karen T Chang, and Kyung-Tai Min. Dynamics of mitochondrial transport in axons. *Frontiers in cellular neuroscience*, 10:123, 2016.

[143] H Nishimura, FV Pallardo, GA Seidner, S Vannucci, IA Simpson, and MJ Birnbaum. Kinetics of glut1 and glut4 glucose transporters expressed in xenopus oocytes. *J Biol Chem*, 268(12):8514–8520, 1993.

[144] V. Nithianandam and C.T. Chien. Actin blobs prefigure dendrite branching sites. *J Cell Biol*, 217:3731–3746, 2018.

[145] Jodi Nunnari and Anu Suomalainen. Mitochondria: in sickness and in health. *Cell*, 148(6):1145–1159, 2012.

[146] Jeremy D O'Connell, Alice Zhao, Andrew D Ellington, and Edward M Marcotte. Dynamic reorganization of metabolic enzymes into intracellular bodies. *Annu Rev Cell Dev Bi*, 28:89–111, 2012.

[147] Nobuhiko Ohno, Grahame J Kidd, Don Mahad, Sumiko Kiryu-Seo, Amir Avishai, Hitoshi Komuro, and Bruce D Trapp. Myelination and axonal electrical activity modulate the distribution and motility of mitochondria at cns nodes of ranvier. *J Neurosci*, 31(20):7249–7258, 2011.

[148] M. Packard, D. Mathew, and V. Budnik. Wnts and tgf beta in synaptogenesis: Old friends signalling at new places. *Nature Reviews Neuroscience*, 4:113–120, 2003.

[149] W Paschen, BK Siesjö, M Ingvar, and K-A Hossmann. Regional differences in brain glucose content in graded hypoglycemia. *Neurochem Pathol*, 5(2):131–142, 1986.

[150] Pinkesh K Patel, Orian Shirihai, and Kerwyn Casey Huang. Optimal dynamics for quality control in spatially distributed mitochondrial networks. *PLoS Comput Biol*, 9(7):e1003108, 2013.

[151] D. Pathak, K.J. Sepp, and P.J. Hollenbeck. Evidence that myosin activity opposes microtubule-based axonal transport of mitochondria. *Journal of Neuroscience*, 30:8984–8992, 2010.

[152] P. Paumard, J. Vaillier, B. Coulary, J. Schaeffer, V. Soubannier, D.M. Mueller, D. Brethes, J.P. Rago, and J. Velours. The atp synthase is involved in generating mitochondrial cristae morphology. *Embo J*, 21:221–230, 2002.

[153] Gulcin Pekkurnaz, Jonathan C Trinidad, Xinnan Wang, Dong Kong, and Thomas L Schwarz. Glucose regulates mitochondrial motility via milton modification by o-glcnac transferase. *Cell*, 158(1):54–68, 2014.

[154] Claire Peppiatt and David Attwell. Neurobiology: feeding the brain. *Nature*, 431(7005):137, 2004.

[155] János A Perge, Kristin Koch, Robert Miller, Peter Sterling, and Vijay Balasubramanian. How the optic nerve allocates space, energy capacity, and information. *J Neurosci*, 29(24):7917–7928, 2009.

[156] János A Perge, Jeremy E Niven, Enrico Mugnaini, Vijay Balasubramanian, and Peter Sterling. Why do axons differ in caliber? *J Neurosci*, 32(2):626–638, 2012.

[157] G.A. Perkins and M.H. Ellisman. Mitochondrial configurations in peripheral nerve suggest differential atp production. *J Struct Biol*, 173:117–127, 2011.

[158] Aaron D Pilling, Dai Horiuchi, Curtis M Lively, and William M Saxton. Kinesin-1 and dynein are the primary motors for fast transport of mitochondria in drosophila motor axons. *Molecular biology of the cell*, 17(4):2057–2068, 2006.

[159] Natalia B Pivovarova and S Brian Andrews. Calcium-dependent mitochondrial function and dysfunction in neurons. *The FEBS journal*, 277(18):3622–3636, 2010.

[160] Gabriela Plucińska, Dominik Paquet, Alexander Hruscha, Leanne Godinho, Christian Haass, Bettina Schmid, and Thomas Misgeld. In vivo imaging of disease-related mitochondrial dynamics in a vertebrate model system. *Journal of Neuroscience*, 32(46):16203–16212, 2012.

[161] V. Popov, N.I. Medvedev, H.A. Davies, and M.G. Stewart. Mitochondria form a filamentous reticular network in hippocampal dendrites but are present as discrete bodies in axons: A three-dimensional ultrastructural study. *J Comp Neurol*, 492:50–65, 2005.

[162] James W Posakony, James M England, and Giuseppe Attardi. Mitochondrial growth and division during the cell cycle in hela cells. *J Cell Biol*, 74(2):468–491, 1977.

[163] Joseph John Pysh and Talat Khan. Variations in mitochondrial structure and content of neurons and neuroglia in rat brain: an electron microscopic study. *Brain Res*, 36(1):1–18, 1972.

[164] Wilfrid Rall. Branching dendritic trees and motoneuron membrane resistivity. *Experimental neurology*, 1(5):491–527, 1959.

[165] Vidhya Rangaraju, Nathaniel Calloway, and Timothy A Ryan. Activity-driven local atp synthesis is required for synaptic function. *Cell*, 156(4):825–835, 2014.

[166] Vidhya Rangaraju, Marcel Lauterbach, and Erin M Schuman. Spatially stable mitochondrial compartments fuel local translation during plasticity. *Cell*, 176(1-2):73–84, 2019.

[167] WT Regenold, M Pratt, S Nekkalapu, PS Shapiro, T Kristian, and G Fiskum. Mitochondrial detachment of hexokinase 1 in mood and psychotic disorders: implications for brain energy metabolism and neurotrophic signaling. *J Psychiatr Res*, 46(1):95–104, 2012.

[168] R Brooks Robey, Jianfei Ma, and Anna VP Santos. Regulation of mesangial cell hexokinase activity by pkc and the classic mapk pathway. *Am J Physiol-renal*, 277(5):F742–F749, 1999.

[169] Jack Rosenbluth. Multiple functions of the paranodal junction of myelinated nerve fibers. *J Neurosci Res*, 87(15):3250–3258, 2009.

[170] Gary J Russo, Kathryn Louie, Andrea Wellington, Greg T Macleod, Fangle Hu, Sarvari Panchumarthi, and Konrad E Zinsmaier. Drosophila miro is required for both anterograde and retrograde axonal mitochondrial transport. *J Neurosci*, 29(17):5443–5455, 2009.

[171] Aiman S Saab, Iva D Tzvetanova, and Klaus-Armin Nave. The role of myelin and oligodendrocytes in axonal energy metabolism. *Curr Opin Neurobiol*, 23(6):1065–1072, 2013.

[172] S. Sachse, E. Rueckert, A. Keller, R. Okada, N.K. Tanaka, K. Ito, and L.B. Vosshall. Activity-dependent plasticity in an olfactory circuit. *Neuron*, 56:838–850, 2007.

[173] D. Safiulina and A. Kaasik. Energetic and dynamic: How mitochondria meet neuronal energy demands. *Plos Biology*, page 11, 2013.

[174] Pabitra K Sahoo, Deanna S Smith, Nora Perrone-Bizzozero, and Jeffery L Twiss. Axonal mrna transport and translation at a glance. *Journal of cell science*, 131(8), 2018.

[175] J. Sanders, A. Singh, G. Sterne, B. Ye, and J. Zhou. Learning-guided automatic three dimensional synapse quantification for drosophila neurons. *BMC Bioinformatics*, 16:177, 2015.

[176] Masao Saotome, Dzhamilja Safiulina, György Szabadkai, Sudipto Das, Åsa Fransson, Pontus Aspenstrom, Rosario Rizzuto, and György Hajnóczky. Bidirectional ca2+-dependent control of mitochondrial dynamics by the miro gtpase. *Proceedings of the National Academy of Sciences*, 105(52):20728–20733, 2008.

[177] Katsuhiko Sato, Yoichiro Ito, Tetsuya Yomo, and Kunihiko Kaneko. On the relation between fluctuation and response in biological systems. *Proceedings of the National Academy of Sciences*, 100(24):14086–14090, 2003.

[178] William M Saxton and Peter J Hollenbeck. The axonal transport of mitochondria. *J Cell Sci*, 125(9):2095–2104, 2012.

[179] Bettina Schnell, Maximilian Joesch, F Forstner, Shamprasad V Raghu, Hideo Otsuna, Kei Ito, Alexander Borst, and Dierk Frithjof Reiff. Processing of horizontal optic flow in three visual interneurons of the drosophila brain. *Journal of neurophysiology*, 103(3):1646–1657, 2010.

[180] Björn Schwanhäusser, Dorothea Busse, Na Li, Gunnar Dittmar, Johannes Schuchhardt, Jana Wolf, Wei Chen, and Matthias Selbach. Global quantification of mammalian gene expression control. *Nature*, 473(7347):337–342, 2011.

[181] Thomas L Schwarz. Mitochondrial trafficking in neurons. *Cold Spring Harbor perspectives in biology*, 5(6):a011304, 2013.

[182] Klaus Schwerzmann, Hans Hoppeler, Susan R Kayar, and Ewald R Weibel. Oxidative capacity of muscle and mitochondria: correlation of physiological, biochemical, and morphometric characteristics. *P Natl Acad Sci*, 86(5):1583–1587, 1989.

[183] E.K. Scott, J.E. Reuter, and L.Q. Luo. Dendritic development of drosophila high order visual system neurons is independent of sensory experience. *Bmc Neurosci*, page 4, 2003.

[184] Richard Seager, Laura Lee, Jeremy M Henley, and Kevin A Wilkinson. Mechanisms and roles of mitochondrial localisation and dynamics in neuronal function. *Neuronal Signaling*, 4(2), 2020.

[185] Dan Shan, Daniel Mount, Stephen Moore, Vahram Haroutunian, James H Meador-Woodruff, and Robert E McCullumsmith. Abnormal partitioning of hexokinase 1 suggests disruption of a glutamate transport protein complex in schizophrenia. *Schizophr Res*, 154(1):1–13, 2014.

[186] Zu-Hang Sheng. Mitochondrial trafficking and anchoring in neurons: new insight and implications. *J Cell Biol*, 204(7):1087–1098, 2014.

[187] Zu-Hang Sheng and Qian Cai. Mitochondrial transport in neurons: impact on synaptic homeostasis and neurodegeneration. *Nature Reviews Neuroscience*, 13(2):77–93, 2012.

[188] Ken Shirato, Kazuki Nakajima, Hiroaki Korekane, Shinji Takamatsu, Congxiao Gao, Takashi Angata, Kazuaki Ohtsubo, and Naoyuki Taniguchi. Hypoxic regulation of glycosylation via the n-acetylglucosamine cycle. *Journal of clinical biochemistry and nutrition*, 48(1):20–25, 2010.

[189] Robert G Shulman, Douglas L Rothman, Kevin L Behar, and Fahmeed Hyder. Energetic basis of brain activity: implications for neuroimaging. *Trends Neurosci*, 27(8):489–495, 2004.

[190] Catia AP Silva, Annik Yalnizyan-Carson, M Victoria Fernández Busch, Mike van Zwieten, Matthijs Verhage, and Christian Lohmann. Activity-dependent regulation of mitochondrial motility in developing cortical dendrites. *Elife*, 10:e62091, 2021.

[191] Ian A Silver and M Erecinska. Extracellular glucose concentration in mammalian brain: continuous monitoring of changes during increased neuronal activity and upon limitation in oxygen supply in normo-, hypo-, and hyperglycemic animals. *J Neurosci*, 14(8):5068–5076, 1994.

[192] Ian A Simpson, Anthony Carruthers, and Susan J Vannucci. Supply and demand in cerebral energy metabolism: the role of nutrient transporters. *Journal of Cerebral Blood Flow & Metabolism*, 27(11):1766–1791, 2007.

[193] Ian A Simpson, Donard Dwyer, Daniela Malide, Kelle H Moley, Alexander Travis, and Susan J Vannucci. The facilitative glucose transporter glut3: 20 years of distinction. *Am J Physiol-endoc M*, 295(2):E242–E253, 2008.

[194] Laura Smit-Rigter, Rajeev Rajendran, Catia A P Silva, Liselot Spierenburg, Femke Groeneweg, Emma M Ruimschotel, Danielle van Versendaal, Chris van der Togt, Ulf T Eysel, J Alexander Heimel, Christian Lohmann, and Christiaan N Levelt. Mitochondrial dynamics in visual cortex are limited in vivo and not affected by axonal structural plasticity. *Current Biology*, 26(19):2609–2616, 2016.

[195] I. Song and R.L. Huganir. Regulation of ampa receptors during synaptic plasticity. *Trends Neurosci*, 25:578–588, 2002.

[196] R Steven Stowers, Laura J Megeath, Jolanta Górska-Andrzejak, Ian A Meinertzhagen, and Thomas L Schwarz. Axonal transport of mitochondria to synapses depends on milton, a novel drosophila protein. *Neuron*, 36(6):1063–1077, 2002.

[197] A. Sugiura, G.L. McLelland, E.A. Fon, and H.M. McBride. A new pathway for mitochondrial quality control: mitochondrial-derived vesicles. *Embo J*, 33:2142–2156, 2014.

[198] L.A. Taber, S. Ng, A.M. Quesnel, J. Whatman, and C.J. Carmen. Investigating murray's law in the chick embryo. *J Biomech*, 34:121–124, 2001.

[199] A.I. Tarasov, E.J. Griffiths, and G.A. Rutter. Regulation of atp production by mitochondrial ca2+. *Cell Calcium*, 52:28–35, 2012.

[200] R.P. Tas, A. Chazeau, B.M.C. Cloin, M.L.A. Lambers, C.C. Hoogenraad, and L.C. Kapitein. Differentiation between oppositely oriented microtubules controls polarized neuronal transport. *Neuron*, 96:1264–, 2017.

[201] Martin J Tovée. Neuronal processing: How fast is the speed of thought? *Current Biology*, 4(12):1125–1127, 1994.

[202] RR Traxinger and S Marshall. Coordinated regulation of glutamine: fructose-6-phosphate amidotransferase activity by insulin, glucose, and glutamine. role of hexosamine biosynthesis in enzyme regulation. *Journal of Biological Chemistry*, 266(16):10148–10154, 1991.

[203] Benita Turner-Bridger, Maximillian Jakobs, Leila Muresan, Hovy Ho-Wai Wong, Kristian Franze, William A Harris, and Christine E Holt. Single-molecule analysis of endogenous β-actin mrna trafficking reveals a mechanism for compartmentalized mrna localization in axons. *Proceedings of the National Academy of Sciences*, 115(41):E9697–E9706, 2018.

[204] Georgi Tushev, Caspar Glock, Maximilian Heumüller, Anne Biever, Marko Jovanovic, and Erin M Schuman. Alternative 3′ utrs modify the localization, regulatory potential, stability, and plasticity of mrnas in neuronal compartments. *Neuron*, 98(3):495–511, 2018.

[205] Gilad Twig, Alvaro Elorza, Anthony J A Molina, Hibo Mohamed, Jakob D Wikstrom, Gil Walzer, Linsey Stiles, Sarah E Haigh, Steve Katz, Guy Las, Joseph Alroy, Min Wu, Bénédicte F Py, Junying Yuan, Jude T Deeney, Barbara E Corkey, and Orian S Shirihai. Fission and selective fusion govern mitochondrial segregation and elimination by autophagy. *The EMBO journal*, 27(2):433–446, 2008.

[206] YUTAKA Uehara, VALERIE Nipper, and ANTHONY L McCALL. Chronic insulin hypoglycemia induces glut-3 protein in rat brain neurons. *Am J Physiol-endoc M*, 272(4):E716–E719, 1997.

[207] Julio A Urbina and Adelaida Crespo. Regulation of energy metabolism in trypanosoma (schizotrypanum) cruzi epimastigotes, i. hexokinase and phosphofructokinase. *Molecular and biochemical parasitology*, 11:225–239, 1984.

[208] Peter JM Van Haastert and Peter N Devreotes. Chemotaxis: signalling the way forward. *Nat Rev Mol Cell Bio*, 5(8):626, 2004.

[209] Myrrhe van Spronsen, Marina Mikhaylova, Joanna Lipka, Max A Schlager, Dave J van den Heuvel, Marijn Kuijpers, Phebe S Wulf, Nanda Keijzer, Jeroen Demmers, Lukas C Kapitein, Dick Jaarsma, Hans C Gerritsen, Anna Akhmanova, and Casper C Hoogenraad. Trak/milton motor-adaptor proteins steer mitochondrial trafficking to axons and dendrites. *Neuron*, 77(3):485–502, 2013.

[210] Marko Vendelin, Olav Kongas, and Valdur Saks. Regulation of mitochondrial respiration in heart cells analyzed by reaction-diffusion model of energy transfer. *Am J Physiol-cell Ph*, 278(4):C747–C764, 2000.

[211] Tine Verreet, Cory J Weaver, Hiromu Hino, Masahiko Hibi, and Fabienne E Poulain. Syntaphilin-mediated docking of mitochondria at the growth cone is dispensable for axon elongation in vivo. *eneuro*, 6(5), 2019.

[212] Patrik Verstreken, Cindy V Ly, Koen JT Venken, Tong-Wey Koh, Yi Zhou, and Hugo J Bellen. Synaptic mitochondria are critical for mobilization of reserve pool vesicles at drosophila neuromuscular junctions. *Neuron*, 47(3):365–378, 2005.

[213] Matheus P Viana, Aidan I Brown, Irina A Mueller, Claire Goul, Elena F Koslover, and Susanne M Rafelski. Mitochondrial fission and fusion dynamics generate efficient, robust, and evenly distributed network topologies in budding yeast cells. *Cell systems*, 2020.

[214] Evelyn S Vincow, Gennifer Merrihew, Ruth E Thomas, Nicholas J Shulman, Richard P Beyer, Michael J MacCoss, and Leo J Pallanck. The pink1–parkin pathway promotes both mitophagy and selective respiratory chain turnover in vivo. *Proceedings of the National Academy of Sciences*, 110(16):6400–6405, 2013.

[215] Shiqi Wang, Weiming Xiao, Sicong Shan, Chunsun Jiang, Ming Chen, Yan Zhang, Shouqin Lü, Juan Chen, Chuanmao Zhang, Quan Chen, and Mian Long. Multi-patterned dynamics of mitochondrial fission and fusion in a living cell. *PloS one*, 7(5):e19879, 2012.

[216] Xinnan Wang and Thomas L Schwarz. The mechanism of ca2+-dependent regulation of kinesin-mediated mitochondrial motility. *Cell*, 136(1):163–174, 2009.

[217] Xinnan Wang, Dominic Winter, Ghazaleh Ashrafi, Julia Schlehe, Yao Liang Wong, Dennis Selkoe, Sarah Rice, Judith Steen, Matthew J LaVoie, and Thomas L Schwarz. Pink1 and parkin target miro for phosphorylation and degradation to arrest mitochondrial motility. *Cell*, 147(4):893–906, 2011.

[218] Fabian Wehnekamp, Gabriela Plucińska, Rachel Thong, Thomas Misgeld, and Don C Lamb. Nanoresolution real-time 3d orbital tracking for studying mitochondrial trafficking in vertebrate axons in vivo. *Elife*, 8:e46059, 2019.

[219] Huayi Wei, Ha Young Kyung, Priscilla J Kim, and Claude Desplan. The diversity of lobula plate tangential cells (lptcs) in the drosophila motion vision system. *Journal of Comparative Physiology A*, 206(2):139–148, 2020.

[220] Petronela Weisová, Caoimhín G Concannon, Marc Devocelle, Jochen HM Prehn, and Manus W Ward. Regulation of glucose transporter 3 surface expression by the amp-activated protein kinase mediates tolerance to glutamate excitation in neurons. *J Neurosci*, 29(9):2997–3008, 2009.

[221] Quan Wen and Dmitri B Chklovskii. A cost–benefit analysis of neuronal morphology. *Journal of neurophysiology*, 99(5):2320–2328, 2008.

[222] Benedikt Westermann. Mitochondrial fusion and fission in cell life and death. *Nature reviews Molecular cell biology*, 11(12):872–884, 2010.

[223] Alex H Williams, Cian O'donnell, Terrence J Sejnowski, and Timothy O'leary. Dendritic trafficking faces physiologically critical speed-precision tradeoffs. *Elife*, 5:e20556, 2016.

[224] John E Wilson. Isozymes of mammalian hexokinase: structure, subcellular localization and metabolic function. *J Exp Biol*, 206(12):2049–2057, 2003.

[225] Luise Wolf, Olin K Silander, and Erik van Nimwegen. Expression noise facilitates the evolution of gene regulation. *Elife*, 4:e05856, 2015.

[226] Man Yan Wong, Chaoming Zhou, Dinara Shakiryanova, Thomas E Lloyd, David L Deitcher, and Edwin S Levitan. Neuropeptide delivery to synapses by long-range vesicle circulation and sporadic capture. *Cell*, 148(5):1029–1038, 2012.

[227] Juliana C Wortman, Uttam M Shrestha, Devin M Barry, Michael L Garcia, Steven P Gross, and C Yu Clare. Axonal transport: how high microtubule density can compensate for boundary effects in small-caliber axons. *Biophysical journal*, 106(4):813–823, 2014.

[228] Chong-Chong Xu, Kyle R Denton, Zhi-Bo Wang, Xiaoqing Zhang, and Xue-Jun Li. Abnormal mitochondrial transport and morphology as early pathological changes in human models of spinal muscular atrophy. *Disease models & mechanisms*, 9(1):39–49, 2016.

[229] Edward Yang, Erik van Nimwegen, Mihaela Zavolan, Nikolaus Rajewsky, Mark Schroeder, Marcelo Magnasco, and James E Darnell. Decay rates of human mrnas: correlation with functional characteristics and sequence attributes. *Genome research*, 13(8):1863–1872, 2003.

[230] Zhaokang Yang and Derek S Steele. Effects of cytosolic atp on spontaneous and triggered ca2+-induced ca2+ release in permeabilised rat ventricular myocytes. *The Journal of Physiology*, 523(1):29–44, 2000.

[231] Richard J Youle and Derek P Narendra. Mechanisms of mitophagy. *Nature reviews Molecular cell biology*, 12(1):9–14, 2011.

[232] R.J. Youle and A.M. Bliek. Mitochondrial fission, fusion, and stress. *Science*, 337:1062–1065, 2012.

[233] Annalisa Zecchin, Peter C Stapor, Jermaine Goveia, and Peter Carmeliet. Metabolic pathway compartmentalization: an underappreciated opportunity? *Curr Opin Biotech*, 34:73–81, 2015.

[234] Chuan Li Zhang, Po Lai Ho, Douglas B Kintner, Dandan Sun, and Shing Yan Chiu. Activity-dependent regulation of mitochondrial motility by calcium and na/k-atpase at nodes of ranvier of myelinated nerves. *J Neurosci*, 30(10):3555–3566, 2010.

[235] Junjun Zhao, Albert Hiu Ka Fok, Ruolin Fan, Pui-Yi Kwan, Hei-Lok Chan, Louisa Hoi-Ying Lo, Ying-Shing Chan, Wing-Ho Yung, Jiandong Huang, Cora Sau Wan Lai, and Kwok-On Lai. Specific depletion of the motor protein kif5b leads to deficits in dendritic transport, synaptic plasticity and memory. *Elife*, 9:e53456, 2020.

[236] Yuanzi Zhao, Camille Fung, Don Shin, Bo-Chul Shin, Shanthie Thamotharan, Raman Sankar, Dan Ehninger, Alcino Silva, and Sherin U Devaskar. Neuronal glucose transporter isoform 3 deficient mice demonstrate features of autism spectrum disorders. *Mol Psychiatr*, 15(3):286, 2010.

[237] Yan-Rong Zheng, Xiang-Nan Zhang, and Zhong Chen. Mitochondrial transport serves as a mitochondrial quality control strategy in axons: Implications for central nervous system disorders. *CNS Neuroscience & Therapeutics*, 25(7):876–886, 2019.

[238] Bing Zhou, Panpan Yu, Mei-Yao Lin, Tao Sun, Yanmin Chen, and Zu-Hang Sheng. Facilitation of axon regeneration by enhancing mitochondrial transport and rescuing energy deficits. *J Cell Biol*, 214(1):103–119, 2016.

[239] Xiao-Hong Zhu, Hongyan Qiao, Fei Du, Qiang Xiong, Xiao Liu, Xiaoliang Zhang, Kamil Ugurbil, and Wei Chen. Quantitative imaging of energy expenditure in human brain. *Neuroimage*, 60(4):2107–2117, 2012.

[240] Luyun Zou, Xiaoyuan Zhu-Mauldin, Richard B Marchase, Andrew J Paterson, Jian Liu, Qinglin Yang, and John C Chatham. Glucose deprivation induced increase in protein o-glcnacylation in cardiomyocytes is calcium dependent. *Journal of Biological Chemistry*, pages jbc–M112, 2012.